



# 60GHz front-end receiver chain in 90nm CMOS technology

**Khaled Khalaf**

Thesis submitted to the Faculty of Electrical Engineering,  
Mathematics and Computer Science, Delft University of  
Technology in partial fulfillment of the requirements for  
the degree of Master of Science.

**August 31, 2010**

*Advisors:*

*Prof. John Long, TU Delft*

*Prof. Piet Wambacq, IMEC*

©2010 Khaled Khalaf

Faculteit Elektrotechniek, Wiskunde en Informatica, Technische Universiteit Delft.  
Mekelweg 4, 2628 CD, Delft. Postal address: Postbus 5031, 2600 GA, Delft. Email:  
bureau@ewi.tudelft.nl.



# 60GHz receiver front-end chain in 90nm CMOS technology

by

**Khaled Khalaf**

Delft University of Technology

Thesis submitted to the Faculty of Electrical Engineering, Mathematics and Computer Science, Delft University of Technology in partial fulfillment of the requirements for the degree of Master of Science.

August 31, 2010

Advisors:

Prof.dr. John Long, TU Delft

Prof.dr. Piet Wambacq, IMEC Belgium

Committee members:

Prof.dr. John Long

Prof.dr. Piet Wambacq

Dr.ing. Marco Spirito

Wanghua Wu, M.Sc.

Dr.ir. Jos Weber



# Abstract

Operation at millimeter-wave frequency, where up to 7GHz of unlicensed bandwidth is available in the 60GHz band, provides an opportunity to meet the higher data rate demands of wireless users. Advancements in silicon technology permit one to consider exploiting the 60GHz band for commercial applications (e.g., short range, wireless HDTV transmission) for the benefit of end users. This could enable, for example, wireless streaming of uncompressed high-quality video packets of a movie in few seconds due to data rates as high as multi gigabits per second. In this thesis, the design of a receiver front-end circuit for operation in the 60GHz range in 90nm CMOS is described. The thesis includes design details of the blocks used in the receiver, including: quadrature voltage-controlled oscillator (QVCO), local oscillator (LO) buffers, divider chain, low-noise amplifier (LNA) and mixer. The QVCO predicts 56.8-64.8GHz tuning range from schematic simulations. The divider chain has 15GHz locking range at rail-to-rail (0.5V-peak) input signal. The LNA and mixer combination achieves a maximum conversion gain of 26.77dB and a noise figure of 5.88dB. The output -1dB compression point is +6.3dBm and IIP3 is -8.6dBm. The complete front-end consumes 91.7mW from 1V supply. Physical layout of the test circuit and post-layout simulations for the implementation of a test chip including the QVCO and the first stage divider are also presented. Post-layout simulations show a maximum phase noise of -97.4dBc/Hz over 55.4-61.7GHz tuning range.

# Acknowledgements

This work was fulfilled as a result of a cooperative research project between the TU Delft Electronics and IMEC wireless research groups. So, I would like to thank all those who helped me bring this work to life. I'd like to thank my advisors, professors John Long and Piet Wambacq, for their valuable guidance and discussions, and for making such cooperation possible. Special thanks to my direct supervisor, Vojkan Vidojkovic, for his constant support and continuous technical and un-technical discussions during my period at IMEC. I'd like to thank Bertrand Parvais, Kuba Raczkowski, Kristof Vaesen, Charlotte Soens, Viki Szortyka, Giovanni Mangraviti, Karen Scheir and Julien Ryckaert for all their help, guidance and fruitful discussions at IMEC. I'd like also to thank Roeland Vandebriel for the IO ring implementation. Thanks extended to all who shared their thoughts and helped me in TU Delft including Yanyu Jin, Mina Danesh, Wanghua Wu, Hakan Cetinkaya, Senad Hiseni and Antoon Frehe. I'd like to acknowledge all my professors at TU Delft including Leo de Vreede and Klaas Bult for their encouraging and valuable course contents, and all my classmates and friends in Delft who made it easier for me staying that period just studying! I appreciate the efforts of all my friends in Leuven that were continuously supporting me in the good and bad times. I've to express deep thanks to my friends in Germany who actually encouraged me taking this study step from the beginning regardless all the difficulties that were facing me. Last but not least, I'd like to send deep regards for my bachelor staff members in Ain Shams University who guided me through such an interesting research and career path.

# Table of Contents

<b>List of Figures</b> .....	<b>viii</b>
<b>List of Tables</b> .....	<b>xiii</b>
<b>Glossary</b> .....	<b>xiv</b>
<b>Introduction</b> .....	<b>1</b>
1.1 Motivation .....	1
1.2 60GHz area background.....	2
1.2.1 Standards and frequency plan .....	2
1.2.2 Beamforming and system architecture .....	3
1.2.3 Enabling technology .....	5
1.2.4 Applications .....	6
1.3 Thesis objectives .....	7
1.4 Organization of the following chapters .....	8
<b>Background</b> .....	<b>9</b>
2.1 QVCO .....	9
2.1.1 VCO basics .....	9
2.1.2 Main parameters .....	11
2.1.3 Phase noise origins.....	16
2.1.4 Quadrature VCO .....	19
2.2 LO buffer.....	22
2.3 Frequency divider.....	25
2.3.1 ILFD.....	26
2.3.2 Static divider .....	30
2.4 LNA.....	32
2.4.1 NF and IIP3.....	32
2.4.2 LNA topology .....	34
2.5 Mixer .....	36
2.5.1 Main parameters .....	36
2.5.2 Mixer topology .....	38
<b>Design and Simulation Results</b> .....	<b>41</b>
3.1 $f_T$ of the 90nm NMOS transistor .....	41
3.2 Passive elements.....	42
3.2.1 Varactors .....	42
3.2.2 Transmission lines .....	43
3.2.3 Inductors .....	44

3.2.4	Transformers .....	45
3.3	QVCO and LO buffer .....	48
3.3.1	Circuit schematic .....	48
3.3.2	Circuit operation .....	48
3.3.3	Design guidelines .....	52
3.3.4	Design values .....	58
3.3.5	Simulation results of P-QVCO .....	59
3.3.6	Simulation results of BS-QVCO .....	65
3.3.7	Performance summary .....	66
3.4	Divider chain .....	67
3.4.1	Circuit schematic .....	67
3.4.2	ILFD locking range .....	68
3.4.3	Design guidelines .....	70
3.4.4	Design values .....	72
3.4.5	Simulation results .....	73
3.4.6	Performance summary .....	78
3.5	LNA and mixer .....	79
3.5.1	Circuit schematic .....	79
3.5.2	Design guidelines .....	80
3.5.3	Design values .....	80
3.5.4	Simulation results .....	81
3.5.5	Performance summary .....	86
	<b>Top-Level Design .....</b>	<b>87</b>
4.1	Complete top-level circuit .....	87
4.1.1	Circuit schematic .....	87
4.1.2	Design choices .....	87
4.1.3	Design values .....	88
4.1.4	Simulation results .....	90
4.2	QVCO and divider sub-system .....	91
4.2.1	Circuit schematic .....	91
4.2.2	Design choices .....	92
4.2.3	Design values .....	94
4.2.4	Simulation results .....	94
	<b>Layout and Post-Layout Simulations.....</b>	<b>99</b>
5.1	Physical layout .....	99
5.2	Nominal simulation results .....	101
5.2.1	Divider .....	101

5.2.2	QVCO and LO buffer .....	102
5.3	PVT simulations.....	104
<b>Conclusions.....</b>		<b>106</b>
6.1	Summary .....	106
6.2	Future work .....	107
<b>Transformer-Coupled Buffer .....</b>		<b>109</b>
<b>Bibliography .....</b>		<b>111</b>

# List of Figures

---

Figure 1.1: Atmospheric propagation attenuation versus frequency [5].	2
Figure 1.2: 57-66GHz band divided into 4 channels [7].	3
Figure 1.3: Radiation pattern of a beamformer [12].	4
Figure 1.4: Beamforming system with antenna arrays and transceivers [8].	4
Figure 1.5: 60GHz receiver architecture.	5
Figure 1.6: 60GHz potential indoor applications [22].	7
Figure 2.1: Cross-coupled LC VCO.	10
Figure 2.2: Small-signal analysis of the active part.	10
Figure 2.3: Oscillator negative resistor model.	11
Figure 2.4: VCO main defining parameters.	12
Figure 2.5: conversion from square wave current to sinusoidal output voltage through filtering by the resonator.	13
Figure 2.6: Oscillator output differential amplitude based on the operation of the tail current transistor.	14
Figure 2.7: Sidebands can be seen as AM and/or PM signals [24].	14
Figure 2.8: Downconversion of unwanted frequency bands due to oscillator spectral impurity.	15
Figure 2.9: Phase noise spectrum in dBc/Hz.	16
Figure 2.10: Noise folding due to cross-coupled pair [24].	18
Figure 2.11: Tail noise mixing with the cross-coupled pair [24].	18
Figure 2.12: Orthogonal signal out of the QVCO.	19
Figure 2.13: Parallel QVCO (P-QVCO) topology.	20
Figure 2.14: P-QVCO with gate decoupling and external bias.	20
Figure 2.15: (a) Top and (b) bottom half-sections of series-QVCO (TS-QVCO and BS-QVCO) topologies.	21
Figure 2.16: Gate-modulated QVCO (GM-QVCO) architecture.	21
Figure 2.17: Source follower buffer.	22
Figure 2.18: Inductively-tuned CS differential amplifier as a buffer.	23
Figure 2.19: Model of the active buffer.	23

Figure 2.20: Active buffer with transformer load (a) voltage output (b) current output.	24
Figure 2.21: Harmonic injection (injection-locked) frequency divider model [42].	26
Figure 2.22: Conventional ILFD.	27
Figure 2.23: Direct ILFD (a) circuit schematic and (b) equivalent model [47].	28
Figure 2.24: Block diagram of the differential direct ILFD [49].	29
Figure 2.25: Voltage and current waveforms (a) at $\phi=\pi/2$ and (b) $\phi=\pi/4$ [49].	29
Figure 2.26: Dual-mixing direct ILFD circuit schematic.	30
Figure 2.27: Conventional CML latches in a master-slave configuration [53].	31
Figure 2.28: High frequency CML divider (by two) [53].	31
Figure 2.29: Two-tone excitation resulting tones (to the third-order) [55].	33
Figure 2.30: Definition of important linearity parameters.	34
Figure 2.31: (a) Inductively degenerated CS transistor and (b) small-signal model.	35
Figure 2.32: Single-ended cascode LNA using inductive degeneration.	36
Figure 2.33: Definition of (a) SSB vs. (b) DSB NF.	37
Figure 2.34: Active implementation of double-balanced mixer.	39
Figure 2.35: Passive implementation of double-balanced mixer [16].	40
Figure 3.1: (a) Transit frequency of the used 90nm transistor, and (b) Drain current density vs. gate voltage.	42
Figure 3.2: (a) Capacitance and (b) quality factor for a varactor with $W=1\mu\text{m}$ and $M=20$ .	43
Figure 3.3: Transmission line (a) cross-section and (b) RLCG model.	44
Figure 3.4: Single-ended TL characteristic impedance vs. frequency.	44
Figure 3.5: (a) Inductance and (b) quality factor of the 300pH differential inductor.	45
Figure 3.6: Differential inductor lumped component model.	45
Figure 3.7: Transformer implemented with 83pH primary (=secondary) inductance in 90nm process.	46
Figure 3.8: Testbench used for the prediction of transformer parameters.	46
Figure 3.9: (a) Inductance, (b) quality factor and (c) coupling coefficient of the 83pH transformer.	47
Figure 3.10: Transformer lumped component model.	47
Figure 3.11: Circuit schematic of the used P-QVCO.	49
Figure 3.12: Circuit schematic of the transformer-coupled LO buffer with output load.	50

Figure 3.13: QVCO (a) without (b) with external gate bias, and (c) higher swing possibility without taking the cross-coupled transistors out of saturation.....	50
Figure 3.14: Impedance points of the QVCO two oscillation modes [57]. .....	51
Figure 3.15: Current and voltage-limited regimes with the bias current as a variable [59].....	55
Figure 3.16: (a) Average capacitance value and (b) effective capacitance curve for a varactor in a VCO [60]. .....	56
Figure 3.17: Less tuning frequency with higher current due to different effective capacitance values at different amplitudes. ....	56
Figure 3.18: P-QVCO and LO buffer amplitudes vs. oscillation frequency. ....	60
Figure 3.19: Phase noise at 1MHz offset vs. oscillation frequency.....	61
Figure 3.20: (a) A at max. and min. oscillation freq. (b) Max. and min. oscillation frequency variations with QVCO bias current. ....	61
Figure 3.21: Phase noise variations at max. and min. oscillation frequencies with QVCO bias current.....	62
Figure 3.22: Amplitude and phase noise variations with external gate bias at maximum oscillation frequency.....	63
Figure 3.23: Amplitude and phase noise variations with supply voltage at maximum oscillation frequency.....	63
Figure 3.24: Amplitude and phase noise variations with external gate bias at 1.2V supply and maximum oscillation frequency. ....	64
Figure 3.25: P-QVCO and LO buffer amplitudes vs. oscillation frequency at a reduced load transistor width of 24um. ....	64
Figure 3.26: BS-QVCO and LO buffer amplitudes and phase noise over the whole tuning range. ....	65
Figure 3.27: BS-QVCO and LO buffer amplitudes vs. oscillation frequency at a reduced load transistor width of 24um. ....	66
Figure 3.28: Divider chain block diagram.....	68
Figure 3.29: Differential to single-ended stage with output buffers.....	68
Figure 3.30: Locking range behavior with inductor quality factor.....	69
Figure 3.31: Divider output spectrum with quality factor curves assuming equal output amplitude. ....	70
Figure 3.32: 60GHz divider input sensitivity curve. ....	74
Figure 3.33: 60GHz divider output power at 4dBm input signal. ....	74

Figure 3.34: 30GHz divider input sensitivity curve. ....	75
Figure 3.35: 30GHz divider output power at 4dBm input signal. ....	75
Figure 3.36: First static divider input sensitivity curve. ....	76
Figure 3.37: First static divider output power at 4dBm input signal. ....	76
Figure 3.38: Second static divider input sensitivity curve. ....	77
Figure 3.39: Second static divider output power at 4dBm input signal. ....	77
Figure 3.40: Divider chain signal levels at each block. ....	78
Figure 3.41: Circuit schematic of the LNA+mixer combination [62]. ....	79
Figure 3.42: Conversion gain vs. LO input power for $R_L=1k\Omega$ . ....	82
Figure 3.43: Conversion gain vs. mixer load resistance for different LO input power values. ....	82
Figure 3.44: Conversion gain vs. LO input power for $R_L=5k\Omega$ . ....	83
Figure 3.45: Conversion gain vs. RF input frequency for $R_L=1k\Omega$ and $P_{LO,dBm}=4dBm$ . ....	83
Figure 3.46: (a) Noise figure vs. IF output frequency, and (b) S11 vs. RF input frequency. ....	84
Figure 3.47: -1dB compression point and third order intercept point for $R_L=1k\Omega$ . ....	84
Figure 3.48: Conversion gain vs. LO input power at 21.8mW total power consumption. ....	85
Figure 3.49: Conversion gain vs. LO input power at 10.55mW total power consumption. ....	86
Figure 4.1: Front-end top-level circuit schematic. ....	89
Figure 4.2: P-QVCO transient output voltage in the complete top-level system. ....	90
Figure 4.3: FFT of the P-QVCO output at max. and min. tuning ranges. ....	91
Figure 4.4: Voltage levels at the mixer and divider inputs vs. Lbuf1 value. ....	91
Figure 4.5: QVCO and divider sub-system circuit schematic. ....	93
Figure 4.6: Real part of the source follower output impedance (a) without current source, and (b) with current source at $M_{sf}=16$ . ....	95
Figure 4.7: (a) Small- and (b) large-signal voltage gain of the source follower. ....	95
Figure 4.8: Input sensitivity curve of the sub-system divider. ....	96
Figure 4.9: Output power of the sub-system divider. ....	96
Figure 4.10: (a) Amplitudes and (b) phase noise of the sub-system QVCO and LO buffer vs. tuning range without neutralization capacitors. ....	97

Figure 4.11: (a) Amplitudes and (b) phase noise of the sub-system QVCO and LO buffer vs. tuning range with neutralization capacitors.....	98
Figure 5.1: Top-level circuit layout with IO rings.....	100
Figure 5.2: The circuit core including the QVCO, LO buffer, divider and output buffer. .....	100
Figure 5.3: The P-QVCO, and LO buffer active elements with the ground cells omitted. .....	101
Figure 5.4: Divider input sensitivity curve and output power for a 48um OD inductor. .....	102
Figure 5.5: Divider input sensitivity curve and output power for a 55um OD inductor. .....	102
Figure 5.6: Variation with QVCO bias current at Vgate of 1V.....	103
Figure 5.7: Variations with gate voltage at Ivco of 30mA. ....	103
Figure 5.8: Performance at Vgate of 1V and Ivco of 30mA over the tuning range. ....	104
Figure 5.9: Amplitude and phase noise variations of the QVCO and LO buffer with supply voltage at Vgate of 1V and Ivco of 30mA. ....	105
Figure 5.10: (a) Amplitudes, (b) phase noise and oscillation frequency schematic simulations vs. process corners at 27°C.....	105

# List of Tables

---

Table 1.1: Channels defined by the IEEE and ECMA standards. ....	3
Table 3.1: QVCO and LO buffer target specifications. ....	48
Table 3.2: Design values for the QVCO and LO buffer. ....	58
Table 3.3: QVCO and LO buffer target specs & achieved results. ....	66
Table 3.4: Design values for the divider chain circuit. ....	72
Table 3.5: Performance summary of each divider block. ....	78
Table 3.6: Design values for the LNA and mixer. ....	80
Table 3.7: Performance summary of the LNA and mixer combination. ....	86
Table 4.1: LO buffers design values for the complete top-level circuit. ....	89
Table 4.2: Design values of the sub-system blocks (without the QVCO). ....	94
Table 5.1: Inductor parameters for the LO buffer and divider in the test chip. ....	100
Table 5.2: Worst case PVT simulation results. ....	105

# Glossary

---

<b>EHF</b>	Extremely high frequency
<b>ITU</b>	International Telecommunication Union
<b>IEEE</b>	Institute of Electrical and Electronics Engineers
<b>FCC</b>	Federal Communication Commission
<b>SC</b>	Single carrier
<b>HSI</b>	High speed interface
<b>AV</b>	Audio-video
<b>LOS</b>	Line of sight
<b>QVCO</b>	Quadrature voltage-controlled oscillator
<b>LO</b>	Local oscillator
<b>LNA</b>	Low-noise amplifier
<b>VCO</b>	Voltage-controlled oscillator
<b>AM</b>	Amplitude modulated
<b>PM</b>	Phase modulated
<b>SNR</b>	Signal-to-noise ratio
<b>SSB</b>	Single-sideband
<b>DSB</b>	Double-sideband
<b>P-QVCO</b>	Parallel QVCO
<b>TS-QVCO</b>	Top-series QVCO
<b>BS-QVCO</b>	Bottom-series QVCO
<b>GM-QVCO</b>	Gate-modulated QVCO
<b>CS</b>	Common-source
<b>CML</b>	Current-mode logic
<b>ILO</b>	Injection-locked oscillator
<b>ILFD</b>	Injection-locked frequency divider

<b>BPF</b>	Band-pass filter
<b>PVT</b>	Process, voltage and temperature
<b>PDN</b>	Pull-down network
<b>NF</b>	Noise figure
<b>IP3</b>	Third-order intercept point
<b>IIP3</b>	Input-referred third-order intercept point
<b>IM3</b>	Third-order intermodulation
<b>P-1dB</b>	-1dB compression point
<b>IF</b>	Intermediate frequency
<b>CG</b>	Conversion gain
<b>MoM</b>	Metal-oxide-metal
<b>TL</b>	Transmission line
<b>OD</b>	Outside dimension
<b>PLL</b>	Phase-locked loop
<b>RP</b>	Reduced-power
<b>IO</b>	Input-output
<b>TT</b>	Typical-NMOS typical-PMOS
<b>FF</b>	Fast-NMOS fast-PMOS
<b>FS</b>	Fast-NMOS slow-PMOS
<b>SF</b>	Slow-NMOS slow-PMOS
<b>SS</b>	Slow-NMOS slow-PMOS

# Chapter 1

## Introduction

---

The unlicensed band centered at 60GHz lies in the extremely high frequency (EHF) band, which is the highest radio frequency band<sup>1</sup> according to the International Telecommunication Union (ITU) running the range between 30 and 300GHz [1]. This frequency range is equivalent to wavelengths between 10mm to 1mm in free space. That's why it's also called the millimeter-wave (mm-wave) band. The Institute of Electrical and Electronics Engineers (IEEE) has another frequency band nomenclature that assigns 60GHz to the V band. The V band includes frequencies ranging from 40 to 75GHz [2].

### 1.1 Motivation

The increasing demands of society for technology driven appliances is pushing the trend to shift operation to higher frequencies, and advancements in silicon technology is making this shift feasible. Data transmission is the current example of our choice. Almost no person can imagine carrying a laptop or any other portable device which is not connected to the internet, or even to a local network, from which you're transmitting and receiving information. These can be ranging from simple text information to streaming video data that requires large data rates of few gigabits per second. A movie, for example, can be steamed with more quality if uncompressed data is used. This needs larger amount of data, which can be transferred at the same speed, or even faster, using higher data rates. Higher data rates require more bandwidth, which is available at higher frequencies. Thus, operation at mm-wave frequencies is a good choice, as compared to lower frequency bands (e.g., WiFi MIMO at 2.4GHz or 5GHz), to meet the current higher data rate demands of applications.

An unlicensed band of 7GHz around 60GHz from 57 to 64GHz was assigned by the Federal Communication Commission (FCC) in the United States [3]. Frequency bands

---

<sup>1</sup> EHF is an International Telecommunication Union (ITU) radio band symbol. It is also equivalent to the ITU radio band number 11, which is the highest till the time of writing this thesis.

of 57-66GHz and 59-66GHz were also assigned in Europe and Japan, respectively [4]. This is now encouraging commercial applications in the 60GHz band. Natural spatial isolation caused by propagation loss due to oxygen absorption makes communication in this frequency band only viable over short ranges (till 10 meters). Figure 1.1 illustrates the oxygen absorption peak in the 60GHz region.

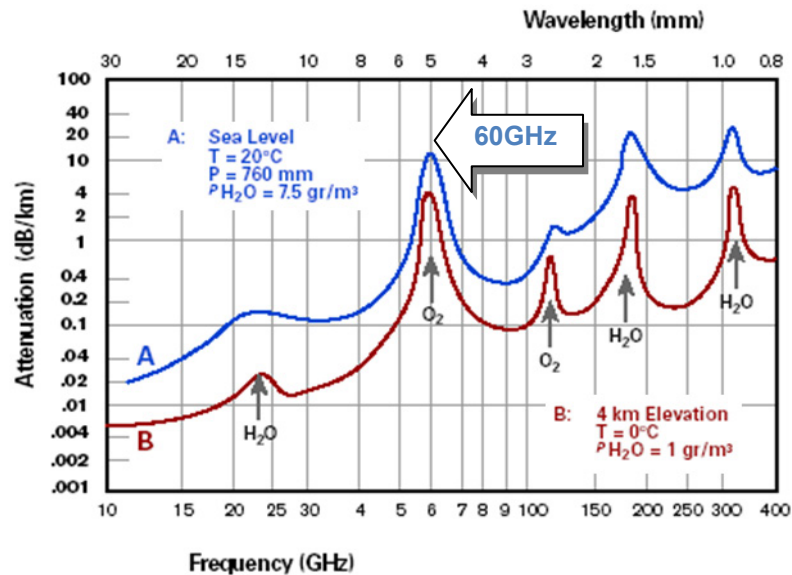


Figure 1.1: Atmospheric propagation attenuation versus frequency [5].

## 1.2 60GHz area background

More information about the 60GHz area from the system point of view is important to have a good background before starting circuit design. Circuit specifications were given as an input, and no system specs were derived from the standard. Thus, only some background information is going to be discussed in this section.

### 1.2.1 Standards and frequency plan

60GHz frequency planning is covered in detail in both IEEE 802.15.3c [6] and ECMA-387 [7] standards<sup>2</sup>. Three modes of operation are defined in the IEEE standard: single carrier (SC), high-speed interface (HSI) and audio-video (AV). The ECMA standard also defines three devices: Type A, Type B and Type C. These modes or devices differ in their capabilities and performance with a variety of modulation schemes, different data rates (reaching a maximum of around 25 Gbps) and different operating distances

<sup>2</sup> ECMA is more related to European standardization.

reaching 10m using line of sight (LOS) communication. The whole band (8.64GHz) is divided into four channels with 2.16GHz each, as depicted in Table 1.1 and graphically illustrated in Figure 1.2. Adjacent channels can be bonded together to allow more bandwidth. Several possibilities for bonding multiple, adjacent channels exist for increased data rate.

**Table 1.1: Channels defined by the IEEE and ECMA standards.**

Channel ID	Lower frequency GHz	Center frequency GHz	Upper frequency GHz
1	57.240	58.320	59.400
2	59.400	60.480	61.560
3	61.560	62.640	63.720
4	63.720	64.800	65.880

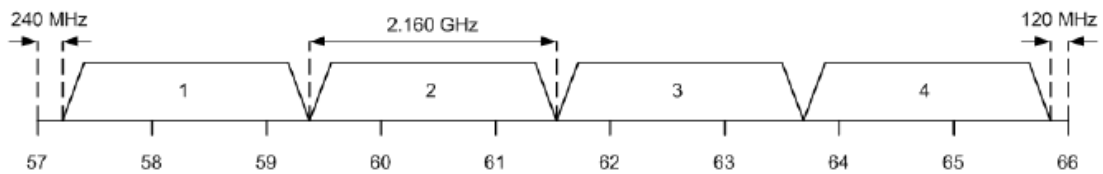


**Figure 1.2: 57-66GHz band divided into 4 channels [7].**

## 1.2.2 Beamforming and system architecture

Oxygen absorption at 60GHz causes signal attenuation due to propagation loss. One advantage of the implicit attenuation for operation at 60GHz is that signals cannot propagate more than 10 meters and cannot penetrate walls. This increases security between two close offices for example. Directional propagation is used to enhance signal transmission and reception. In the transmitter, radiated power is concentrated towards the receiver instead of being wasted in unwanted directions. Similarly, gain is boosted in one direction and unwanted interferers can be spatially attenuated in the receiver. This suggests using multiple antennas at the transmitter, to direct and enhance signal transmission, and at the receiver, to improve the sensitivity and reduce interference. The size of an antenna is inversely proportional to the operating frequency. For example, 60GHz operation allows the use of 16-element antenna array that occupies the same area as a dipole antenna at 5GHz [8].

Beamforming is a signal processing technique used in sensor arrays for directional signal transmission or reception [9]. The term Beamforming is derived from spatial

filters that were designed to form pencil beams (Figure 1.3) [10]. As shown in Figure 1.4, an array of antennas with variable gain and phase shifting (or time delay elements) can form different antenna patterns, one of which is a beam with a specific radiation angle  $\theta$  [8]. Time delays among different antenna paths need to be compensated by true time delay elements for coherent signal combination [11]. Assuming no channel bonding, signal bandwidth is around 2GHz, which is very small compared to the 60GHz carrier frequency. In narrowband systems, phase shift blocks can be used instead of true time delay elements as an approximation for the multi-path signal to add constructively [11].



Figure 1.3: Radiation pattern of a beamformer [12].

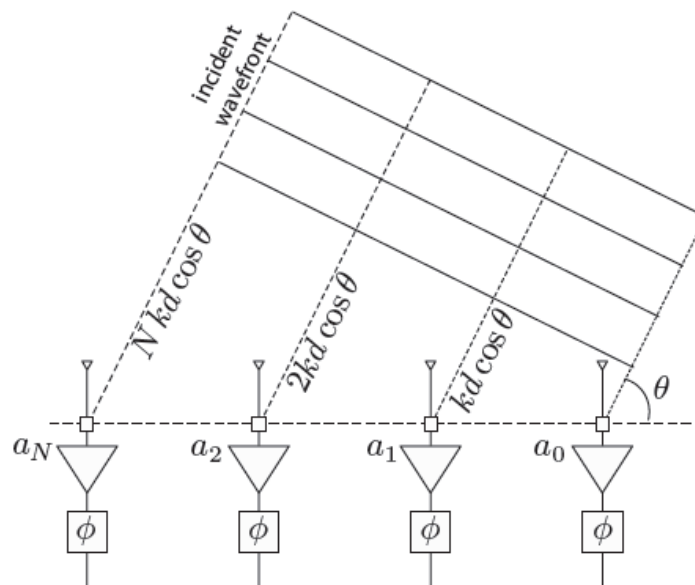


Figure 1.4: Beamforming system with antenna arrays and transceivers [8].

Phase shifting in a receiver can be implemented in four different ways: at RF after the LNA, at baseband after the mixer, in the LO path or using signal processing in the digital domain [13]. Signal combination in the digital domain uses the most hardware and is the most power hungry because the whole front-end is copied as many times as

the number of antenna paths. Phase shifting at RF (e.g., [14] and [15]) places lossy elements directly after the LNA which degrades the system gain, noise figure and bandwidth. System gain and noise figure are less sensitive to amplitude variations in the large LO signal. Thus, phase shifting at LO provides the lowest effect on signal quality. Phase shifting after the mixer causes insignificant deterioration of gain and noise figure (as compared to phase shifting at RF). Signal combination is performed at baseband in both LO and baseband phase shifting. In both cases, in order to avoid using multiple PLLs, LO signal should be distributed to different antenna paths. This includes other problems, such as cross-talk and low LO power levels.

One antenna path of the receiver is shown in the block diagram of Figure 1.5. Phase shifting and signal-combination are performed at baseband. The receiver is a direct conversion receiver, which includes a QVCO, LNA and mixer in the front-end. Antenna and baseband circuit design details are outside the scope of this thesis.

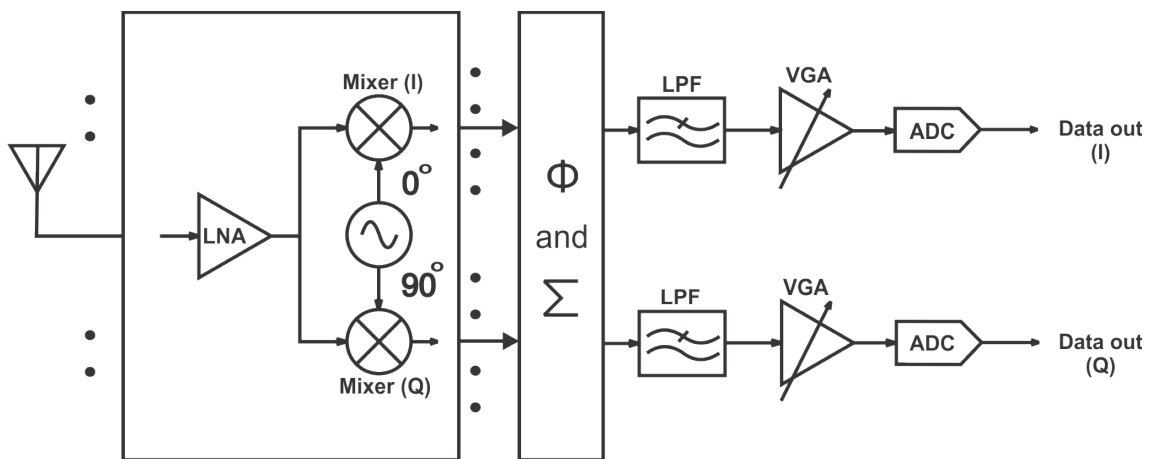


Figure 1.5: 60GHz receiver architecture.

### 1.2.3 Enabling technology

In a mixed-signal chip that includes analog and digital circuits, CMOS technology is preferred over bipolar for high volume applications when the digital part dominates. Moore's law states that on-chip density of transistors doubles every two years. This doubling is due to the fabrication of transistors with smaller minimum length. Smaller size transistors enable operation at higher frequencies. That's the reason for which operation at mm-wave became possible nowadays after it was just a dream years ago.

Scaling also has drawbacks. Smaller transistors usually require lower supply voltage due to the lower gate oxide. For example, the breakdown voltage is 1.8V for 0.18 $\mu$ m devices and 1.2V for 0.13 $\mu$ m ones [16]. This reduces the available voltage headroom, and thus, decreases voltage swings. The reduced supply voltage also limits the number of stacked transistors between supply and ground terminals. Smaller size transistors have more mismatch. This is because transistor mismatch is inversely proportional to the square root of its area [17].

Although devices are smaller in size, allowing for higher frequency operation, interconnects are not scalable as a consequence. Taking 60GHz as an example, wavelength in free space is 5mm. Assuming that the effective dielectric constant of a microstrip line is 4, the on-chip wavelength at 60GHz becomes 2.5mm. This means that a track length of more than 250 $\mu$ m carrying a signal with frequency components of 60GHz will cause a considerable difference in signal characteristics. This suggests the use of electromagnetic wave simulators, such as Agilent ADS [18] or Ansoft HFSS [19], to model relatively long interconnects, or with the help of a parasitic extraction tools, such as Mentor Graphics Caliber [20] or Cadence Assura [21], for medium and short interconnects.

### 1.2.4 Applications

The large bandwidth allocated for the 60GHz frequency band could be used to transfer tens of gigabytes of data in few seconds. Short range indoor applications like broadband internet access and high speed point-to-point wireless communication could utilize this capability. Wireless replacement of the cable HDMI technology is another potential application that will change the dark picture of wireless video steaming in our minds. Figure 1.6 gathers the main applications, such as HDTV-DVD wireless connection, high speed mobile internet connection, wireless docking station and wireless digital video cameras. We can also go further for the high data rate connection applications, especially the ability to replace any short range cable connection with very a high speed wireless link. That's all of course beside the implicit security and isolation causing no wall penetration for the 60GHz waves.

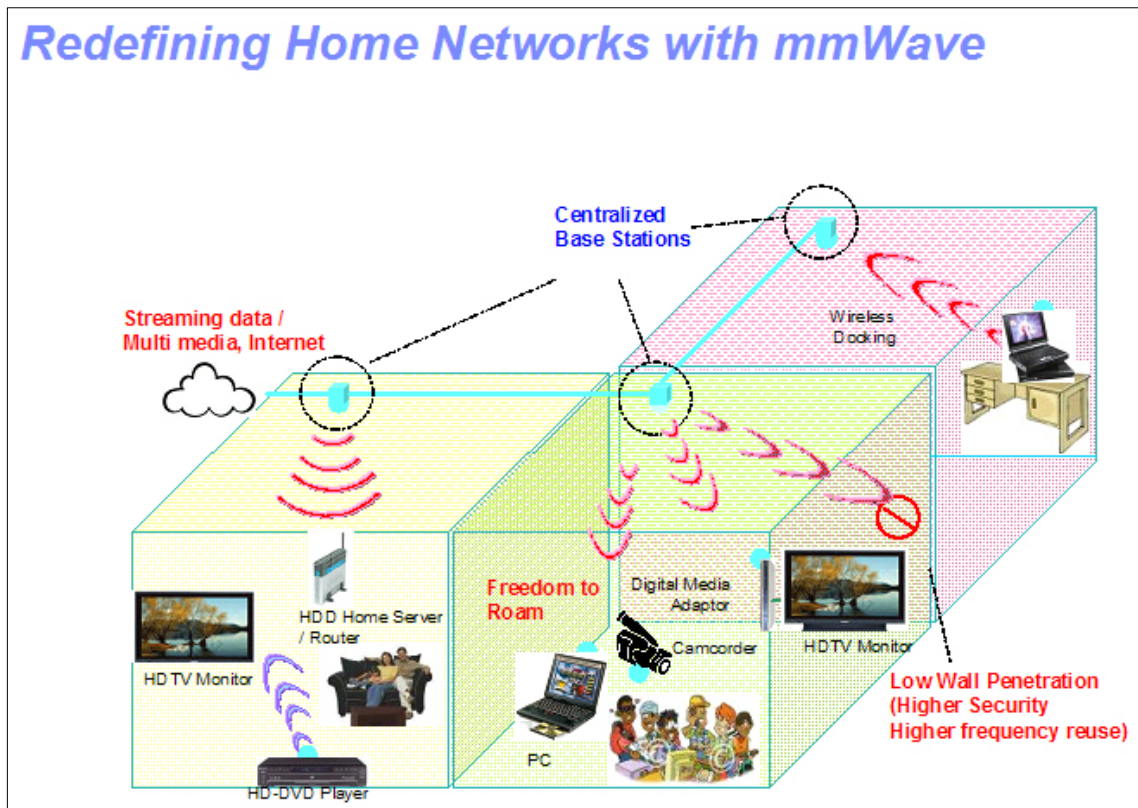


Figure 1.6: 60GHz potential indoor applications [22].

### 1.3 Thesis objectives

The main objective of this work is to build a receiver front-end that can be part of a complete 60GHz transceiver system. The front-end circuit includes a 60GHz QVCO that drives a divider chain and a LNA-mixer combination through LO buffers. The QVCO should provide a phase noise  $< -90\text{dBc/Hz}$  while oscillating at 60GHz with 8GHz tuning range. The divider chain is four consecutive divide-by-two blocks with locking range  $> 8\text{GHz}$  around 60GHz at the delivered input power level from the LO buffer. The LNA and mixer combination should be reused from a design in 45nm process. In the current 90nm process, it should still provide a conversion gain  $> 26\text{dB}$ , noise figure  $< 6\text{dB}$  and an output  $-1\text{dB}$  compression point  $> +3.5\text{dBm}$ . A subsystem including the QVCO with a LO buffer and the first stage of the divider chain are going to be laid-out and taped-out. Due to time limitations, measurement results of the test chip are not part of this work.

## **1.4 Organization of the following chapters**

The thesis consists of six chapters. Chapter 2 provides a theoretical background on the blocks used in the design in separate subsections. Some basic concepts and then a summary of topologies from a survey of the recent literature are shown. A detailed design procedure with schematics and simulation results for each circuit block are explained and elaborated in Chapter 3. It also provides some information on the technology used, such as transistor  $f_T$  and the design of passive inductors, transformers and transmission lines. Chapter 4 connects all the blocks together showing the predicted performance of both the entire front-end and the QVCO+divider sub-system at the top-level with simulation results. Chapter 5 shows the whole physical layout and some detailed block layouts. It also provides post-layout simulations and comparison with the pre-layout simulation results. Some simulations for process, supply and temperature variations are also included in the chapter. Finally, conclusions and recommendations for future research are listed in Chapter 6.

# Chapter 2

# Background

---

This chapter is going to present the theoretical background needed for the rest of the thesis. The blocks used in the design are going to be considered. This includes the quadrature voltage-controlled oscillator (QVCO), local oscillator (LO) buffer, injection-locked and static frequency dividers, low-noise amplifier (LNA) and the mixer.

## 2.1 QVCO

This section includes an introduction to the QVCO. The oscillation condition and main parameters defined in the cross-coupled LC oscillators are going to be reviewed. An overview on the origins of phase noise in differential LC oscillators is presented. Finally, the QVCO topologies discussed in recent literature are shown.

### 2.1.1 VCO basics

An oscillator is a circuit that generates a periodic signal in its steady state. The frequency of a voltage-controlled oscillator (VCO) is controlled by an external voltage source. It has no RF input signal, and it depends on the circuit noise to initiate a growing signal that settles to stable periodic signal in steady state. Oscillators may be used for frequency conversion in transceiver circuits and for clock generation in digital systems. An oscillator that generates a sine wave is a harmonic oscillator. A cross-coupled LC oscillator is widely used in communication systems. Compared to the resonator-less ring oscillator, it has superior phase noise performance but poorer quadrature accuracy when used to generate quadrature signals. As shown in Figure 2.1, the cross-coupled LC VCO is composed of two parts; an active cross-coupled pair and a tunable resonator including the passive elements.

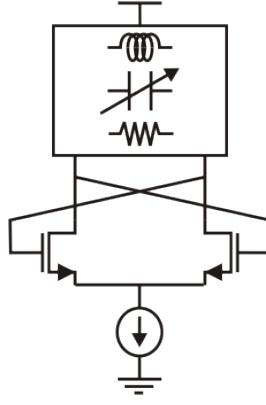


Figure 2.1: Cross-coupled LC VCO.

The transconductance and output resistance of the cross-coupled pair can be derived by connecting an AC voltage source at the output of the active part and deactivating independent sources, as in Figure 2.2.

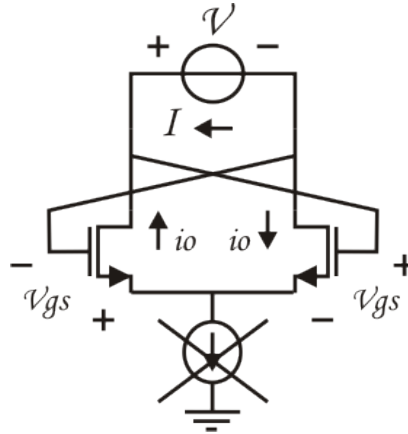


Figure 2.2: Small-signal analysis of the active part.

By relating  $V$  and  $I$  in Figure 2.2, we can determine  $g_m$  and  $R_{out}$  as following:

$$G_m = \frac{I_{out}}{V_{in}} = \frac{I}{V} = -\frac{i_0}{2V_{gs}} = -\frac{g_m}{2} \quad 2.1$$

$$G_m = \frac{I_{out}}{V_{in}} = \frac{I}{V} = -\frac{i_0}{2V_{gs}} = -\frac{g_m}{2} \quad 2.2$$

where  $G_m$  is the total active transconductance,  $g_m (= i_0/v_{gs})$  is the transistor transconductance and  $R_{out}$  is the total active output resistance.

The impedance seen at the drain terminals of the cross-coupled pair can now be seen as a negative resistance  $-R_m$  ( $R_m$  is assumed to be a positive number) with a noisy current source, as shown in Figure 2.3. The equivalent impedance of the tank circuit at resonance reduces to a resistor, because both positive (inductive) and negative (capacitive) reactances cancel each other.

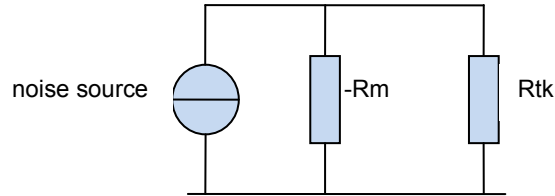


**Figure 2.3: Oscillator negative resistor model**

The circuit will start oscillation, with the help of the noise source, when the negative resistance (resembling a power generating element) is higher in magnitude than the positive resistance (which is a power dissipative element) that represents tank losses. This is the oscillation condition, which is equivalent to saying:

$$G_m > \frac{1}{R_{tk}} \quad 2.3$$

where  $R_{tk}$  is the tank resistance. This is a single port model for the oscillator. The factor by which the negative resistance is higher than the positive one ( $R_m/R_{tk}$ ) is the oscillation margin. This value should be greater than unity to ensure starting of oscillation.

### 2.1.2 Main parameters

The voltage-controlled oscillator is characterized by four main parameters: center frequency, tuning range, output voltage swing and phase noise. Figure 2.4 is a graphical illustration of these parameters.

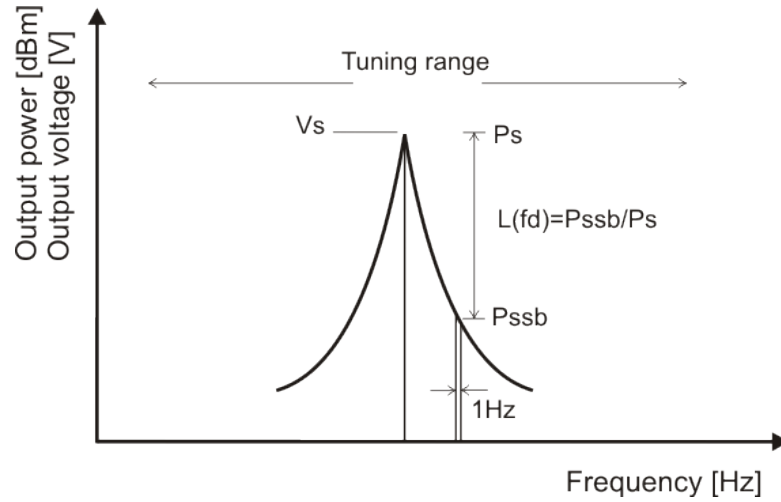


**Figure 2.4: VCO main defining parameters.**

The oscillator center frequency ( $f_0$ ) is the frequency at which the output power is largest. This is defined by the resonant frequency of the tank circuit, which leads to the following result:

$$f_0 = \frac{1}{2\pi\sqrt{LC}} \quad 2.4$$

where L and C are the total inductance and capacitance seen at the drain nodes of the cross-coupled pair.

The oscillator tuning range is the difference between the maximum and minimum output frequency of the oscillator ( $f_{max} - f_{min}$ ). This is usually controlled by a varactor, where the maximum and minimum capacitance of the varactor corresponds to the minimum and maximum output frequency of the oscillator, respectively.

$$f_{max} = \frac{1}{2\pi\sqrt{LC_{min}}} \quad 2.5$$

$$f_{min} = \frac{1}{2\pi\sqrt{LC_{max}}} \quad 2.6$$

$$f_0 = \frac{f_{max} + f_{min}}{2} \quad 2.7$$

The oscillator's output voltage swing is the amplitude at the oscillator center frequency. It should be high enough to drive the following stage. This is usually not the case, and

so a buffer is needed to deliver the required amplitude to the load. This will be shown in detail section 2.2. Voltage swing is usually limited by tank losses ( $R_{tk}$ ), and can be calculated, assuming a square wave output current, using the following equation:

$$V_{s-peak-diff} = A \approx \frac{2}{\pi} R_{tk} I_{tail} \quad 2.8$$

The main assumption to the previous equation is that the output current arises from ideal on-off switching of the transistors, and therefore the tail current is commutated between either sides of the oscillator. The current through  $R_{tk}$  is then as shown in Figure 2.5. The tank circuit is tuned to the fundamental tone of the square wave, which is then multiplied by the tank resistance to give a sinusoidal, differential output voltage swing.

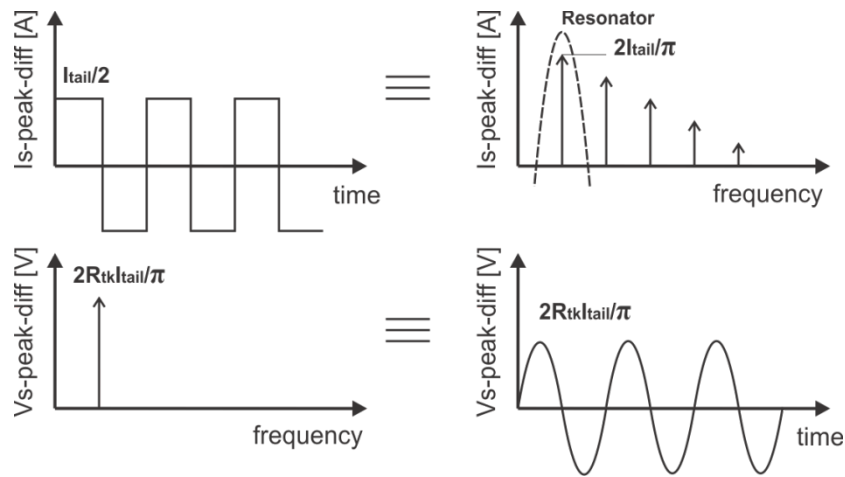


**Figure 2.5: conversion from square wave current to sinusoidal output voltage through filtering by the resonator.**

Equation 2.8 is only valid as long as the bias current is not large enough to push the tail transistor into the triode region. When the bias current is increased, the gate-source voltage of the tail transistor is increased while the drain-source voltage is limited by the voltage headroom available from the supply. At the edge of the triode region, the voltage swing is limited by the supply, and no longer proportional to the tail current. Thus, two regions of operation are defined: the current-limited regime and the supply-limited regime [23]. The oscillator output differential amplitude within the two regions is shown in Figure 2.6.

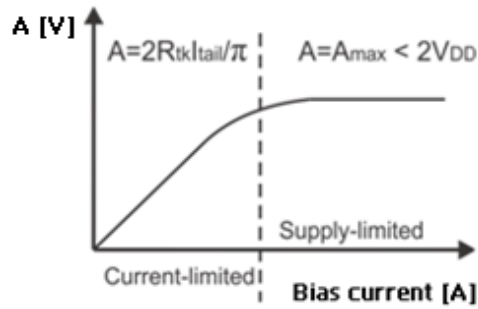


**Figure 2.6: Oscillator output differential amplitude based on the operation of the tail current transistor.**

The spectrum of the output voltage signal of a real VCO circuit is not just a single frequency representing a pure sine wave. As shown in Figure 2.4, the signal is spread in frequency having a skirt shape. In time domain, this can be seen as random variation of zero-crossings of the periodic sine wave signal representing the fundamental tone. In a phasor representation, this can be seen as a split into amplitude-modulated (AM) wave and phase-modulated (PM) wave as shown in Figure 2.7, where both can yield phase noise, either directly or indirectly.

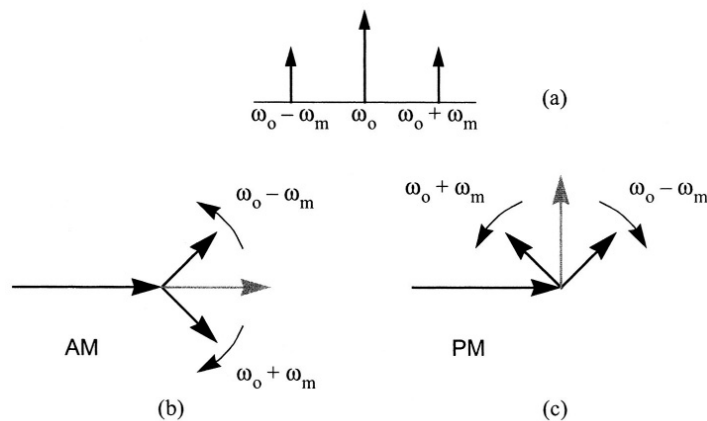


**Figure 2.7: Sidebands can be seen as AM and/or PM signals [24].**

Phase noise is the parameter defining the spectral purity of the oscillator. The oscillator output signal is more “pure” when the fundamental component of its frequency domain is less spread in frequency. This is translated to a lower phase noise value. This parameter is very crucial, especially in receiver circuits. As shown in Figure 2.8, an oscillator with a high phase noise can cause frequency down-conversion for unwanted

adjacent channels, which cannot be distinguished from the wanted signal. This leads to signal interference and higher noise, reducing the system's signal-to-noise ratio (SNR).

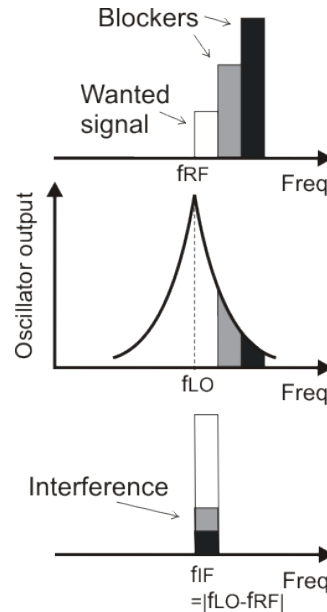


**Figure 2.8: Downconversion of unwanted frequency bands due to oscillator spectral impurity.**

As mentioned in [16] and [24], phase noise is characterized using the single-sideband (SSB) phase perturbation spectral power in a 1 Hz bandwidth (spectral power density) at a frequency offset  $f_d$  away from the carrier frequency normalized to the power of this fundamental carrier frequency. Figure 2.9 shows the phase noise curve in dBc/Hz versus frequency. Three regions are defined according to the phase noise slope. The first region is independent of frequency, which is the white noise in the system. The second region is proportional to  $f^2$ , and it shows the tank effect on the thermally induced noise sources in circuit components. Close-in phase noise is represented by the third region, which is proportional to  $f^3$  and is due to active elements' flicker noise up-conversion close to the carrier frequency.

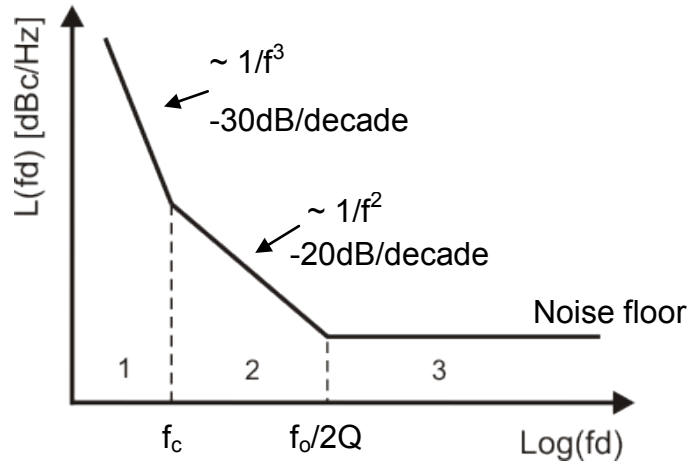


Figure 2.9: Phase noise spectrum in dBc/Hz.

Several models and analyses for phase noise are presented in the literature aiming at understanding the relationships between circuit parameters and phase noise, and getting an equation that can predict the phase noise value [25], [26], [27], [28], [29]. More intuitive interpretations and closed form formulas were also developed [30], [31]. This is in order to have the possibility of exploring ways to reduce this unwanted effect in oscillators. Phase noise in the  $1/f^2$  region, assuming a square wave output current and neglected parasitic capacitance, can be written in terms of circuit parameters as following [32].

$$\mathcal{L}(f_d) = 10 \log \left[ \frac{kT}{C^2 A^2 R_{tk} f_d^2} (1 + \gamma_n) \right] \quad 2.9$$

where  $C$  is the total VCO capacitance at the output nodes,  $A$  is the peak differential voltage swing,  $R_{tk}$  is the equivalent losses at the oscillator output and  $\gamma_n$  is the NMOS transistor excess channel noise parameter. This equation accounts for both tank and switch noise. Accurate prediction of the phase noise value is not expected using this equation at 60GHz due to large parasitics. However, it is useful in determining the effect of circuit parameters on phase noise in the  $1/f^2$  region.

### 2.1.3 Phase noise origins

Understanding phase noise origins can help choosing the correct modification in a circuit to reduce its value. A brief summary of phase noise origins will be presented in this section. In [24] the differential LC oscillator phase noise is studied in great detail.

The thermally induced phase noise can be a result of three main sources: the resonator, the differential pair and the current source.

### **2.1.3.1 Resonator noise**

Resistance  $R_{tk}$  representing tank losses is the noise generating element in the resonator. The noise current can be divided, due to the cross-coupled pair non-linearity, into AM and PM signals modulating the main oscillator tone. The AM signal can be filtered due to the limiting action of the cross-coupled pair. The cross-coupled pair negative resistance cancels the tank losses, and the PM signal is multiplied by the lossless resonator transfer function. This shows the importance of a lower bandwidth, i.e., higher quality factor resonator.

### **2.1.3.2 Differential pair noise**

Noise in the cross-coupled pair will only be effective when both transistors are in the active region (this is mostly the case at 60GHz). If one transistor switches off, the noise current of the other transistor will be in series with a constant current source  $I_{tail}$ , and thus eliminated. This can be modelled as the cross-coupled transistor white noise current multiplied by a pulsed  $G_m$  function with a frequency of  $2f_o$ . As shown in Figure 2.10, the current noise of the cross-coupled transistors only at the fundamental frequency and its odd harmonics will cause noise to be folded at the oscillation frequency when multiplied by the pulsed  $G_m$  function. This analysis shows the importance of the noise generated at odd harmonics of the oscillation frequency from the cross-coupled pair. Note that the width of the time window at which both transistors are active doesn't affect the output referred noise density. The higher transistor transconductance, the less MOS transistors are in saturation region, and thus, the higher  $G_m$  sinc function bandwidth. But input-referred noise noise density is also lowered with higher transconductance. This leads to the same integrated rms output noise [33].

### **2.1.3.3 Tail current noise**

Noise in the tail current will be commutated between the two sides of the oscillator. This can be modeled as being multiplied by a square wave with frequency components at the fundamental and odd harmonics.

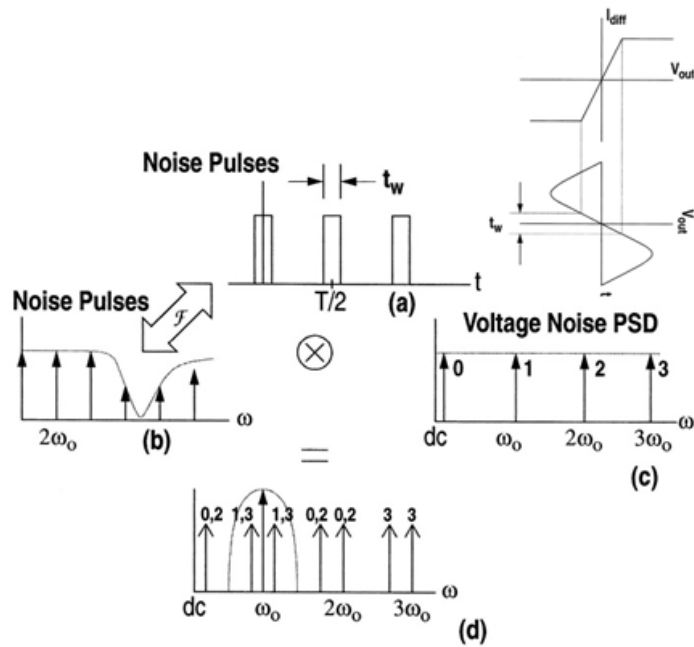


Figure 2.10: Noise folding due to cross-coupled pair [24].

Multiplications that will end up with noise components around the fundamental frequency are the square wave fundamental component with tail noise at DC and at second harmonic. Also the square wave third harmonic with the tail noise second harmonic, and so on. This is shown in Figure 2.11. Note that only tail noise components at DC and even harmonics are causing noise components at the fundamental frequency. Note also that tail noise component at DC will produce an AM signal. A varactor is a component that will convert voltage signal into a change in the capacitance value, and thus, a change in the operating frequency. Owing to the varactor in the VCO, the AM signal generated from the DC component of the tail noise can be converted into an FM signal which appears as phase noise around the center frequency [34], [35].

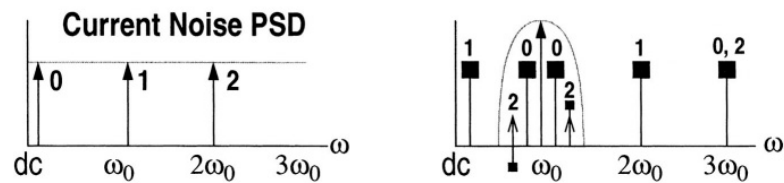


Figure 2.11: Tail noise mixing with the cross-coupled pair [24].

### 2.1.4 Quadrature VCO

In direct conversion receivers, positive and negative sidebands of the RF signal spectrum are down-converted on top of each other at baseband [36]. In frequency and phase modulated signals, two down-converting paths with a  $90^\circ$  phase shifted oscillator signal are needed for demodulation. Quadrature voltage-controlled oscillator (QVCO) uses coupling mechanisms between two VCO's in order to produce four-phase outputs, all orthogonal to each other (Figure 2.12).

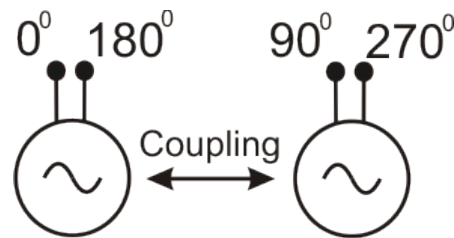


Figure 2.12: Orthogonal signal out of the QVCO.

One more parameter can be defined for the QVCO beside the main VCO parameters described before in section 2.1.2: phase error or quadrature error. For multi-phase oscillators, phase error is the difference in degrees between the actual phase difference between two subsequent output terminals in the oscillator and the ideal value. In the QVCO with in-phase (I) and quadrature (Q) outputs, quadrature error is the deviation from the  $90^\circ$  phase difference between I and Q terminals.

Cross-coupled LC VCO's can be coupled in three different ways, each with its pros and cons: parallel coupling (P-QVCO), series coupling (with two different choices; TS-QVCO and BS-QVCO for top and bottom, respectively) and gate-modulated coupling (GM-QVCO) [37]. All of the main VCO parameters are affected by inserting the coupling transistor in the VCO core.

In the P-QVCO shown in Figure 2.13, the coupling transistors are connected in parallel to the cross-coupled transistors. A, B, C and D outputs represent phase shifts of  $0^\circ$ ,  $180^\circ$ ,  $90^\circ$  and  $270^\circ$ , respectively. This topology is simple but has some disadvantages: phase noise is relatively high compared to the other topologies, and there is a trade-off between the phase noise and the quadrature accuracy through the coupling strength. The

greater the coupling coefficient, the higher the phase noise but the better phase error, and vice versa.

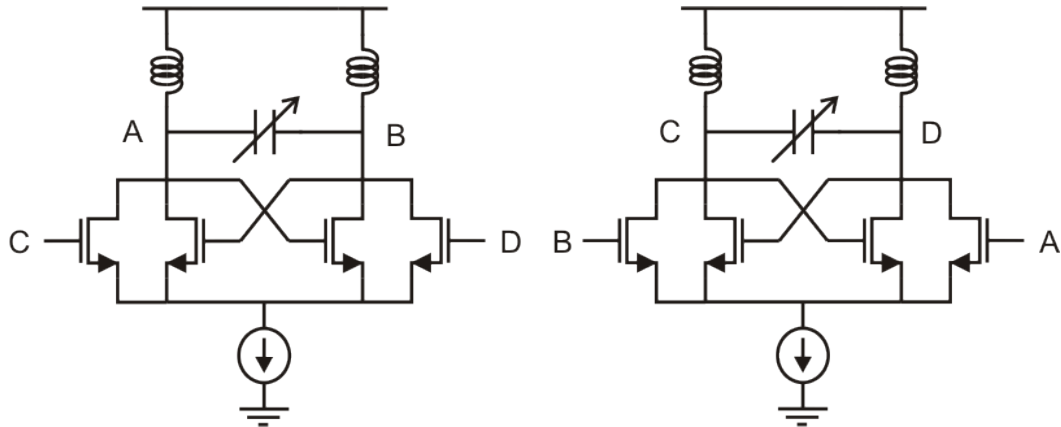


Figure 2.13: Parallel QVCO (P-QVCO) topology.

The P-QVCO phase noise can be improved by independently biasing the gate of the cross-coupled pair [38]. This requires gate decoupling capacitors and biasing resistors as shown in Figure 2.14. With a reduced gate voltage, the cross-coupled pair is allowed to provide more output voltage swings while operating in the saturation region.

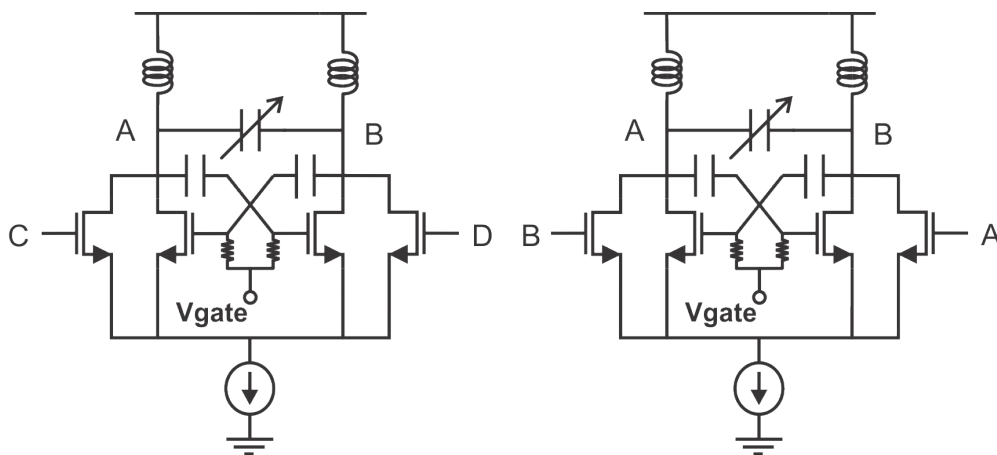
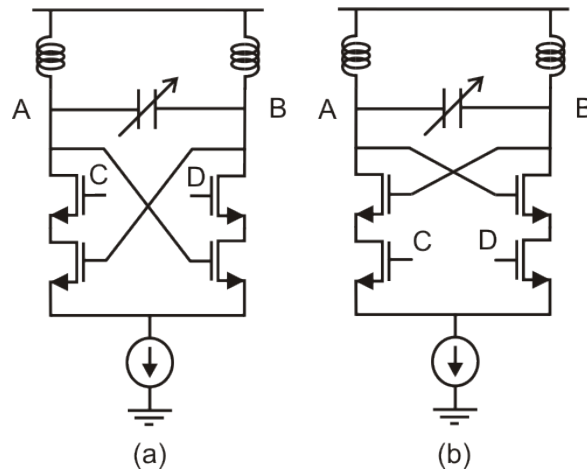


Figure 2.14: P-QVCO with gate decoupling and external bias.

In the top and bottom series-QVCOs of Figure 2.15, coupling transistors are inserted in series with the cross-coupled pair. This takes from the voltage headroom available which is not so suitable for low-voltage applications. In the TS-VCO, large coupling transistors are needed to have lower phase error, which will dramatically increase the

parasitic capacitance, and thus, reduce the tuning range. The BS-VCO, on the other hand, has higher phase accuracy and lower phase noise compared to the top-stacked one.



**Figure 2.15: (a) Top and (b) bottom half-sections of series-QVCO (TS-QVCO and BS-QVCO) topologies.**

As shown in Figure 2.16, a gate-modulated QVCO topology was proposed in [37]. The coupling transistors are placed in series with the gates of the switching transistors. This will improve the voltage headroom as compared to the series topologies. The GM-VCO was claimed to have the best quadrature accuracy and phase noise performances over the parallel and series ones. To ensure enough coupling strength from the opposite oscillator core, the coupling transistor sizes may need to be increased, which will lead to higher output parasitic capacitance, and thus, reduced tuning range.

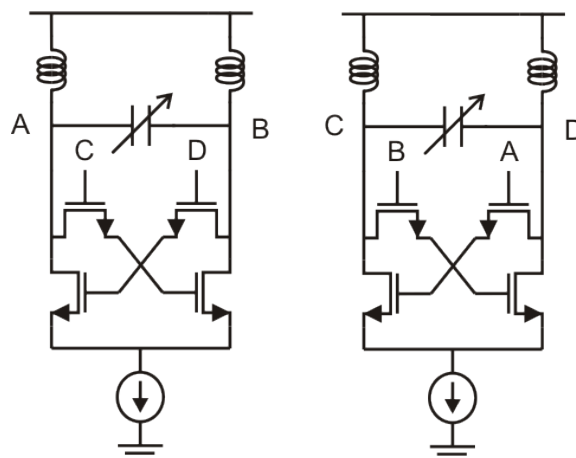


**Figure 2.16: Gate-modulated QVCO (GM-QVCO) architecture.**

## 2.2 LO buffer

A buffer is usually needed after the VCO to minimize any effect of the output load on the oscillator signal. The VCO output can either feed another block in the system or go directly to the output for measuring purposes. In both cases, the VCO load can be modeled as a parallel combination of a capacitance and a resistance. The load capacitance can reduce the oscillation frequency and tuning range. The load resistance, however, can reduce the output amplitude. Thus, the phase noise can also be increased. Buffers are also needed to increase the output amplitude. Local oscillator (LO) buffers, for example, can deliver the output signal to a mixer. For higher conversion gain, the mixer input amplitude should be increased. LO buffers can be useless if it has a higher load than the following stage or if the VCO amplitude is large enough for the operation of the following circuit.

Two transistor configurations can be used as buffers for the VCO: source followers and common-source (CS) amplifiers. Source-followers reduce the VCO output amplitude (Figure 2.17a). They can be used if the VCO output is going to be directly measured stand-alone. In this case, large output swing is not required as it is used for testing purposes. The common drain transistor has a low output resistance, which is suitable for driving the output  $50\Omega$  load.

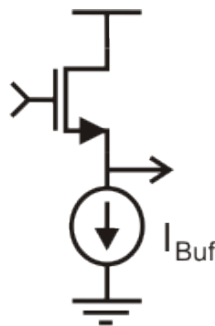


**Figure 2.17: Source follower buffer.**

Common-source amplifiers can also be used after the VCO for buffering, as shown in its differential form in Figure 2.18. Inductors can be used at high frequency to tune out all the parasitic and load capacitances at the output node. This allows the transistor to amplify the input signal within the required frequency range, with a peak at the tuning frequency  $f_{\text{tune}}$ , and a bandwidth limited by the current source  $I_{\text{buf}}$ .

$$f_{\text{tune}} = \frac{1}{2\pi\sqrt{L_{\text{buf}}C_{\text{tot}}}} \quad 2.10$$

where  $C_{\text{tot}} = C_{\text{parasitic}} + C_{\text{load}}$ . When the buffer is used for measuring, an accurate prediction of the pad capacitance is required for choosing the buffer inductor value. Any mismatch between the buffer tuning frequency and the oscillator frequency will cause a significant reduction in the output amplitude.

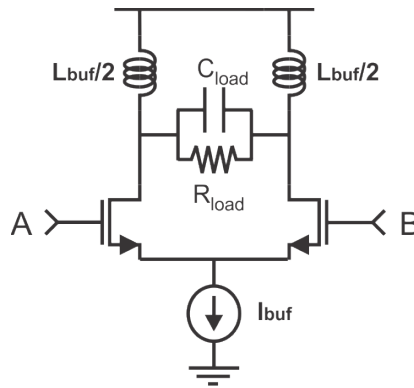


Figure 2.18: Inductively-tuned CS differential amplifier as a buffer.

The small-signal model of the buffer is shown in Figure 2.19. If the inductor cancels all capacitive elements at the output node, the buffer gain can be calculated as following:

$$A_{\text{buf}} = G_m(r_{\text{out}} \parallel R_{\text{load}} \parallel R_{\text{par,L}}) = \frac{g_m}{2} R_{\text{out}} \quad 2.11$$

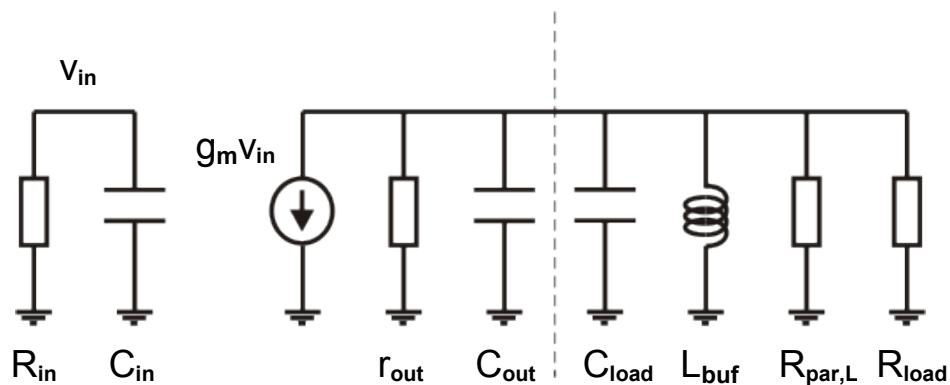


Figure 2.19: Model of the active buffer.

If the total capacitance at the output node is not large enough, large inductor values will be required. Maximum inductance is usually limited by the inductor self resonance frequency, after which the lines forming the inductor behave capacitively. One way to

get the gain peak at the required frequency is to add more capacitance at the output. Any additional capacitance comes with its parasitic resistance. This will add more load resistance to the output, and the total parallel resistance will be reduced, causing gain reduction.

$$A_{\text{buf}} = G_m(r_{\text{out}} || R_{\text{load}} || R_{\text{par,L}} || R_{\text{par,C}}) \quad 2.12$$

Another way to get the tuning frequency with a limited inductor is to exchange the inductor load with a transformer as in Figure 2.20a. The transformer used is nothing but an increased equivalent inductance with the factor (k), which is the coupling coefficient. So:

$$L_{\text{eq}} = L_{\text{tune}}(1 + k) \quad 2.13$$

It is worth noticing that a transformer is usually implemented with a lower quality factor than the inductor, as more than one metal layer should be used compared to the only top metal layer used in the inductor implementation. The gain can be the same as in Equation 2.11 with a different inductor quality factor.

$$A_{\text{buf}} = G_m(r_{\text{out}} || R_{\text{load}} || R_{\text{par,trafo}}) \quad 2.14$$

As shown in Figure 2.20b, the transformer can be used in such a way that the output current of the common-source transistor is used instead of the output voltage. One side of the transformer will be connected to the buffer circuit, and the other side will be connected to the load.

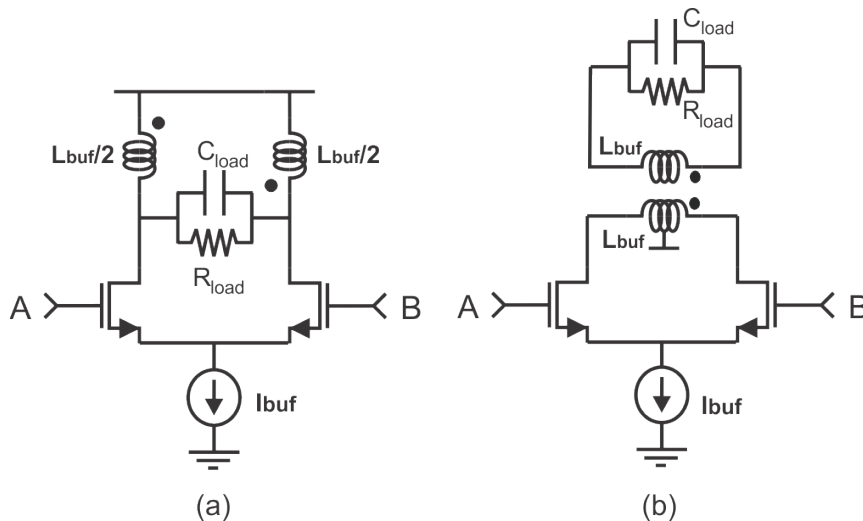


Figure 2.20: Active buffer with transformer load (a) voltage output (b) current output.

This transformer-coupled differential amplifier is analyzed in [39]. If the load is assumed to be only capacitive, it will be transformed to the buffer output node with an equivalent impedance value that is elaborated in appendix 0, and given below in its final form:

$$Z_{\text{out}} = j\omega \left( L + \frac{\omega^2 L^2 C_{\text{load}} k^2}{1 - \omega^2 L C_{\text{load}}} \right) \quad 2.15$$

This means that for practical values (for example,  $f = 60\text{GHz}$ ,  $L = 100\text{ pH}$  and  $C_{\text{load}} = 20\text{ fF}$ ), the denominator will always be positive, and the common-source transistors will see an equivalent inductance value that depends on the load. Note that the equivalent inductance is higher than the primary value of the transformer. In practice, the buffer load is a transistor with an equivalent input parallel capacitance and resistance. The resistive component is transformed to the buffer output with a higher value ( $R'_{\text{load}}$ ) [39]. Thus, the buffer voltage gain can be calculated as following:

$$A_{\text{buf}} = G_m (r_{\text{out}} || R'_{\text{load}} || R_{\text{par,trafo}}) \quad 2.16$$

Note that the voltage-output transformer-coupled buffer is expected to provide higher gain (Equation 2.14) compared to the current-output one (Equation 2.16) because of the higher load resistance.

## 2.3 Frequency divider

Frequency dividers are circuit blocks used to divide an input signal in the frequency domain. They can be categorized into static and dynamic dividers. Static dividers use bi-stable latches and, for operation at high frequencies, can be implemented using current-mode logic (CML) circuits [40]. Dynamic dividers don't quantize the divided signal in either amplitude or time. They are divided into regenerative, parametric and harmonic injection dividers [41]. The harmonic injection dividers are of interest because they can operate at smaller input signal amplitudes [41]. They depend on a free-running oscillator, and synchronizing the harmonics of the free-running frequency with an input source.

Static dividers have a trade-off between speed (and thus maximum input frequency) and power dissipation, and they can operate down to DC. Analog dividers, on the other

hand, can operate at higher input frequencies with lower power consumption using only few transistors, but usually with limited input bandwidth (locking range).

### 2.3.1 ILFD

Oscillators depend on the non-linear behavior of circuit components to reach their steady-state. This non-linearity will enable harmonic components to appear together with the fundamental oscillation frequency. An input source can be injected at any of these harmonic frequencies, and synchronization of the oscillator output (i.e., injection locking) can take place. Locking range will decrease with higher order of the oscillator harmonic components because they have lower amplitudes.

Harmonic injection dividers are one group of injection-locked oscillators (ILOs). ILOs are divided into three categories; first-harmonic, sub-harmonic and super-harmonic ILOs. This depends on the relationship between the input signal frequency and the free-running oscillator frequency. The input frequency is the same as the oscillator free-running frequency in the first-harmonic ILO, lower and higher in the sub-harmonic and super-harmonic ILOs, respectively. So, harmonic injection dividers are super-harmonic ILOs, and they're also called injection-locked frequency dividers (ILFDs).

ILFDs can be modeled as shown in Figure 2.21 [42]. The model includes a non-linear device that generates harmonic energy and a band-pass filter (BPF) to select one of these harmonics. The BPF output is then fed back to the non-linear device and oscillation keeps running independently. An input signal can then be injected in the oscillator signal path to be synchronized with the selected frequency component after the BPF.

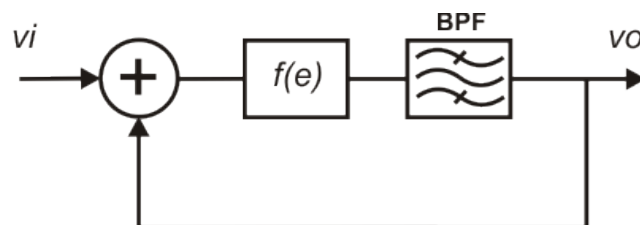


**Figure 2.21: Harmonic injection (injection-locked) frequency divider model [42].**

As the input signal frequency changes, the output should follow this change. The range of input frequencies across which the oscillator is still locking and the signal is divided

correctly is the locking range. A large locking range is important, as the frequency divider should cover the tuning range of the VCO plus a good margin. At high frequencies, larger margin is required to ensure proper operation within process, voltage and temperature (PVT) variations in the circuit.

ILFDs can be implemented using a cross-coupled LC oscillator generating the free-running signal. Traditional ILFDs [42] inject the input signal at the gate of the tail current transistor as shown in Figure 2.22. They suffer from large input capacitance, small locking range and they operate at low input frequencies. This is due to the large tail transistor size. A shunt peaking inductor and capacitor were inserted at the common-source node of the cross-coupled pair to tune out the tail transistor output capacitance [43]. This solution improved the maximum frequency and locking range, but with the use of large area passives and the need for careful adjustments of the inductor and capacitor values to get the required parasitic cancellation.

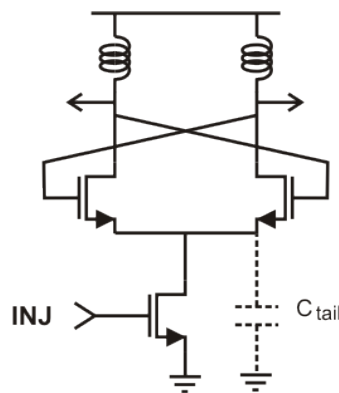


**Figure 2.22: Conventional ILFD.**

Another way to inject the input signal is through a transistor switch connected in parallel to the tank as shown in Figure 2.23a [44], [45], [46]. The direct ILFD doesn't incorporate extra passives and provides a simpler circuit. The injecting signal modulates the oscillator output and the signal with frequency difference is selected by the tank. A block diagram explaining the behavior of the circuit is shown in Figure 2.23b [47]. The output signal ( $f_i/2$ ) is fed back and mixed with the input signal ( $f_i$ ) generating the sum ( $3f_i/2$ ) and difference ( $f_i/2$ ) of both signal frequencies. The band-pass filter selects  $f_i/2$  and passes it to the output, thus providing division. The transistor switch in Figure 2.23a

works as a drain-pumped mixer [48], and the cross-coupled pair with the tuning inductor form the feedback loop.

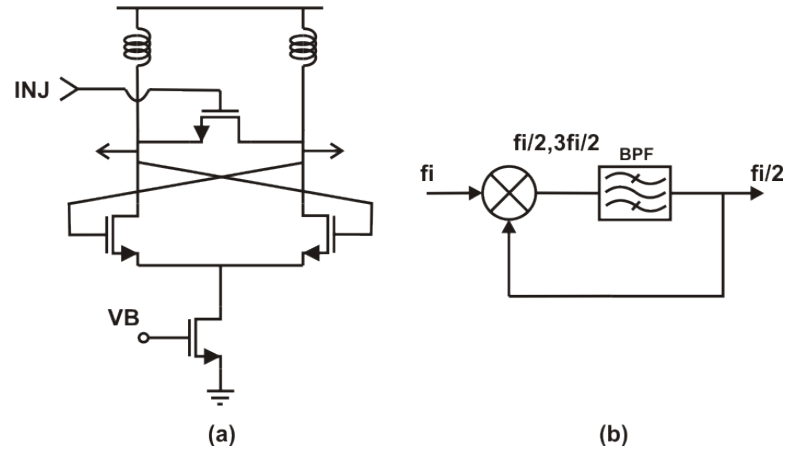


**Figure 2.23: Direct ILFD (a) circuit schematic and (b) equivalent model [47].**

An analytical model for the direct ILFD is developed in [49]. The model depends on substituting the switching transistor ( $M_{in}$ ) with passive elements. Figure 2.24 shows  $M_{in}$  and the relationship between the injected input voltage ( $V_{in}$ ), the differential output voltage  $V_{out\pm}$  and the channel current of  $M_{in}$  ( $I_{in}$ ). The difference in phase shift between the input and output voltage signals is  $\varphi$ . The voltage and current waveforms for  $\varphi=\pi/2$  and  $\varphi=\pi/4$  are shown in Figure 2.25. The locking range derived equation is as following:

$$\Delta\omega = 2g_{q,max}/C = 2\omega_0^2 Lg_{q,max} \quad 2.17$$

where  $L$  and  $C$  are the tank inductance and capacitance, respectively.  $g_{q,max}$  is the equivalent injecting transistor output conductance ( $g_{q,max} = I_q(\varphi)/2v_o$ ), which appeared as a result of modeling the injecting transistor as an inductor or a capacitor in parallel with a resistor.  $I_q(\varphi)$  is the magnitude of the quadrature component of  $I_{in}$ , and  $v_o$  is the magnitude of the output voltage.

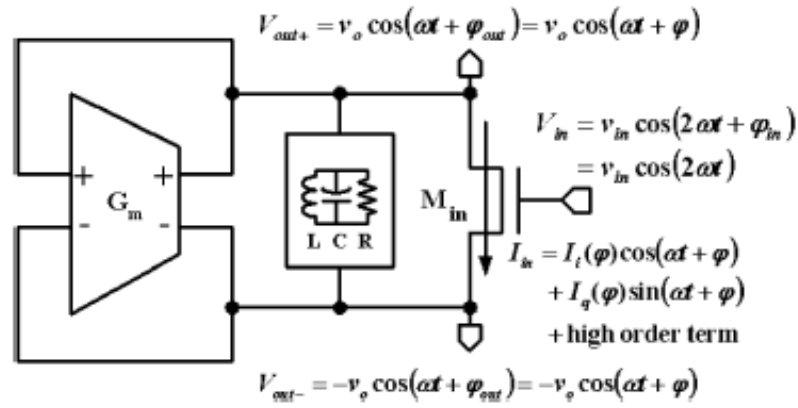


Figure 2.24: Block diagram of the differential direct ILFD [49].

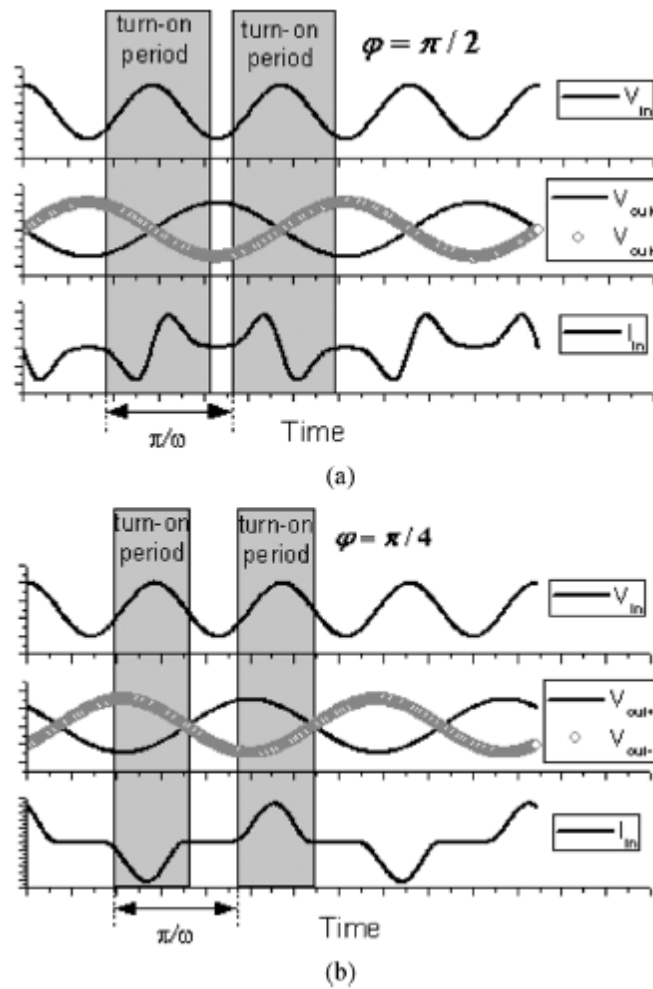


Figure 2.25: Voltage and current waveforms (a) at  $\varphi=\pi/2$  and (b)  $\varphi=\pi/4$  [49].



coupled pair keeps the output state unchanged. The second stage works in the same way with inverted clock signals to implement the DFF.

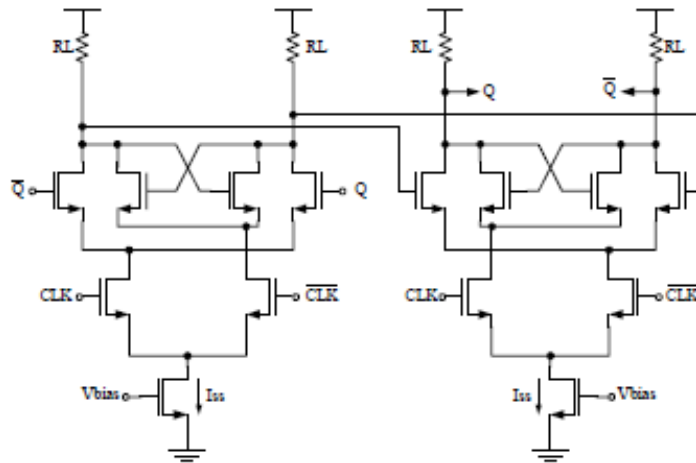


Figure 2.27: Conventional CML latches in a master-slave configuration [53].

The maximum operating frequency of the divider is limited by the CLK-Q time delay, which is a function of the total output capacitance and the load resistance, as well as the bias current. In [53], the cross-coupled pair size is reduced (to reduce the output capacitance) and the circuit is rearranged to have one tail transistor as shown in Figure 2.28.

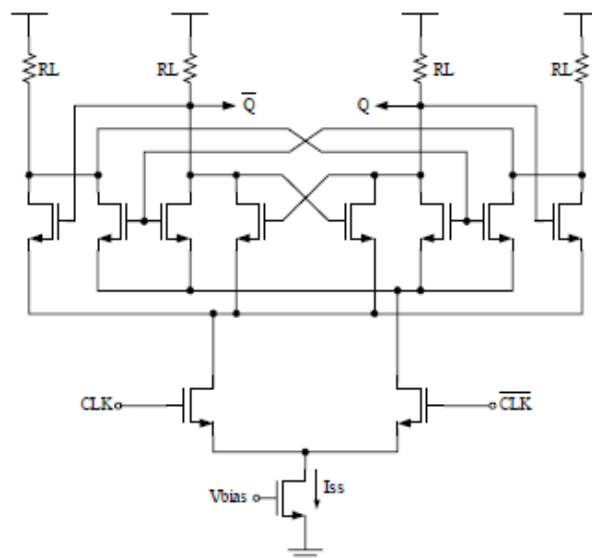


Figure 2.28: High frequency CML divider (by two) [53].

## 2.4 LNA

The low-noise amplifier (LNA) is usually used as the first block in the receiver front-end. It should add the lowest possible noise to the input signal. Noise degradation is usually measured with noise figure (NF). NF is a parameter that shows how much noise a block is adding to the system. Noise factor (F) is the linear equivalent of NF. LNAs should provide enough gain to overcome the noise figure of the following stages. This is suggested by Frii's formula, which calculates the system noise factor as following:

$$F_{\text{total}} = F_1 + \frac{F_2 - 1}{G_1} + \frac{F_3 - 1}{G_1 G_2} + \frac{F_4 - 1}{G_1 G_2 G_3} + \dots \quad 2.18$$

where G is the power gain of a block, and the subscript indicates the order of the block in the receiver. Assuming the LNA to be the first block in the system, Equation 2.18 shows how the LNA (with noise factor  $F_1$ ) is dominating the total noise, especially with a high gain ( $G_1$ ) value.

The LNA input should be matched to  $50\Omega$  to provide the lowest possible reflections from the source. It shouldn't also distort the input signal. Signal distortion is caused by the non-linear behavior of a block. Non-linearity is usually specified by the third order input-referred intercept point (IIP3). The total IIP3 of a system can be calculated as following:

$$\frac{1}{IIP3_{\text{total}}} = \frac{1}{IIP3_1} + \frac{G_1}{IIP3_2} + \frac{G_1 G_2}{IIP3_3} + \frac{G_1 G_2 G_3}{IIP3_4} + \dots \quad 2.19$$

Equation 2.19 shows that non-linearity of the latter stages are more effective due to the gain of the previous stages. So, the LNA distortion is not dominating the system non-linearity.

### 2.4.1 NF and IIP3

Noise figure of a linear two-port network as a function of the source admittance can be represented by:

$$F = F_{\text{min}} + \frac{R_n}{G_s} |Y_s - Y_{\text{opt}}|^2 \quad 2.20$$

where  $F_{\text{min}}$  is the minimum achievable noise factor,  $Y_s (= G_s + jB_s)$  is the source admittance,  $Y_{\text{opt}}$  is the optimum load at which F reduces to  $F_{\text{min}}$  (noise match

condition) and  $R_n$  is the noise resistance defining the sensitivity of  $F$  to changes in the source admittance.

Note that these parameters can be related to circuit parameters, such as  $f_T$ ,  $g_m$  and  $C_{gs}$  for a MOS transistor [54]. For minimum noise figure,  $F_{min}$  should be minimized by choosing the correct bias point, and the LNA input should be matched to the optimum source impedance that gives the minimum noise factor ( $Z_{opt}$ ). The source impedance for noise match is usually not  $50\Omega$  leading to the either a compromise between impedance and noise matching conditions or using a topology that allow for choosing the two impedances independently.

Non-linearity will cause additional tones to be generated at harmonic frequencies. If a signal with two frequency components at  $f_1$  and  $f_2$  enters the amplifier, more frequency components appear in the frequency band. Figure 2.29 shows the output spectrum with additional frequency components due to non-linearity (only to the third order).

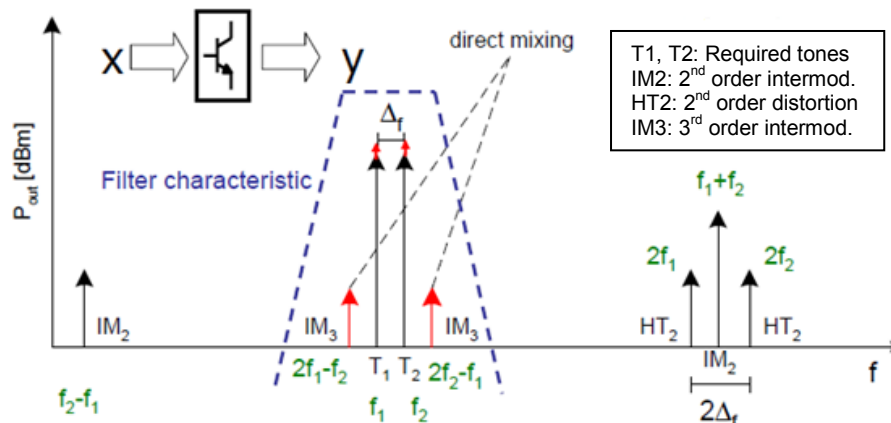


Figure 2.29: Two-tone excitation resulting tones (to the third-order) [55].

Harmonic frequencies ( $2f_1$ ,  $2f_2$ ,  $3f_1$ ,  $3f_2$ , ...) and second-order intermodulation components ( $f_1 - f_2$  and  $f_1 + f_2$ ) are of less importance as they can be easily filtered out. In a direct conversion receiver, ( $f_1 - f_2$ ) falls in-band but is usually not effective when using differential circuits. The third-order intermodulation products (IM3) are used in the definition of system non-linearity.

As shown in Figure 2.30, the fundamental output tone eventually goes into compression with increasing input power. Linear extrapolation of the fundamental and IM3 curves

will intersect at the third-order intercept point (IP3). Referred to its input, the IIP3 is used to define non-linearity in a system. The point at which the fundamental tone is compressed with 1dB is the -1dB compression point (P-1dB), which is also used to define the non-linearity of a system. The P-1dB as it's easier to measure because it uses a single input tone, compared to the two-tone test for the IIP3 measurement. Input -1dB compression point (P-1dB,in) is around 10dB lower than IIP3 [36], which gives an approximate value for the IIP3 when measured. Note that when dealing with a mixer, Figure 2.30 is used with the x-axis (input power) at RF frequencies, while the y-axis (output power) is at the intermediate frequencies (IF) resulting after the frequency conversion.

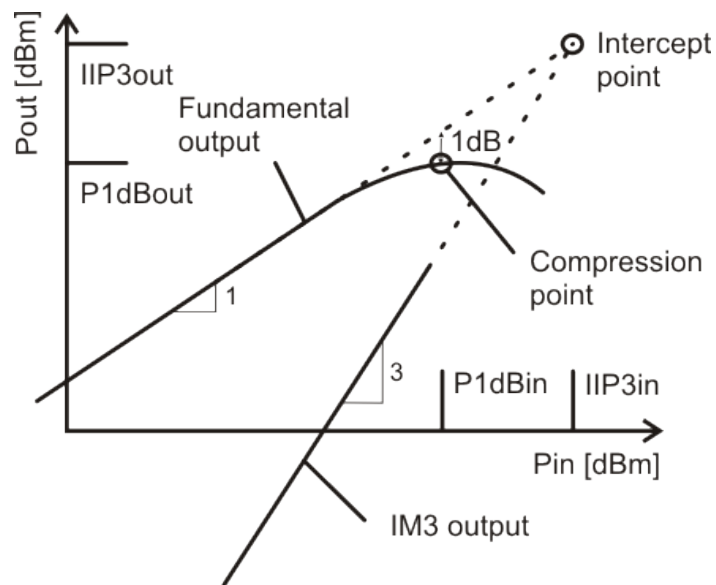


Figure 2.30: Definition of important linearity parameters.

## 2.4.2 LNA topology

The commonly used topology for the LNA is based on a common-source transistor with inductive degeneration, as shown in Figure 2.31a. If the small signal model of the transistor only contains an input capacitance  $C_{gs}$  and an output transconductance (Figure 2.31b), the degenerated inductor can be transformed to the input using the  $\beta$ -transformation concept, leading to the following input impedance:

$$Z_{in} = \frac{1}{j\omega C_{gs}} + j\omega L_{ss}[1 + \beta(\omega)]$$

$$\begin{aligned}
&= \frac{1}{j\omega C_{gs}} + j\omega L_{ss} + j\omega L_{ss} \frac{\omega_T}{j\omega} \\
&= L_{ss} \frac{g_m}{C_{gs}} + j \left( \omega L_{ss} - \frac{1}{\omega C_{gs}} \right)
\end{aligned} \tag{2.21}$$

where  $\beta(\omega)$  is the current gain.

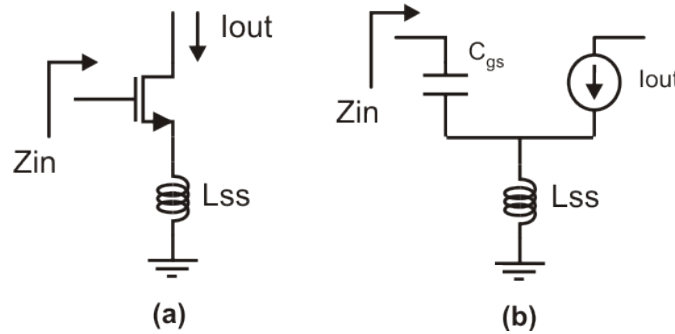


**Figure 2.31: (a) Inductively degenerated CS transistor and (b) small-signal model.**

The input impedance contains a resistive part, which can be made equal to  $50\Omega$ , and a reactive part. As the inductor  $L_{ss}$  is chosen to vary the resistive part, the reactive part will usually have a non-zero value. As the input capacitance  $C_{gs}$  is a very small value, the reactive part is usually capacitive. An inductor inserted at the gate can be used to cancel the imaginary part of the input impedance, leaving only  $50\Omega$  to match the source impedance of the LNA.

In our small-signal analysis to get the LNA input impedance, we neglected a lot of components. When added to the small-signal model, the transistor output resistance, through the overlap capacitance, can cause a significant drop in the real part of the input impedance [54]. This is due to the path created to the load of the LNA. A cascode transistor (maybe with a larger gate length leading to a higher output resistance) can be used to isolate the output load from the input circuit. This can keep good input matching properties for the LNA with the drawback of additional noise figure. The complete LNA can now be as shown in Figure 2.32.

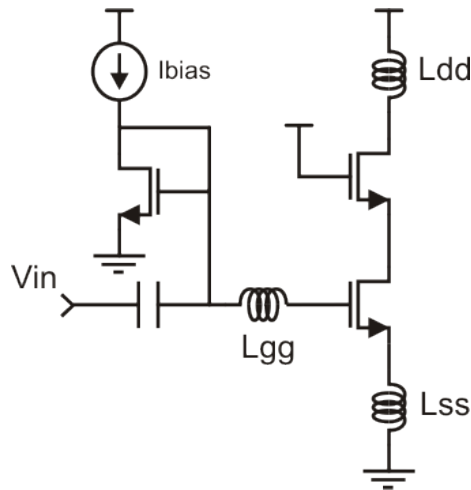


**Figure 2.32: Single-ended cascode LNA using inductive degeneration.**

LNA design can now be simplified to adjusting the transistor width for noise match while keeping minimum gate length for maximum gain. Then, we can adjust  $L_{SS}$  to have real input impedance equal to the source impedance. And finally,  $L_{gg}$  can be chosen to cancel the imaginary part of the input impedance. Thus, impedance and noise matching can “ideally” be achieved.

## 2.5 Mixer

After the received signal is amplified by a low-noise block, a down-conversion mixer is then used to bring the RF signal down to low frequencies. Signal processing at baseband is much easier and economical from the chip area and power consumption point of views. So, the LO generated signal is multiplied by the low-noise amplified RF signal via the mixer, and the signal with frequency difference is filtered at baseband.

### 2.5.1 Main parameters

As Equation 2.19 suggests, the receiver blocks closer to baseband have more effect upon the total linearity. Thus, mixer distortion usually dominates the system non-linearity.

Two noise figure definitions are common in the mixer: single-sideband (SSB) and double-sideband (DSB) noise figures. In non-zero IF systems, the input frequency band includes the required RF signal and maybe another signal at the same distance from the LO signal as that between LO and RF signals. This is called the image frequency. Both

frequencies, the RF and image, can down-convert to the lower IF frequency band, because they're at equal distance from the LO signal (on opposite sides). Noise from both frequency bands down-convert to the same frequency and contribute to the output noise. If we assume a noiseless mixer and useful information exists in the image band as well as the RF band, then the noise factor is  $SNR_{in}/SNR_{out} = (P_i \times N_o)/(P_o \times N_i) = 1$  ( $NF = 0\text{dB}$ ). This is the way how DSB NF is calculated. In the SSB NF calculation, it is assumed that the image band doesn't include useful information (which is the usual case). So, the SNR at the output is doubled, because there is only noise coming from the image band. This will cause the noise factor to be 2 ( $NF = 3\text{dB}$ ). The two situations can be graphically illustrated as in Figure 2.33. Unless otherwise specified, the DSB NF is usually used to define the noise figure of the mixer.

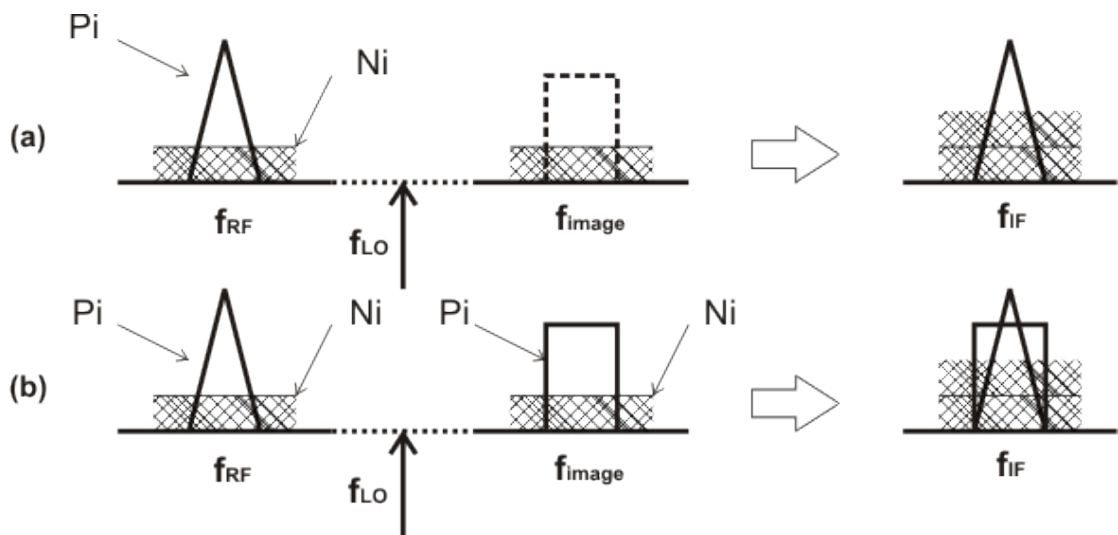


Figure 2.33: Definition of (a) SSB vs. (b) DSB NF.

The input and output signals of the mixer are not at the same frequency. Thus, the conversion gain (CG) parameter is used in the mixer if it is providing gain (otherwise, conversion loss). CG is defined as the ratio of the desired IF output to the value of the RF input at a given LO signal level [16]. CG can be defined in the voltage domain ( $CG_v$ ) or power domain ( $CG_p$ ), and they're related through the ratio of the RF and IF port impedances, as shown in the following equations:

$$CG_v = \frac{V_{IF}}{V_{RF}} \quad 2.22$$

$$CG_p = \frac{V_{IF}^2/R_{out}}{V_{RF}^2/R_{in}} = CG_v^2 \frac{R_{in}}{R_{out}} \quad 2.23$$

Mixer port impedances also should be defined unless the mixer interfaces remain internal to the IC. Isolation between ports is also important. For example, LO signal leaking to the RF port can reach the receiver antenna leading to unwanted signal radiation and additional frequency sidebands through the mixing action. Port-to-port isolation can thus be defined to avoid unwanted feed-through actions in the mixer.

## 2.5.2 Mixer topology

Based on the way mixing is performed, mixers can be divided into three categories: single-ended, singly-balanced and doubly-balanced mixers [16]. Single-ended mixers depend on system non-linearity to generate second-order terms resulting in mixing behavior. This can be implemented using a single MOS transistor, which is characterized by the square law I-V behavior in saturation mode. Single-balanced mixers depend on multiplication in current domain to perform the mixing action [54]. One input (usually the RF signal) is single-ended and the (the LO signal) other is used differentially.

Double-balanced mixers use both input signals differentially to provide better port-to-port isolation. Active implementation of the double-balanced mixer employ two single-balanced mixers combined together. As shown in Figure 2.34, the RF signal is first converted to current in a transconductor. The LO signal is then used to drive the switching transistors. This is equivalent to multiplying the RF current signal with a square wave that depends on the LO signal. The LO signals enter the switching transistors in anti-parallel configuration, which allows the cancellation of all related LO components at the output. The fundamental frequency of the square wave, multiplied by the RF signal, will generate the required difference signal after low-pass filtering. The conversion gain for a square wave input can be calculated as following:

$$CG_v = \frac{g_m \times \frac{4}{\pi} \times R_{out}}{2} = \frac{2}{\pi} g_m R_{out} \quad 2.24$$

where  $g_m$  is the transconductance of the RF transistor. The magnitude of fundamental component of the square wave is  $4/\pi$ , and the factor of 2 is because only the difference component at the output is considered.



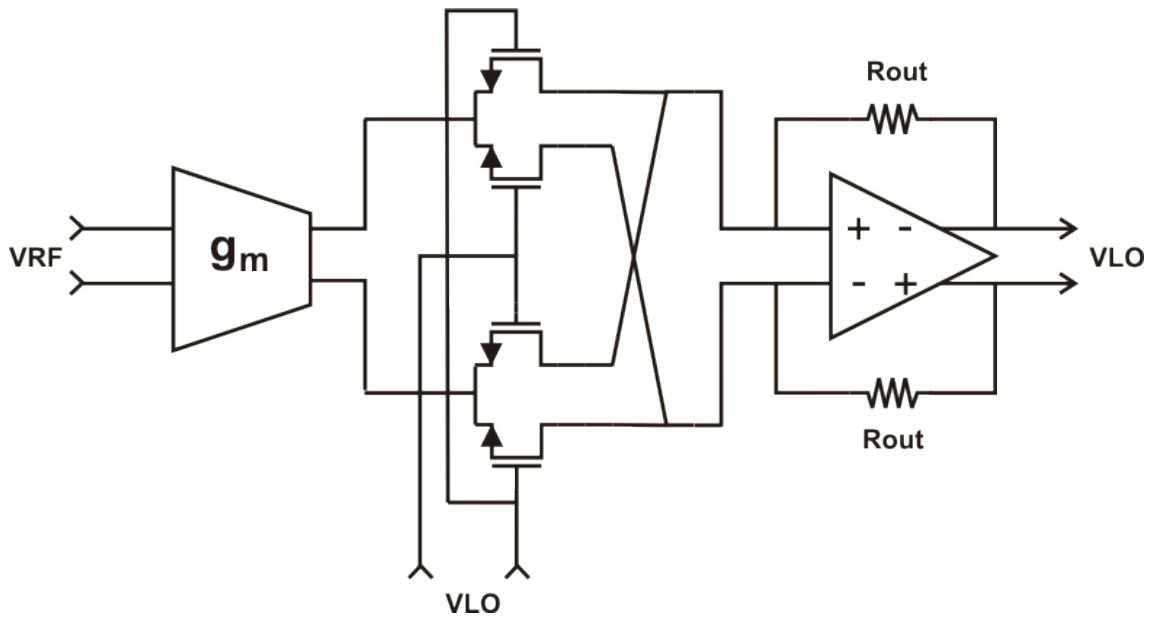


Figure 2.35: Passive implementation of double-balanced mixer [16].

# Chapter 3

# Design and Simulation

# Results

---

Schematic simulations at 60GHz allow the designer to become familiar with a circuit and understand its behavior and changes with different parameters. The pre-layout schematic doesn't really represent actual component values in the final design, and a considerable difference can be expected between measurements and schematic simulation results. Parasitic capacitance and inductance due to interconnects, for instance, are comparable to the designed values but cannot be accurately predicted before post-layout simulations. The design procedure followed in this work includes a few iterations. Firstly, circuit behavior is understood through schematic simulations. Initial design values can be chosen with the help of estimated interconnect parasitic capacitance and realistic values of quality factor for the passive components. A physical layout can then be drawn and post-layout results analyzed. Active and passive component values are then optimized, the layout is modified and post-layout results are again analyzed. This process is repeated few times until an optimum design is reached.

The circuit is designed in UMC 90nm CMOS technology with thick (3.25 $\mu$ m) top metal. The supply voltage is determined to be 1V in order to have the opportunity to reuse the circuit in a 40nm process.

In this chapter, an evaluation of the active and passive elements used in the technology is first shown. Schematic simulation results for all of the circuit blocks are then presented. This includes the QVCO, LO buffer, divider chain, LNA and mixer blocks.

## 3.1 $f_T$ of the 90nm NMOS transistor

Transit frequency ( $f_T$ ) of a transistor determines the region of operation according to the frequency used.  $f_T$  can be calculated using the hybrid parameters. A NMOS transistor is tested at 60GHz using the following equation:

$$f_T = 60e9 \times h_{21} \quad 3.1$$

where  $h_{21}$  is the short circuit forward current gain. Transit frequency versus the drain current density of the NMOS transistor at minimum (80nm) gate length is shown in Figure 3.1. Maximum transistor  $f_T$  is 135GHz, which is close to the operating frequency. This shows that operation at 60GHz using this process is possible, but high transistor intrinsic gain ( $g_m \times r_o$ ) is not expected.

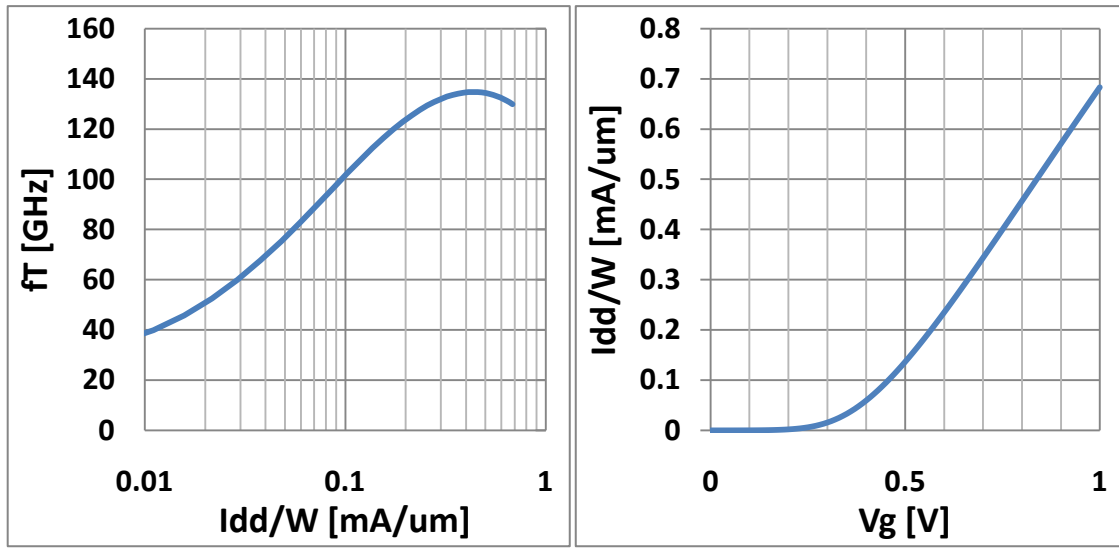


Figure 3.1: (a) Transit frequency of the used 90nm transistor, and (b) Drain current density vs. gate voltage.

## 3.2 Passive elements

Passive elements used in the circuit include poly resistors, diodes, metal-oxide-metal (MoM) capacitors, varactors, transmission lines, inductors and transformers. Resistors, diodes and MoM capacitors are well characterized in the available technology. Inductors and transformers are only characterized up to 20GHz. Furthermore, not all of the values needed in the design are covered by the available components. Thus, varactors, transmission lines, inductors and transformers are designed independently, and presented in the following sub-sections. ADS-Momentum<sup>®</sup> [18] is used to simulate all the inductive elements.

### 3.2.1 Varactors

Inversion-mode MOS varactors are used in this design. Capacitance variation and quality factor with tuning voltage for the minimum length varactor are shown in Figure

3.2a and Figure 3.2b, respectively. The finger width (W) used is 1 $\mu$ m and 20 fingers (i.e., M=20) are used for each transistor. Measured quality factor is expected to be lower than the simulated value due to the lack of an accurate model at 60GHz and the presence of interconnect parasitic resistance. Thus, margin should be added to the design or additional resistance should be added to the schematic in order to account for the reduced quality factor.

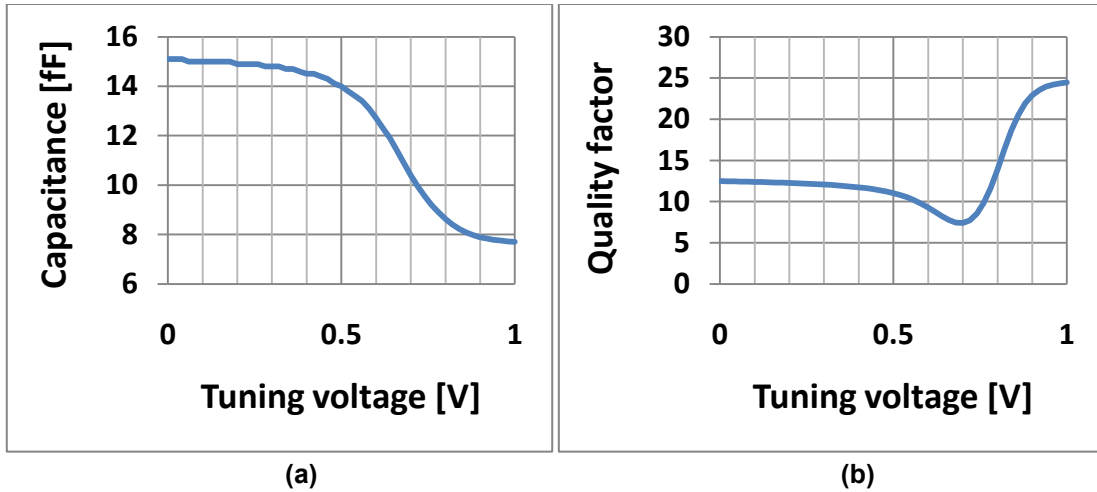


Figure 3.2: (a) Capacitance and (b) quality factor for a varactor with W=1 $\mu$ m and M=20.

### 3.2.2 Transmission lines

Coplanar waveguide over ground plane are used to implement 50 $\Omega$  transmission lines (TLs). Transmission lines with 50 $\Omega$  characteristic impedance ( $Z_c$ ) are needed for the chip output signals at high frequencies. Single-ended transmission lines are going to be used in the QVCO and divider subsystem of section 4.2, which has output signals at 30GHz. The TL configuration and unit-element (1 $\mu$ m length) lumped RLCG model are shown in Figure 3.3a and Figure 3.3b, respectively. The TL is implemented using top-metal with a width (W) of 2 $\mu$ m and spacing (S) of 4 $\mu$ m.  $Z_c$  is calculated using the following equation:

$$Z_c = Re(\sqrt{B/C}) \quad 3.2$$

where B and C are the transmission line ABCD-parameters. Characteristic impedance as a function of frequency is shown in Figure 3.4. A value of 48.5 $\Omega$  was achieved for  $Z_c$  at 30GHz.

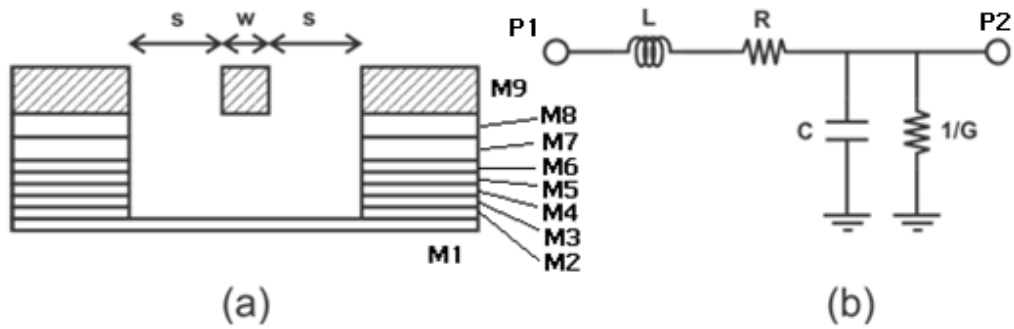


Figure 3.3: Transmission line (a) cross-section and (b) RLCG model.

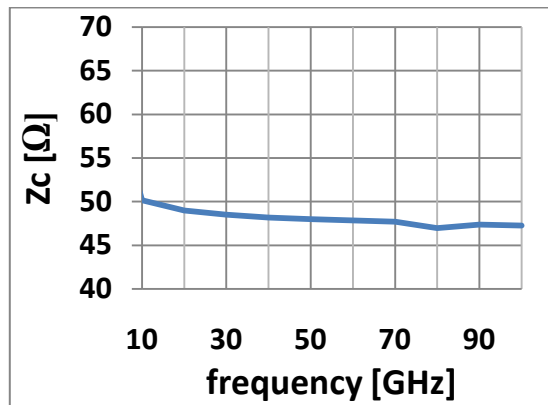


Figure 3.4: Single-ended TL characteristic impedance vs. frequency.

### 3.2.3 Inductors

Differential inductors are used in different blocks in our circuit. Differential inductance values from 40pH to 300pH are implemented. The smallest inductance is used in the QVCO (section 3.3) and maximum size one is used in the first stage of the 60GHz frequency divider (section 3.4). A 5x5um stack of technology metal layers is used as a unit element for the chip ground plane. The square ground cell should pass the layout design-rule checks. Square inductors are implemented, shielded with ground cells during simulation to minimize the effect of other components on the inductor layout. For example, the 300pH inductor has 2 turns with  $W$  of 3um,  $S$  of 2um and an outside dimension (OD) of 48um. The inductance ( $L$ ) is calculated by dividing the imaginary part of the differential input impedance by the angular frequency. The quality factor ( $Q$ ) is calculated by dividing the imaginary part of the differential input impedance by its real part. The simulated inductance and quality factor for the 300pH inductor is shown in Figure 3.5. A quality factor value of 13.3 is predicted at 60GHz. The inductor is self oscillating at a frequency close to 100GHz. That's why the inductance shows an

increasing behavior with frequency. The self-resonance frequency is increased at lower inductor sizes due to the lower parasitic capacitance. The lumped model used in schematic simulations is shown in Figure 3.6. Note that in this model, the total differential inductance is  $2L$ .

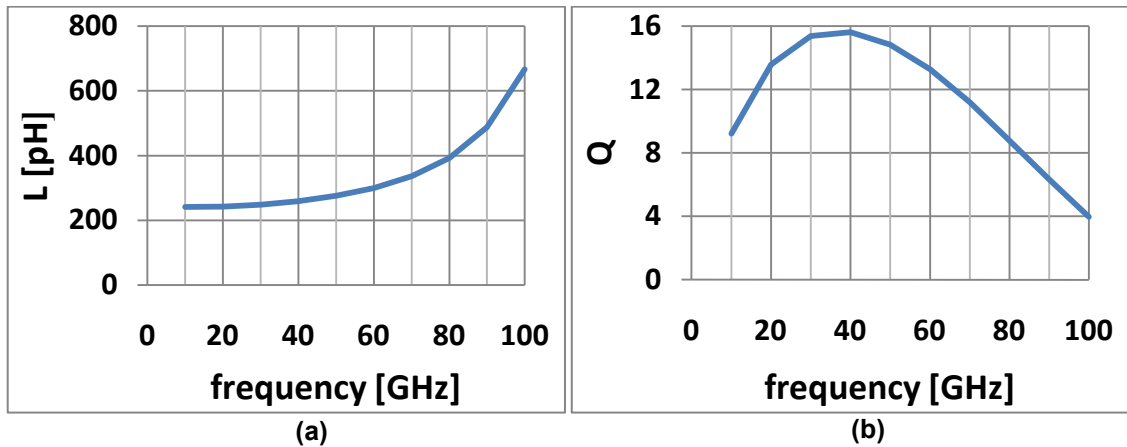


Figure 3.5: (a) Inductance and (b) quality factor of the 300pH differential inductor.

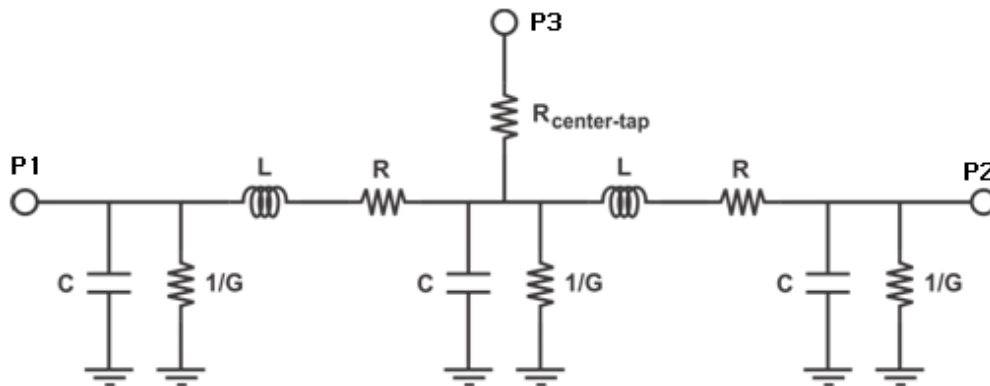


Figure 3.6: Differential inductor lumped component model.

### 3.2.4 Transformers

Two metal layers are used to implement the transformer. These are metal layer 9 (M9) and metal layer 8 (M8). The top metal layer (M9) is 3.25 $\mu\text{m}$  thick with a sheet resistance of 7m $\Omega$ /square. M8 is 0.5 $\mu\text{m}$  thick with a sheet resistance of 44m $\Omega$ /square. The inductor only uses M9. Thus, Transformers are usually implemented with lower quality factors compared to inductors. Figure 3.7 shows an 83pH transformer. The transformer turns ratio is 1:1, so the primary and secondary inductance values are the same. The 83pH transformer is implemented with two turns, W of 3 $\mu\text{m}$ , S of 2 $\mu\text{m}$  and OD of 28 $\mu\text{m}$ . This is the smallest size transformer implemented in this work, which is

used in the LNA and mixer combination (see section 3.5). The test-bench used to predict the transformer parameters is shown in Figure 3.8. The mutual inductance ( $M$ ) is calculated by dividing the imaginary part of  $Z_{21}$  (numbers refer to the differential ports in the test-bench) by the angular frequency. The coupling coefficient ( $k$ ) is calculated as:

$$k = M / \sqrt{L_1 L_2} \quad 3.3$$

where  $L_1$  and  $L_2$  are the imaginary parts of  $Z_{11}$  and  $Z_{22}$  divided by the angular frequency, respectively. Simulation results are shown in Figure 3.9. A quality factor of 7.91 and coupling coefficient of 0.73 are achieved at 60GHz. The lumped model used in schematic simulations is shown in Figure 3.10.

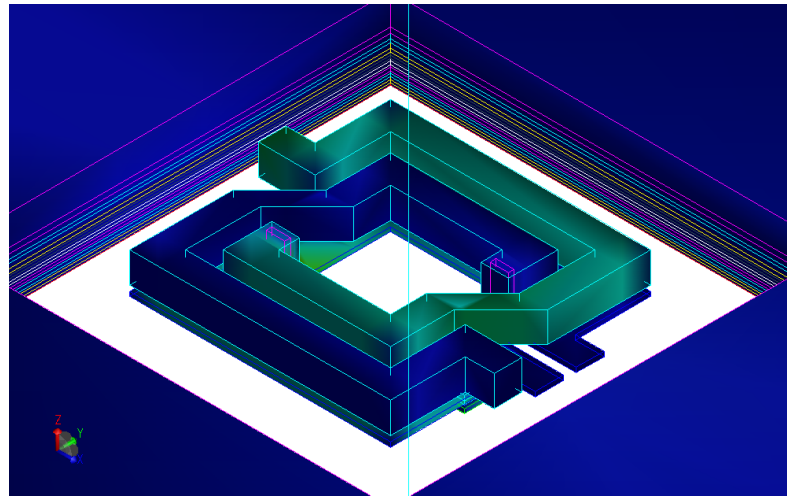


Figure 3.7: Transformer implemented with 83pH primary (=secondary) inductance in 90nm process.

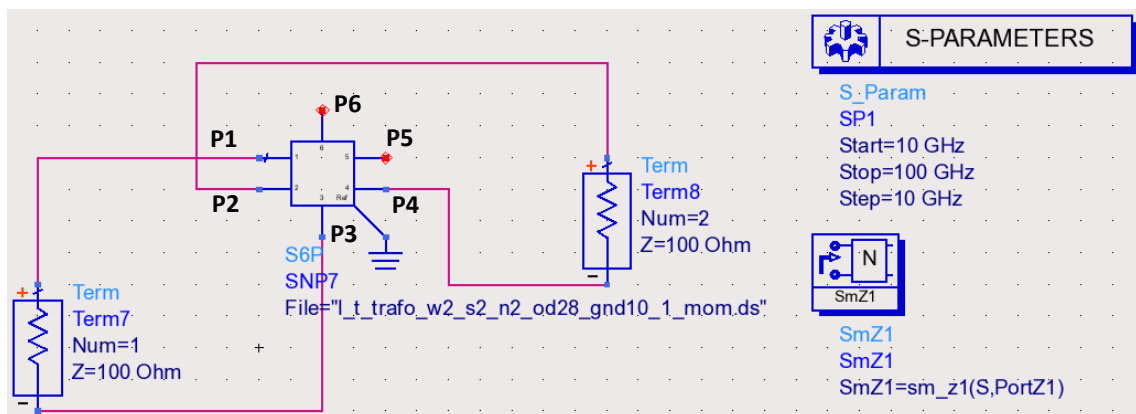


Figure 3.8: Testbench used for the prediction of transformer parameters.

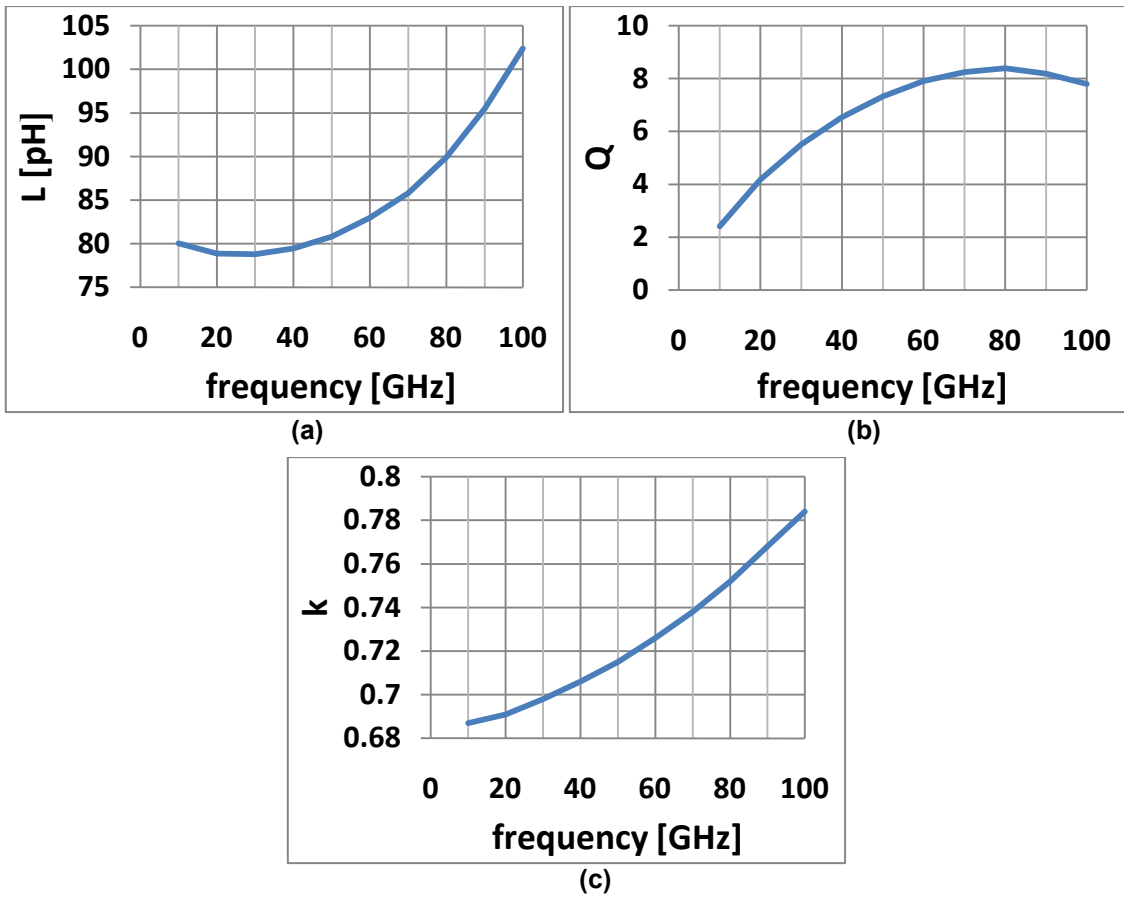


Figure 3.9: (a) Inductance, (b) quality factor and (c) coupling coefficient of the 83pH transformer.

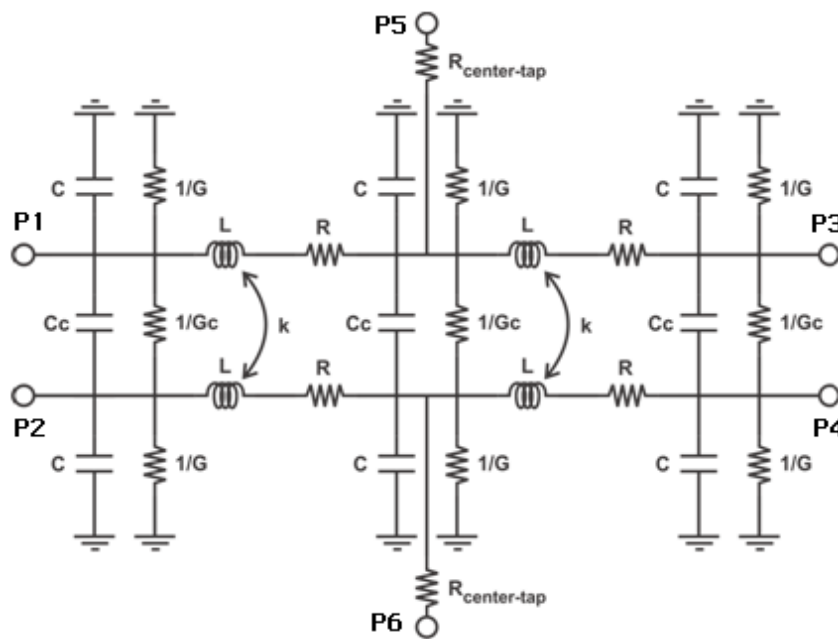


Figure 3.10: Transformer lumped component model.

### 3.3 QVCO and LO buffer

The aim of this section is to design a quadrature VCO and LO buffer stage. Target specifications for the QVCO and LO buffer blocks are shown in Table 3.1. More emphasis was put on the phase noise spec by the system designer. So, a low phase noise ( $<-90\text{dBc/Hz}$ ) QVCO is the first priority. The starting point of target phase noise spec is the  $-85\text{dBc/Hz}$  achieved in [13].

**Table 3.1: QVCO and LO buffer target specifications.**

Parameter	Value
Maximum phase noise	$-90\text{dBc/Hz @ 1MHz offset}$
Center frequency	60.5GHz
Minimum tuning range	8GHz
Maximum power consumption	30mW
Minimum voltage swing	1V-pp (rail-to-rail)

#### 3.3.1 Circuit schematic

The schematics of the P-QVCO and LO buffer are shown in Figure 3.11 and Figure 3.12, respectively. Two similar LO buffers are used for both in-phase and quadrature oscillator outputs. Results of a bottom-series QVCO (BS-QVCO) are going to be compared with the parallel QVCO (P-QVCO). The schematic of the BS-QVCO used is shown previously in Figure 2.15b. Unless otherwise specified, the MOSFET finger width is  $1\mu\text{m}$ .

#### 3.3.2 Circuit operation

As shown in Figure 3.11, a modified P-QVCO can be used to lower the phase noise. The circuit uses external gate bias for the active cross-coupled transistor pair to improve the phase noise performance [38].



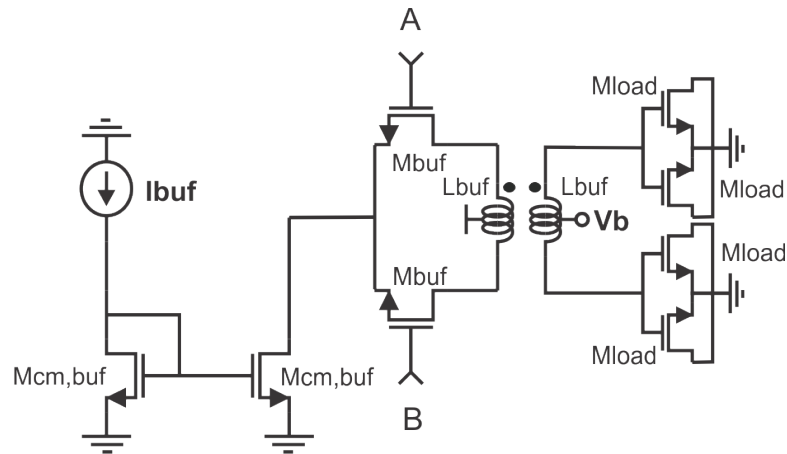


Figure 3.12: Circuit schematic of the transformer-coupled LO buffer with output load.

### 3.3.2.1 External gate bias

In a normal cross-coupled LC VCO, the gate of one transistor is connected to the drain of the other, representing the two differential VCO outputs. This can easily take the transistor out of saturation when the peak differential output signal goes above the threshold voltage (in this case, condition of a transistor being in saturation is  $V_g - V_d < V_{th}$ ). When the gate bias is independently reduced, gate-to-drain maximum voltage is reduced, allowing greater voltage swings with active transistors in saturation. This is shown graphically in Figure 3.13.

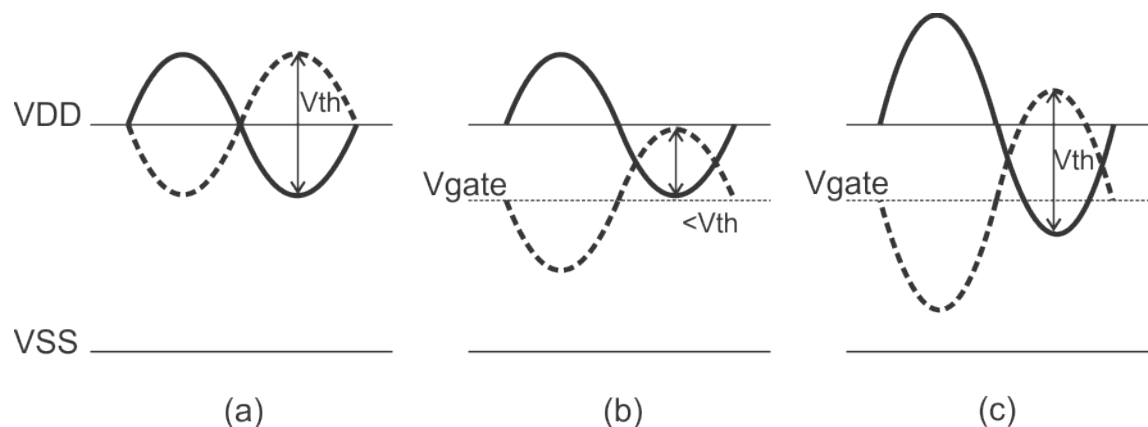


Figure 3.13: QVCO (a) without (b) with external gate bias, and (c) higher swing possibility without taking the cross-coupled transistors out of saturation.

External bias of the active cross-coupled pair is implemented through the use of gate decoupling capacitors ( $C_d$ ) and biasing resistors ( $R_d$ ).  $C_d$  is implemented using metal-

oxide-metal (MOM) capacitors.  $R_d$  is implemented using P+ poly resistors. This can partially load the VCO output through parasitics of active transistors. However, the improved phase noise performance due to the independent gate bias encourages using it.

### 3.3.2.2 Modal determinism

In a quadrature-VCO, two modes of oscillation can occur when the oscillator is switched on [56]. This depends on the quadrature signal, either leading or lacking the in-phase signal by  $90^\circ$ . A detailed mathematical analysis was performed on the QVCO to derive its two modes [57]. The analysis predicts a fast, high frequency, mode and a slow mode. Owing to the asymmetry in the tank impedance due to the difference between the inductor and varactor quality factors, one frequency mode usually dominates the other. A figure illustrating the two modes' impedance points on the tank impedance curve is presented in Figure 3.14. The QVCO tends to oscillate at the higher tank impedance mode. The difference between the two tank impedance modes should be large enough to ensure operation at one of them. A higher coupling coefficient operates the QVCO at tank impedance points with a larger difference in value. This explains the need for higher coupling coefficient to ensure modal determinism. A higher coupling coefficient also increases the effective  $G_m$  and improves the oscillation margin which is required for the oscillator to start up. However, phase noise is degraded by a higher coupling coefficient. Thus, variable coupling can be implemented to achieve all requirements. When switching on the oscillator, a high coupling coefficient is used for the startup. Then a low value is selected for lower phase noise.

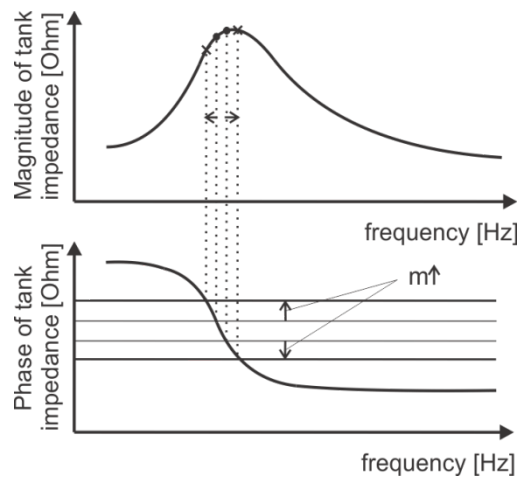


Figure 3.14: Impedance points of the QVCO two oscillation modes [57].

### 3.3.2.3 Variable coupling

Variable coupling is implemented using three transistors. One fixed small coupling transistor ( $M_{q1}$ ) and a larger switching coupling transistor ( $M_{q2}$ ). When the switch is ON,  $M_{q2}$  is in parallel with  $M_{q1}$ , giving a high value of coupling coefficient. Two transistors are used to implement variable coupling instead of one in order to ensure quadrature locking at all values of the switching voltage.

### 3.3.2.4 Digital varactor

There is a tradeoff between tuning range and phase noise using a single varactor. A digitally controlled varactor using a bank of binary weighted sizes can be used. As mentioned earlier in section 2.1.3, noise in active elements can easily be transformed into phase noise by the tank varactor due to its sensitivity to amplitude variations. The oscillator's sensitivity to the varactor can be reduced by using a smaller varactor size ( $K_v = \Delta C / \Delta V$ ). This improves AM-to-FM conversion, and thus, reduces translated phase noise components in the circuit [58], [34]. The analog varactor should be larger than the minimum digital varactor size. This is to overcome process variations and ensure overlapping frequency ranges.

### 3.3.2.5 Current mirror

A cascode current mirror is used to implement a high output resistance. This is useful to reduce the noise generated in one of the cross-coupled pair transistors while the other is OFF, as mentioned in section 2.1.3. Lengthening the current mirror transistors reduces flicker noise. Further increase of the tail transistor length, with its width set to the maximum value (limited by layout), to increase the output resistance causes less current copy ratio. This is because of the reduced aspect ratio ( $W/L$ ), which leads to an increase in the common gate-source voltage of the current mirror transistors and the drain-source voltage of the diode-connected one. The drain-source voltage of the tail transistor, on the other hand, is controlled by the supply. Due to the limited headroom available from the 1V supply, tail transistors are working on the edge of saturation.

## 3.3.3 Design guidelines

For oscillator design at 60GHz, the following equation should be used:

$$60 \times 10^9 = \frac{1}{2\pi\sqrt{LC}} \quad 3.4$$

where L and C are the total inductance and capacitance values, respectively, seen at the output of the oscillator. The total output capacitance is due to several components including the cross-coupled transistor pair, parallel coupling transistors, varactor, buffer load and interconnect parasitics.

### 3.3.3.1 Cross-coupled pair

More transconductance is required from the cross-coupled transistor pair (gm,c) to start-up the oscillation with sufficient margin. However, its width (Mc) can't be increased so much to keep a room for other capacitance components to tune the resonator. Thus, a good balance between different capacitive components is required for the oscillator. Mc was, thus, chosen to be 40um.

### 3.3.3.2 Digital varactor

Four digitally-controlled inversion-mode MOS capacitors are chosen to provide a discrete frequency step for the VCO. Sizes of the digital varactors are binary-weighted to cover the overall frequency range. The finger width of a transistor is a trade-off between input resistance and capacitance values. The finger width used in the varactor is 0.5um, which is the minimum finger width available from the technology. This improves varactor quality factor at the expense of lower tuning range at the same center frequency. The larger the size of the varactor is, the larger the tuning range. However, this loads the VCO output and causes a drop in the center frequency at the same inductance value. Varactor sizes of 24um, 48um, 96um and 192um, with an analog varactor of 36um, are used to provide a tuning range of 8GHz centered at 60GHz (i.e., 13.3%). This is limited by the minimum possible inductance value.

### 3.3.3.3 Differential inductor

The smallest inductor is 2um wide, 18x18um half-turn (i.e., U-shaped) to connect the two drains of the cross-coupled transistor pair. The minimum inductance was found to be around 40pH with a quality factor of 14.2. An initial value of 45pH with a quality factor of 15 was used in the schematic. A small inductor is required at 60GHz to compensate the large capacitance value at the VCO due to the previously mentioned

contributors. With the chosen inductor, transistor size and varactors, a tuning range of 8GHz with 500MHz step size is simulated.

### 3.3.3.4 Quadrature coupling

Coupling transistor  $M_q$  should be small to represent a small coupling coefficient for improved phase noise. Minimum coupling coefficient of 0.1 is chosen. With  $g_{m,c}$  of 30mS, this requires that  $g_{m,q}$  is 3mS, which gives a value of 4 $\mu$ m for  $M_q$ . A very small value for the transistor width can cause more mismatch ( $\sigma \propto 1/\sqrt{WL}$ ) [17]. Also contribution of transistor flicker noise is high at lower transistor widths. A value of 6 $\mu$ m is chosen for lower flicker noise contribution of  $M_q$  and better mismatch. This gives a minimum coupling coefficient of 0.15.  $M_{q2}$  in combination with  $M_{sw}$  give the second part of the coupling coefficient. The switching transistor works in triode, and can be replaced by a resistor. The effective coupling transconductance when the switch is ON can be written as:

$$g_{m,q,eff} = g_{m,q} + \frac{g_{m,q2}}{1 + g_{m,q2} \times R_{sw}} \quad 3.5$$

Where  $g_{m,q,eff}$  is the total effective coupling transconductance,  $g_{m,q}$  is the fixed coupling transconductance,  $g_{m,q2}$  is the variable coupling transconductance and  $R_{sw}$  is the switch transistor equivalent resistance.  $M_{q2}$  should be large to have a better margin of oscillation startup and modal determinism. A large  $M_{q2}$  also adds capacitance to the QVCO output, which shifts the oscillation frequency to lower values. As  $M_{q2}$  is only used to ensure appropriate startup, a maximum coupling factor of 0.7 is chosen. This leads to a value of 21mS for  $g_{m,q,eff}$  (this value is based on the simulator). With a large enough switching transistor to ensure low  $R_{sw}$ ,  $M_{q2}$  can be determined according to the resulting  $g_{m,q2}$  value. For  $M_{sw}$  of 48 $\mu$ m,  $R_{sw}$  is 9.7 $\Omega$  and  $g_{m,q2}$  is 21mS, leading to a value of 18 $\mu$ m for  $M_{q2}$ .

### 3.3.3.5 Current mirror

Wide channel transistors are required in the current mirror in order to have the best possible current copy ratio and to decrease flicker noise. The limited headroom available from the 1V supply and the reduced gate voltage for better phase noise performance caused a small value (around 140mV) of  $V_{ds}$  to be available for tail transistors. This caused around 7mA only to be copied from a 10mA current source (30% current loss in the current mirror). A value of 208 $\mu$ m total width was chosen for

the current mirror transistors (Mcm). The maximum number of fingers of a transistor in the used technology is 32. With a finger width of 1 $\mu$ m, 8 parallel transistors of 26 $\mu$ m each were used to implement one 208 $\mu$ m current mirror transistor. Even number of fingers was suggested in the technology for the best matched transistor layout.

### 3.3.3.6 Current source

Two current sources, 10mA each, feed the QVCO through the cascode current mirror. As explained in section 2.1.2, the VCO operation is divided into current-limited and voltage-limited regimes according to the bias current. As shown in Figure 3.15, the output amplitude is proportional to the bias current in the current-limited regime. This leads the phase noise to decrease with increasing the bias current as expected from the phase noise equation (Equation 2.9). In the voltage-limited regime, the tail transistor goes into the triode region and the output amplitude is almost constant, limited by the power supply. Operation in the voltage-limited regime is usually not desirable, because the bias current is wasted without an effective increase in the output amplitude. Moreover, the higher current leads to a higher transconductance (higher noise current), which degrades the phase noise. Thus, the VCO should operate on the edge of the voltage-limited regime in order to have the best phase noise without wasting the bias current.

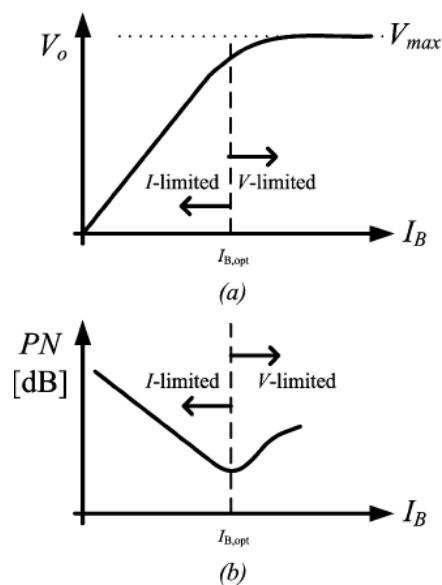


Figure 3.15: Current and voltage-limited regimes with the bias current as a variable [59].

### 3.3.3.7 Output voltage swing

One drawback of high output voltage swing in the VCO is the reduced possible tuning range [60], [34]. The capacitance value at a specific varactor bias is averaged due to the time varying oscillation amplitude, as shown in Figure 3.16a. As shown in Figure 3.16b, effective capacitance causes the actual tuning curve to be smoother than the DC varactor characteristics. Higher amplitude causes less tuning sensitivity, and thus, lower available tuning range. That's because available tuning voltage is limited by the supply. This effect can be shown in Figure 3.17. Thus, output amplitude should be kept in the current-limited regime, as a compromise between phase noise and tuning range. In our circuit, maximum output swing in the QVCO (before the LO buffer) was kept around 250mV.

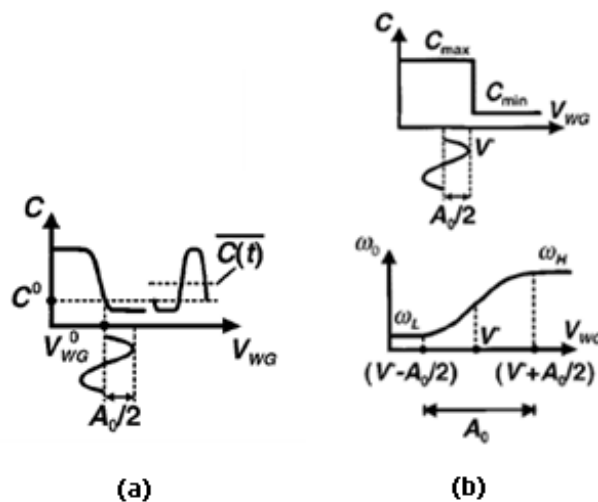


Figure 3.16: (a) Average capacitance value and (b) effective capacitance curve for a varactor in a VCO [60].

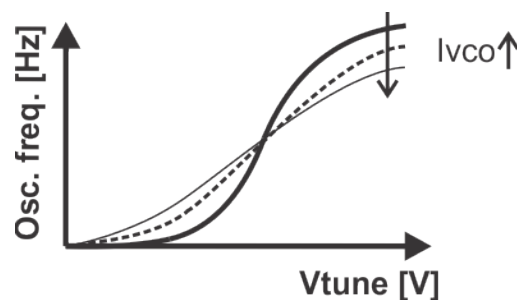


Figure 3.17: Less tuning frequency with higher current due to different effective capacitance values at different amplitudes.

### 3.3.3.8 External gate bias

The cross-coupled transistor pair gate voltage ( $V_{gate}$ ) should be lower than the supply voltage, to keep transistors in saturation (for peak differential amplitudes higher than  $V_{th}$ ) and improve phase noise.  $V_{gate}$  also controls the common source node of the cross-coupled pair, which is the headroom for the tail transistor. Low headroom can get the tail transistor out of saturation. The tail transistor will fail to work as a high impedance current source. This leads the phase noise to, again, start increasing. So,  $V_{gate}$  was chosen to be 0.6V as a trade-off between phase noise and tail transistor headroom.

### 3.3.3.9 LO buffer transistor size

The LO buffer transistor size ( $M_{buf}$ ) should be kept as small as possible not to load the VCO output. However, large buffer size is required for large transconductance ( $g_{m,buf}$ ) to overcome the buffer load resistance. The LO buffer load resistance also depends on the following stage. In our circuit, we simulate using large buffer load transistors (two parallel transistors with 20um total width each). This is to simulate the large-size input transistors of the first-stage divider. The LO buffer gain is due to the multiplication of  $G_m$  and  $R_{out}$ .  $R_{out}$  includes the buffer transistor output resistance, which is inversely proportional to the width. So, as the buffer size is increased,  $G_m$  is increased and  $R_{out}$  is decreased. The buffer gain will, thus, increase to the point at which the reduction in  $R_{out}$  is more dominant. So, there is an optimum width for the buffer transistors to get maximum gain at a specific load. In our circuit, we chose  $M_{buf}$  to be 14um. This value is still below the optimum value for maximum gain. However, a compromise between buffer gain (controlling output voltage swing) and QVCO loading (controlling center frequency and tuning range) was considered.

### 3.3.3.10 LO buffer configuration

The LO buffer can either be an inductively-tuned or a transformer-coupled CS differential amplifier, shown previously in section 2.2. The selection between both configurations depends on the buffer load. Capacitive part of the load can be compensated by the inductor or the transformer. Resistive part of the load, however, always contributes to the reduction of the buffer gain, and can only be overcome by the buffer transconductance. In the transformer-coupled choice, the load resistance is transferred to the buffer transistor drain terminal with a higher value. This improves the

resistive contribution of the load transistor to the total buffer output resistance (see equations 2.11 and 2.16). However, a transformer is usually implemented with a low quality factor, as compared to the differential inductor. In this technology, differential inductors with  $Q$  of around 15, and transformers with  $Q$  of around 8 and coupling coefficient of 0.8 were implemented. The transformer implemented for this circuit is a 160pH one with 2 turns,  $W$  of 2 $\mu$ m,  $S$  of 2 $\mu$ m and OD of 32 $\mu$ m. Lower quality factor is equivalent to a lower parallel resistance, which degrades the resistive contribution of the inductive component to  $R_{out}$ . So, depending on the effective buffer output resistance at a specific load, a choice can be made between both configurations. In our circuit, a large 40 $\mu$ m width transistor was chosen to load the LO buffer. That would degrade  $R_{out}$  if connected directly to the buffer output. Thus, a transformer-coupled CS differential amplifier was chosen to load the QVCO.

### 3.3.4 Design values

All transistor sizes, passive values and controlling parameters are listed in Table 3.2. Finger width of all transistors is 1 $\mu$ m except for the digital varactor which has a 0.5 $\mu$ m width.  $M$  defines the number of fingers and  $L$  is the channel length.

**Table 3.2: Design values for the QVCO and LO buffer.**

Transistor sizes						
Parameter			P-QVCO	Reduced load	BS-QVCO	Reduced load
Cross-coupled pair ( $M_c$ )	M		40			
	L		80nm			
Fixed coupling ( $M_q$ )	M		6	6	30	30
	L		180nm			
Variable coupling ( $M_{q2}$ )	M		18		×	×
	L		80nm		×	×
Switch transistor ( $M_{sw}$ )	M		48		×	×
	L		100nm		×	×
Digital varactor ( $W=0.5\mu$ m)	Md1	M	96			
		L	80nm			
	Md2	M	48			
		L	80nm			
	Md3	M	24			
		L	80nm			

	Md4	M	12			
		L	80nm			
Analog varactor (Mv) (W=0.5um)		M	18			
		L	80nm			
QVCO Current mirror (Mcm)		M	208			
		L	200nm			
QVCO Current source (Mcs)		M	72			
		L	200nm			
Buffer transistor (Mbuf)		M	14			
		L	80nm			
Buffer current mirror (Mcm,buf)		M	208			
		L	300nm			
Load transistor (Mload)		M	20	12	20	12
		L	80nm			
<b>Passive elements' values</b>						
QVCO differential inductor		Lvco	45pH			
Gate decoupling capacitor		Cd	540fF			
Gate biasing resistor		Rd	3k $\Omega$			
Buffer transformer (primary = sec.)		Lbuf	160pH	230pH	160pH	230pH
<b>Controlling parameters</b>						
External gate voltage		Vgate	0.6V		×	×
QVCO bias current		Ivco	10mA	10mA	5mA	5mA
Buffer bias current		Ibuf	5mA			

### 3.3.5 Simulation results of P-QVCO

In the following section, the schematic simulation results of the designed P-QVCO and transformer-coupled LO buffer combination are plotted. An ideal inductor with an estimated Q of 15 was used in the QVCO. An additional capacitance of 10fF was added at each node of the circuit to simulate the parasitic capacitance that is expected to be added after layout.

#### 3.3.5.1 Amplitude and tuning range

Figure 3.18 shows the P-QVCO single-ended peak output amplitude (A) over the whole tuning range. A plot of the LO buffer output voltage swing (Abuf) is also plotted on the same graph. A peak of around 0.42V at the buffer output is achieved at a 40um

transistor load. This corresponds to 0.84V peak-to-peak, which is acceptable compared to the rail-to-rail (1V) requirement. Note that output amplitudes increase with smaller transistor sizes for the load. So, a comparison with a smaller-size load will be shown in section 3.3.5.6.

The oscillation frequency is plotted on the x-axis. It shows that a tuning range of 8GHz centered at 60.8GHz is achieved (from 56.8GHz to 64.8GHz). The full 8GHz are divided into 16 sub-ranges, 500MHz each, by the four digital varactors.

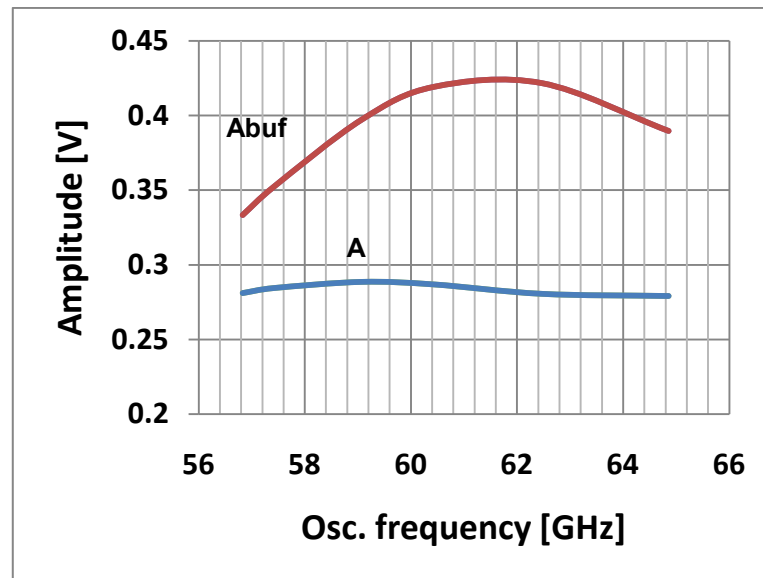


Figure 3.18: P-QVCO and LO buffer amplitudes vs. oscillation frequency.

### 3.3.5.2 Phase noise

As shown in Figure 3.19, the phase noise at 1MHz offset (fd) changes from -98.9dBc/Hz to -94.8dBc/Hz over the tuning range. Phase noise performance shows some degradation at higher oscillation frequencies. Apart from the reduced amplitude, the degradation in phase noise is attributed to the lower equivalent tank capacitance (higher oscillation frequency) as expected from Equation 2.9. Moreover, the buffer input resistance, which loads the oscillator tank, is reduced due to the feedback caused by the gate-drain capacitance ( $C_{gd,buf}$ ) of the buffer transistor ( $M_{buf}$ ). One way to improve the phase noise is to use neutralization capacitors [61] to cancel the effect of  $C_{gd}$ . This improves the oscillator output amplitude and phase noise. This will be shown in section 4.2.

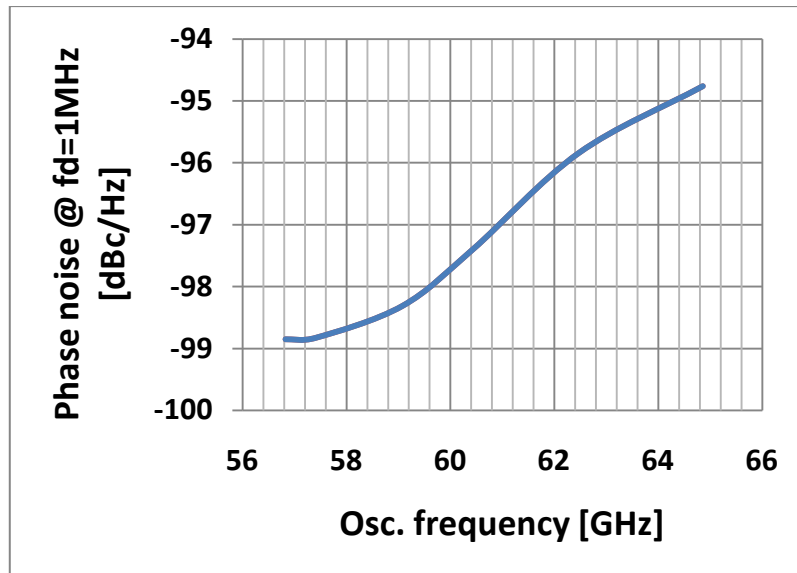


Figure 3.19: Phase noise at 1MHz offset vs. oscillation frequency.

### 3.3.5.3 Variations with tail current

The overall circuit operation was optimized at a 10mA tail current. Figure 3.20a shows the amplitude increase with the QVCO bias current ( $I_{vco}$ ). The voltage-limited regime can be recognized at around 20mA. Operation at 10mA is chosen to meet both power consumption and tuning range specifications. As mentioned in section 3.3.3.7, tuning range is reduced with higher voltage swings (higher bias current at the same circuit design values). This can be shown in Figure 3.20b.

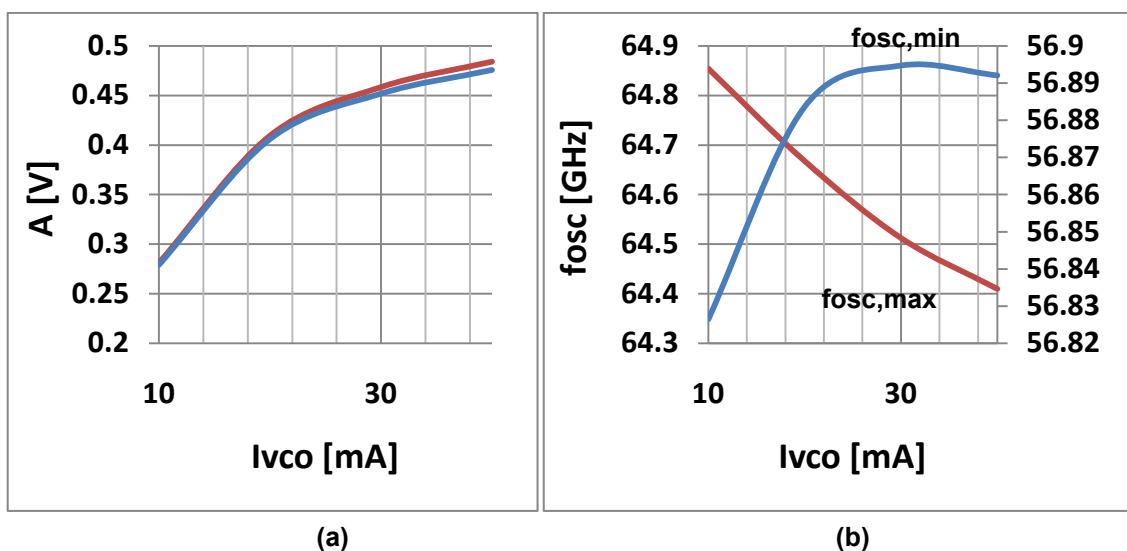


Figure 3.20: (a) A at max. and min. oscillation freq. (b) Max. and min. oscillation frequency variations with QVCO bias current.

Figure 3.21 shows phase noise degradation with higher bias current. The phase noise is best at the beginning of the voltage-limited regime in Figure 3.15. This is the AM-to-FM phase noise component. In our circuit, the overall phase noise is optimized at 10mA. Phase noise keeps degrading in the voltage-limited regime. In that region, current is consumed without an effective increase in the amplitude. Higher current causes an increase in transistor gm. This leads to higher contribution of a transistor noise to the overall phase noise.

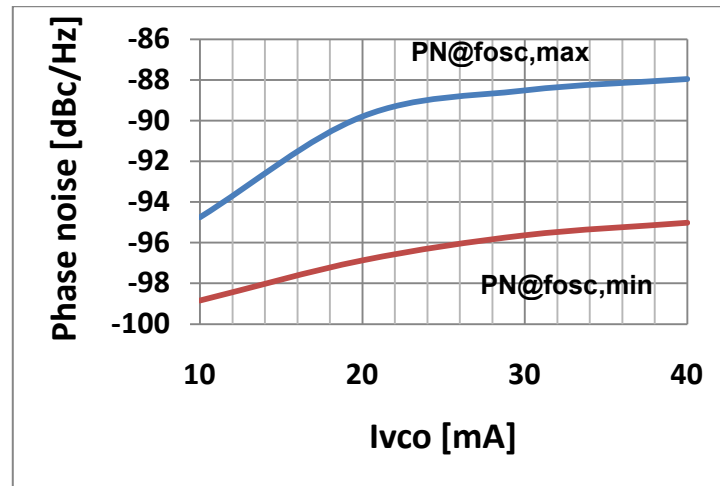


Figure 3.21: Phase noise variations at max. and min. oscillation frequencies with QVCO bias current.

#### 3.3.5.4 Variations with gate voltage

Circuit performance with different gate voltages is shown in Figure 3.22. More gate bias increases the common-source node voltage of the cross-coupled pair. When this leads to an increase in the tail current (due to higher Vds), output amplitude is increased. Total phase noise is minimized at 0.6V. Higher gate voltage takes the cross-coupled pair out of saturation. Lower gate voltage takes the tail transistor out of saturation. Both leads to an increase in phase noise as mentioned in section 3.3.2.

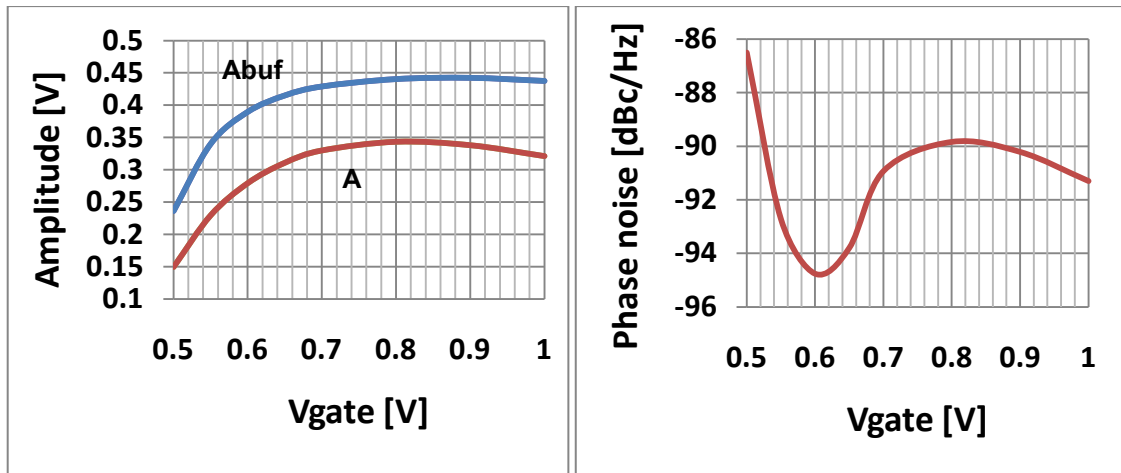


Figure 3.22: Amplitude and phase noise variations with external gate bias at maximum oscillation frequency.

### 3.3.5.5 Variations with supply voltage

Supply voltages up to 1.2V are available for this process. Figure 3.23 shows how the circuit behaves at different supply voltages (all other parameters are constant). Lower supply voltages lead to lower headroom for the tail transistor. This leads to lower tail current and, thus, lower amplitudes. Phase noise is expected to increase with reduce voltage swings as clear from the plot. At 1.2V supply, amplitude is also reduced. This is because the gate voltage is kept constant while the common-source node is increased. This leads to a reduction in the downward gate swing before switching the cross-coupled pair transistor off.

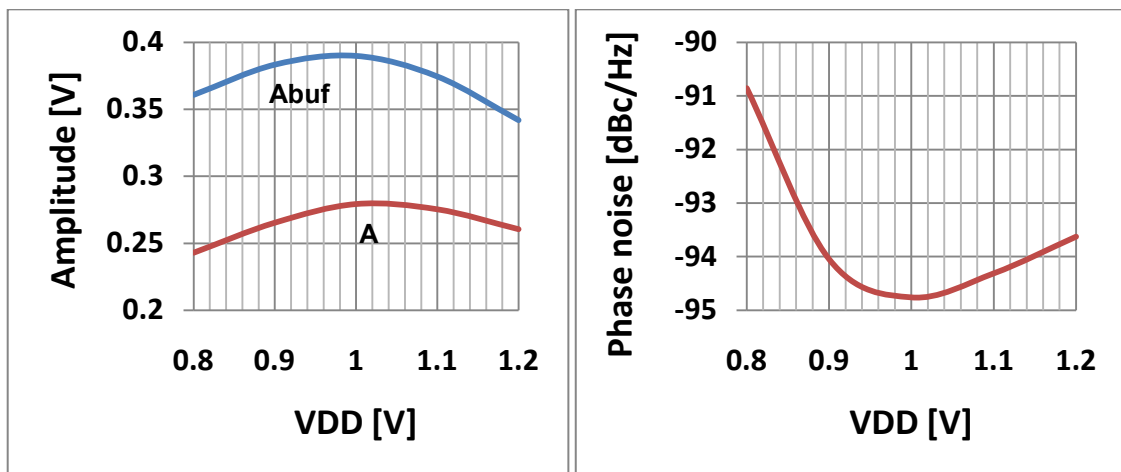


Figure 3.23: Amplitude and phase noise variations with supply voltage at maximum oscillation frequency.

Low gate bias prevented the QVCO performance to be improved at 1.2V supply voltage. So, a graph of amplitude and phase noise versus gate voltage at 1.2V supply is plotted in Figure 3.24. This shows an increase in output amplitude at higher gate voltage, and an improved phase noise of -95.8dBc/Hz at  $V_{gate} = 0.75V$ .

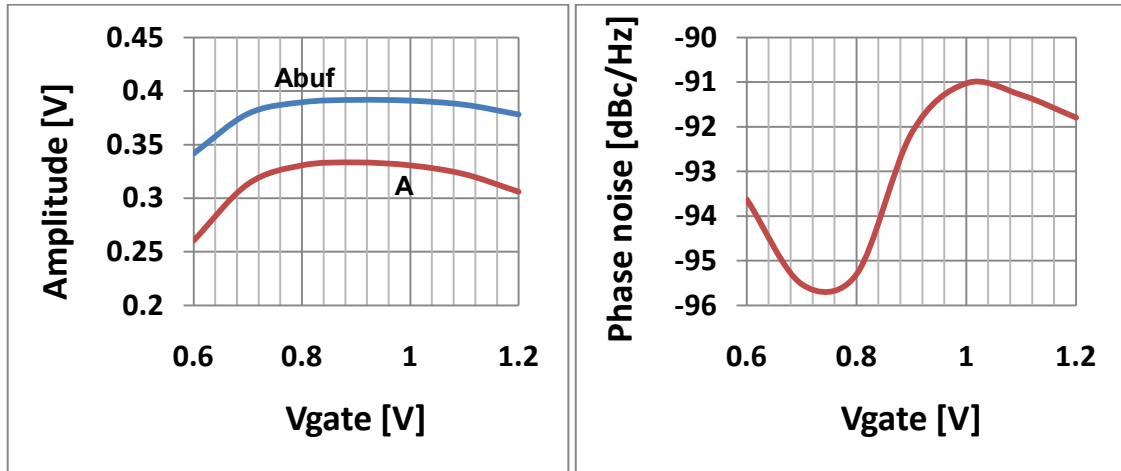


Figure 3.24: Amplitude and phase noise variations with external gate bias at 1.2V supply and maximum oscillation frequency.

### 3.3.5.6 Performance at a reduced load size

Up till now, the LO buffer is assumed to have a 40um load transistor. This is to simulate a large locking range divide-by-two stage, as will be shown in the divider section. Smaller load transistor size helps getting a better output voltage swing. The LO buffer is usually loaded by two mixer blocks in a receiver front-end, each with around 12um input transistor size, as will be shown in the mixer section. Figure 3.25 shows the increase in the buffer output swing at a load transistor of 24um instead of 40um. Maximum output swing is around 0.52V peak.

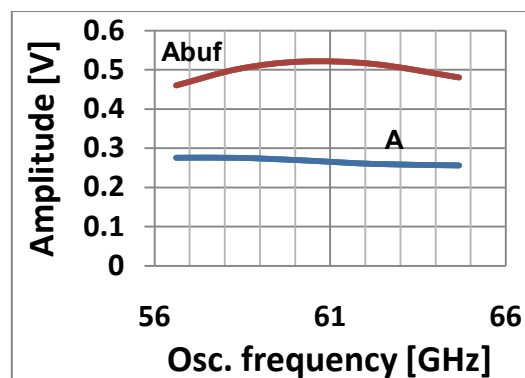


Figure 3.25: P-QVCO and LO buffer amplitudes vs. oscillation frequency at a reduced load transistor width of 24um.

### 3.3.6 Simulation results of BS-QVCO

In the following section, the schematic simulation results of the BS-QVCO and transformer-coupled LO buffer combination are plotted. The BS-QVCO is designed using the same parameter values of the P-QVCO except for the coupling transistor size and the bias current. They are optimized for the best performance of the oscillator.

#### 3.3.6.1 Performance at a load transistor of 40um

Figure 3.26 shows the BS-QVCO performance. Peak amplitude of around 0.39V and a tuning range of 8GHz were achieved. At the highest oscillation frequency, phase noise is -95.1dBc/Hz. This is due to the buffer tail transistor, as explained before.

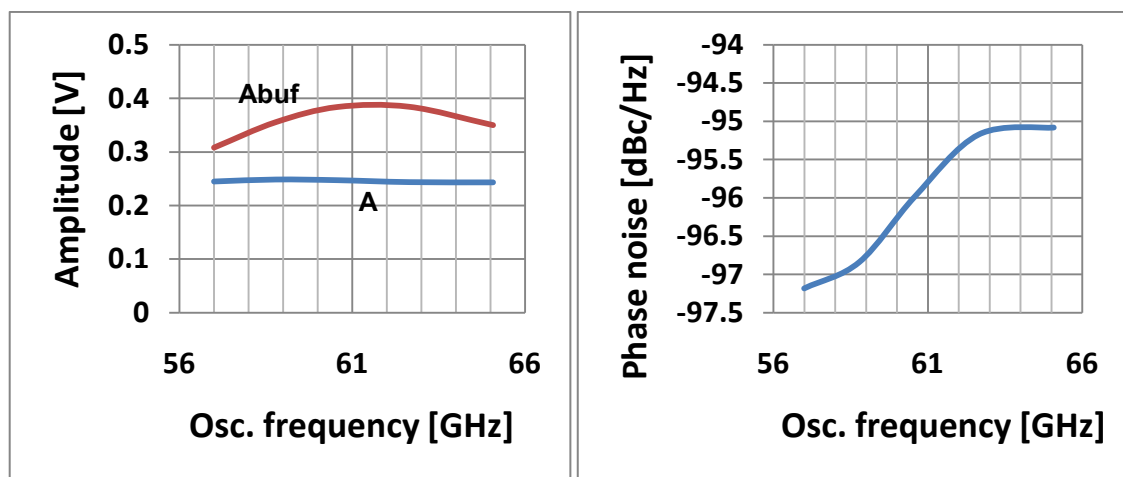


Figure 3.26: BS-QVCO and LO buffer amplitudes and phase noise over the whole tuning range.

#### 3.3.6.2 Performance at a load transistor of 24um

At a reduced load transistor size, the BS-QVCO can reach peak amplitude of 0.49V. This is expected because of the 100mV improvement in the P-QVCO output amplitude when a 24um load transistor is used instead of a 40um one (Figure 3.25 and Figure 3.18).

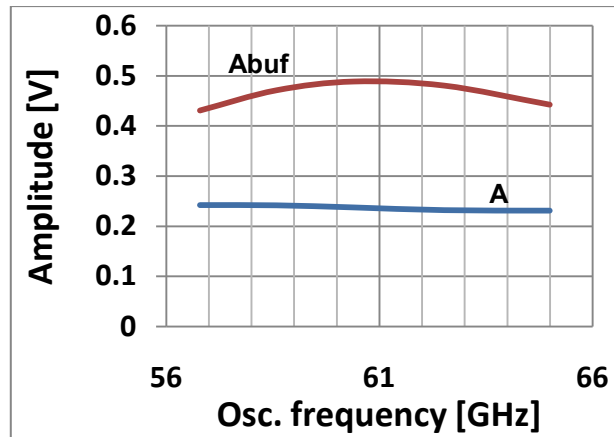


Figure 3.27: BS-QVCO and LO buffer amplitudes vs. oscillation frequency at a reduced load transistor width of 24 $\mu$ m.

### 3.3.7 Performance summary

A comparison between the required and achieved specs in both the P-QVCO and BS-QVCO is shown in Table 3.3. All the requirements are met from simulations of the circuits at the schematic level. The output swing requirement is met at a reduced load size of 24 $\mu$ m. The BS-QVCO shows very close results to the externally gate-biased P-QVCO. The advantage in the series approach of the BS-QVCO is the current reuse. Power consumption is 10mW in the series-QVCO compared to the 26.6mW in the parallel one. The P-QVCO was selected due to the variable coupling, which ensures oscillation startup. Thus, the P-QVCO configuration will be used in the following top-level circuits.

Table 3.3: QVCO and LO buffer target specs & achieved results.

Parameter	Required	Achived (P-QVCO)	Achieved (BS-QVCO)
Max. phase noise	-90dBc/Hz	-98.9 to -94.8dBc/Hz	-97.2 to -95.1dBc/Hz
Center frequency	60.5GHz	60.8GHz	60.5GHz
Min. tuning range	8GHz	8GHz	8GHz
Max. power consumption	30mW	26.6mW	10mW
Min. voltage swing	1V-pp	0.84V-pp (Mload=40 $\mu$ m) 1.4V-pp (Mload=24 $\mu$ m)	0.78V-pp (Mload=40 $\mu$ m) 0.98V-pp (Mload=24 $\mu$ m)

## 3.4 Divider chain

The aim of this section is to design a divider chain with a divide ratio of 16, with maximum input locking range, and minimum power consumption. This ratio will divide the 60GHz input to low-GHz frequencies (3.75GHz), which is easily measured by an oscilloscope. Also large divider ratios can be reused afterwards in a phase-locked loop (PLL) design, which requires a divider block in its feedback path.

A combination of analog and digital dividers was used to provide a reasonable area and power consumption with good characteristics. A chain of four divider blocks, each with a divide-by-two, is chosen to divide the 60GHz signal to low-GHz frequencies. Multiple divide-by-two blocks are easier to implement and less complex compared to other higher order dividers. Static dividers don't use inductors, and are thus smaller in size. However, the maximum frequency of operation in static dividers is proportional to power consumption. So, for high frequencies (down to 30GHz input), analog dividers are used. The first two blocks are then analog dividers, and the last two are digital ones. Only one inductor per analog divider is used to have a compact design.

Special care should be taken to provide enough margin in the locking range of each divider to overcome process variations and keep the input and output frequency ranges matched within all the divider blocks.

### 3.4.1 Circuit schematic

The first two stages of the divider chain are injection-locked frequency dividers (ILFDs), each with two injecting transistors connected across the tank. The dual-mixing direct ILFD is explained in section 2.3.1, and its schematic is shown in Figure 2.26. The second two stages use a CML static divider, with its schematic shown in Figure 2.28. The complete divider block diagram is shown in Figure 3.28, and the 50Ω output buffers are shown in Figure 3.29.

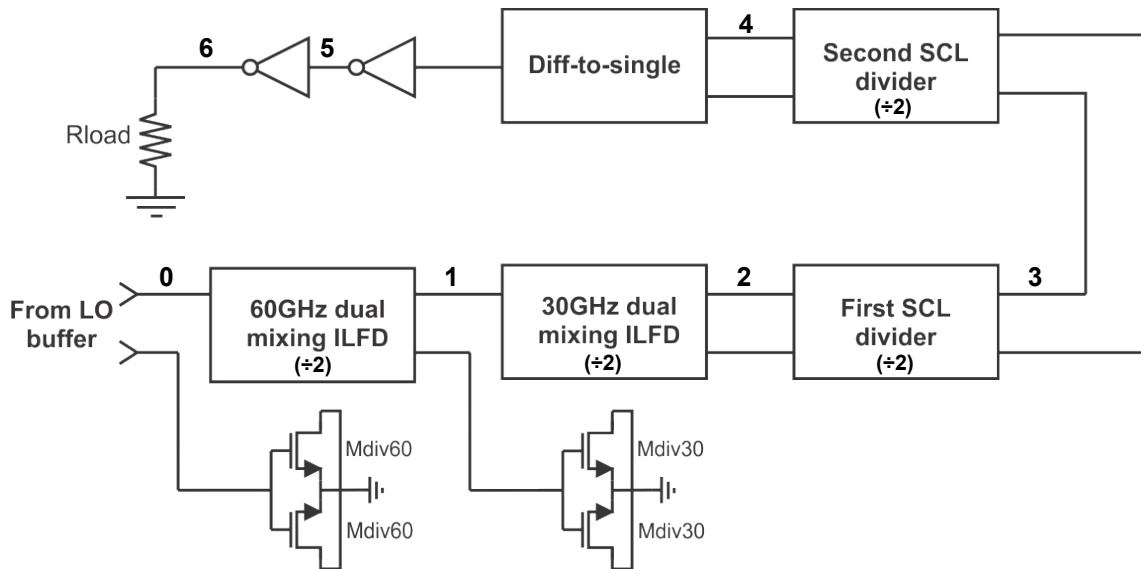


Figure 3.28: Divider chain block diagram.

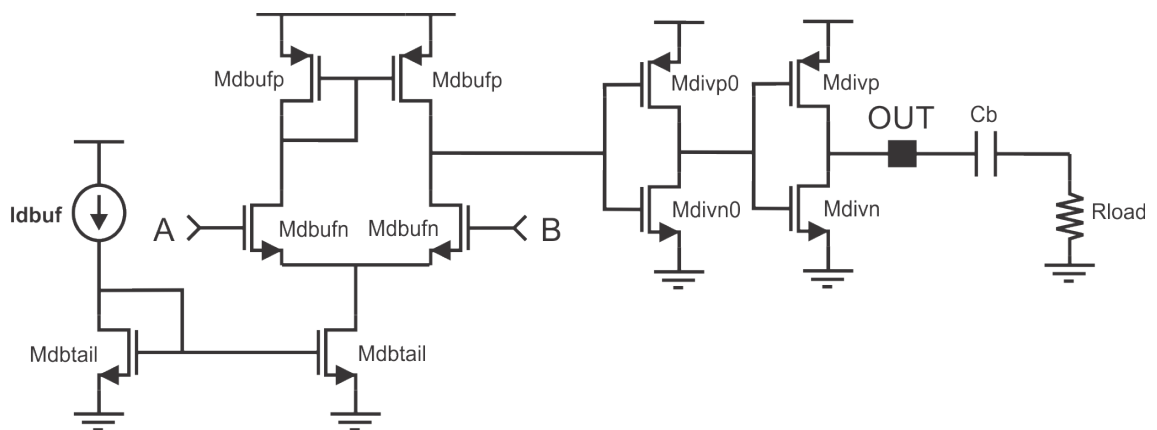


Figure 3.29: Differential to single-ended stage with output buffers.

### 3.4.2 ILFD locking range

Equation 2.17 is an expression for the locking range of direct ILFDs, derived as a result of the analytical model developed in [49]. The equation shows that the locking range doesn't depend on the tank quality factor ( $Q_{tk}$ ).  $Q_{tk}$  can only affect the locking range indirectly through the output amplitude. For example, lower  $Q_{tk}$  results in a lower output amplitude, which leads to a higher equivalent injecting transistor output conductance ( $g_{q,max}$ ) and higher locking range. However, a very high (e.g., 1000)  $Q_{tk}$  can only pass a narrow frequency range. A divider using this load cannot have the same locking range as another one using a low (e.g., 10)  $Q_{tk}$  with wide bandwidth. In this section, we're

going to show that the locking range is independent of  $Q_{tk}$  only to a maximum value of the tank quality factor ( $Q_{tk,opt}$ ). The locking range after this  $Q_{tk,opt}$  is going to decrease with increasing  $Q_{tk}$ .

To understand the effect of the  $Q_{tk}$  on the locking range at the same input overdrive voltage and output voltage swing (same  $g_{q,max}$ ), simulations were performed on the first stage divider (Figure 2.26). The divider is loaded only by the input stage of the following divider and 10fF additional capacitance to model layout parasitics. All the values used are the same as the 60GHz divider values in Table 3.4 except for  $M_{div60}$  which is 26 $\mu$ m. This is just to account for the lower load capacitance due to the usage of only the input stage of the 30GHz divider.

With a fixed inductance value and transistor sizes, the inductor quality factor ( $Q$ ) is varied between 5 and 5000 ( $Q$  represents  $Q_{tk}$  with a fixed capacitance quality factor). The tail current is adjusted at each run to have the same output voltage swing at 60GHz. Figure 3.30 shows how the locking range changes with different  $Q$  values. The tank quality factor is the parallel combination of the inductor and capacitor quality factors. So, at very high values of the inductor  $Q$ ,  $Q_{tk}$  is dominated by the capacitor quality factor. This explains the 14GHz locking range at an inductor  $Q$  of 5000.

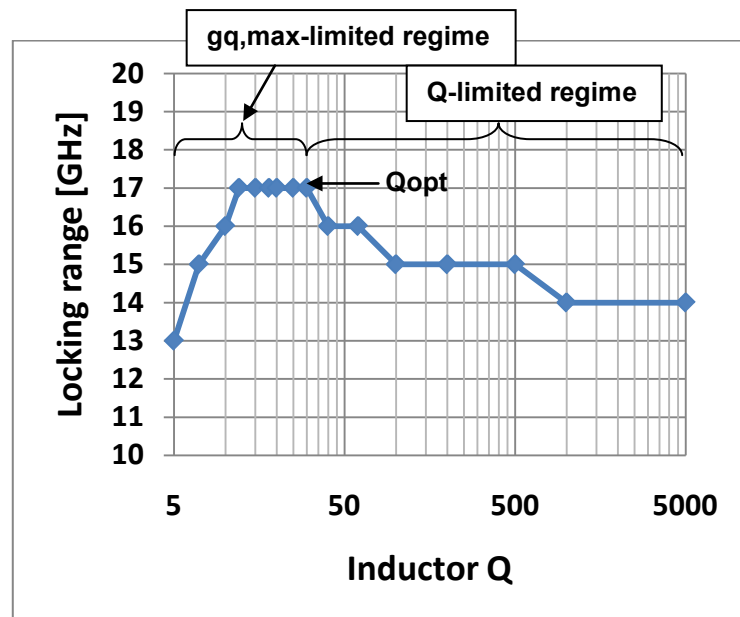


Figure 3.30: Locking range behavior with inductor quality factor.

Figure 3.30 shows that Equation 2.17 is only valid until a maximum inductor quality factor ( $Q_{\text{opt}} = 30$ ), after which the locking range starts decreasing. The range that is independent of  $Q$ , which is below a  $Q$  of 30, is limited by  $g_{q,\text{max}}$  and the output capacitance (it follows Equation 2.17). This is described in Figure 3.30 as the  $g_{q,\text{max}}$ -limited regime. At very low  $Q$  values, a drop in the locking range is noticed. This is due to the higher effective output capacitance, which causes a shift in the divider free-running frequency and a drop in the locking range. In the  $Q$ -limited regime, as  $Q$  gets higher, the frequency components at the edge of the locking range start decreasing in amplitude due to the reduced bandwidth. When those frequency components are filtered out by the low circuit bandwidth, the locking range is reduced. Higher bias current can help at this moment to increase the amplitude of the frequency components at the edge of the locking range. This leads the locking range to increase again to its value before reducing the inductor  $Q$ . Thus, reducing the inductor  $Q$  gives the same locking range with higher bias current. Figure 3.31 shows a divider expected output spectrum with different inductor  $Q$  values assuming equal output amplitudes. The optimum  $Q$  is indicated according to above understanding. The optimum tank quality factor is the highest quality factor before the locking range starts decreasing due to the limited bandwidth.

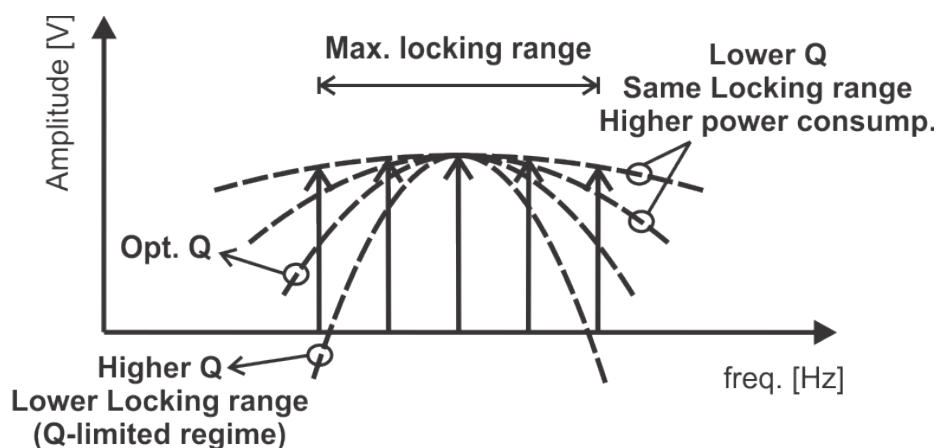


Figure 3.31: Divider output spectrum with quality factor curves assuming equal output amplitude.

### 3.4.3 Design guidelines

General guidelines for the design of each of the divider stages are discussed in this section.

### 3.4.3.1 First analog divider stage

The first divider stage of Figure 3.28 is a dual mixing direct ILFD (Figure 2.26). The inductor value ( $L_{div60}$ ) should be maximized as suggested by Equation 2.17. The inductor quality factor ( $Q_{div60}$ ) should be maximized as suggested by Figure 3.30. The divider can be biased with lower current at higher  $Q_{div60}$  without reducing the locking range (as long as  $Q_{div60}$  is lower than  $Q_{opt}$ ). The maximum inductor value is limited by the self-resonance frequency, and the maximum quality factor is limited by the technology. The cross-coupled pair ( $M_{div60}$ ) and the dual-injecting transistors ( $M_{inj60}$ ) should provide, together with the inductor value, a free-running frequency of 30GHz. The current source transistors ( $M_{tail60}$ ) should be increased until the drain-source voltage of the diode-connected transistor is close enough to that of the tail transistor and the current is copied with the lowest loss. For this, the length of  $M_{tail60}$  can be increased two or three times of its minimum value (80nm) to reduce the short channel effect. The tail current ( $I_{div60}$ ) should be increased until the locking range does not increase anymore with current ( $g_{q,max}$ -limited region), and the output voltage swing is high enough to drive the following stage. Finally, the output conductance of the input injecting transistors should be maximized by using different combinations of  $M_{inj60}$  and  $M_{div60}$  (keeping the same free-running frequency) to get the maximum locking range.

### 3.4.3.2 Second analog divider stage

The second divider stage uses the same topology as the first one. Thus, only steps to migrate design parameters from the 60GHz-input divider stage to the 30GHz divider are going to be discussed. The free-running frequency is divided by 2 (15GHz). This means that the LC product should be multiplied by 4.

$$L_{30}C_{30} = 4L_{60}C_{60} \quad 3.6$$

where the subscript indicates the block input frequency inGHz. The locking range of the second divider is only required to be one-half that of the 60GHz divider.

$$\Delta\omega_{60} = \frac{2g_{q,max,60}}{C_{60}}$$

$$\Delta\omega_{30} = \frac{\Delta\omega_{60}}{2} = \frac{g_{q,max,60}}{C_{60}} = \frac{2g_{q,max,30}}{C_{30}} \quad 3.7$$

If the input amplitude of the second divider is one-half that of the 60GHz divider, then  $g_{q,max,30}$  equals to  $g_{q,max,60}/2$ . From Equation 3.7, it follows that  $C_{30}$  is the same as  $C_{60}$ . By substituting in Equation 3.6, the 30GHz stage inductor should be 4 times larger than the 60GHz stage one.

### 3.4.3.3 Static dividers

Static dividers are used in the third and fourth divider blocks. The maximum frequency of operation determines the locking range. This is mainly affected by the total capacitance at the divider output terminals and power consumption. The output capacitance should be reduced and more power consumption should be used for higher frequency operation. Firstly, a bias current should be assumed. The tail transistors should be increased until the current is copied with the lowest loss. As explained in section 2.3.2, the cross-coupled devices can be 1.5x smaller in gate width than buffer devices. Both buffer and cross-coupled transistors should be set to their minimum gate width value (keeping acceptable matching properties [17]). This is to minimize the output capacitance. The load resistance ( $R_D$ ) should be chosen to maximize the output voltage swing at the specified bias current. Finally, the bias current can be changed, with all the circuit parameters re-optimized, to control the divider speed. The maximum operating frequency is designed to be slightly higher than the maximum input frequency to save in the power consumption.

### 3.4.4 Design values

Final design values according to the discussed guidelines are shown in Table 3.4. The finger width used is 1 $\mu$ m. M defines the number of fingers and L is the channel length.

**Table 3.4: Design values for the divider chain circuit.**

60GHz dual mixing direct ILFD			30GHz dual mixing direct ILFD		
Parameter		Value	Parameter		Value
Cross-coupled pair (Mdiv60)	M	24	Cross-coupled pair (Mdiv30)	M	48
	L	80nm		L	80nm
Input injecting transistors (Minj60)	M	20	Input injecting transistors (Minj30)	M	20
	L	80nm		L	80nm
Current mirror (Mtail60)	M	96	Current mirror (Mtail30)	M	96
	L	160nm		L	160nm
Differential inductor	Ldiv60	330pH	Differential inductor	Ldiv30	1.2nH

(Ldiv60)	Q	11	(Ldiv30)	Q	15
Bias current (Idiv60)	I	4mA	Bias current (Idiv30)	I	2mA
<b>First SCL divider</b>			<b>Second SCL divider</b>		
<b>Parameter</b>	<b>Value</b>		<b>Parameter</b>	<b>Value</b>	
Buffer transistor (Mb1)	M	12	Buffer transistor (Mb2)	M	12
	L	80nm		L	80nm
Cross-coupled transistor (Mcc1)	M	8	Cross-coupled transistor (Mcc2)	M	8
	L	80nm		L	80nm
Input transistor (Mclk1)	M	12	Input transistor (Mclk2)	M	12
	L	80nm		L	80nm
Current mirror (Mtail1)	M	64	Current mirror (Mtail2)	M	64
	L	160nm		L	160nm
Load resistor (Rlatch1)	R	700Ω	Load resistor (Rlatch2)	R	1kΩ
Bias current (Ilatch1)	I	2mA	Bias current (Ilatch2)	I	1mA

### 3.4.5 Simulation results

In the following section, the schematic simulation results of the divider chain are plotted. Each divider block is loaded by the rest of the divider chain while being tested. Ideal inductors with estimated quality factors of 11 and 15 were used in the first and second analog dividers, respectively. Additional capacitances of 10fF each were added at the analog divider outputs to simulate layout parasitics. Transient simulations and FFT were used to collect the data.

#### 3.4.5.1 60GHz divider

Figure 3.32 shows the locking range at different input levels for the first divide-by-two stage. At rail-to-rail input signal (500mV-peak = 4dBm), 15GHz locking range can be achieved around 59.5GHz. Note that locking range is reduced with lower input amplitudes. This emphasizes the importance of higher output voltage swings from the LO buffer. The minimum affordable locking range in our system is 8GHz + process margin. This can be around 9GHz, which can be achieved at around 0dBm input signal (0.3V-peak). Output power at rail-to-rail input signal is shown in Figure 3.33. This is going to feed the following 30GHz divider stage.

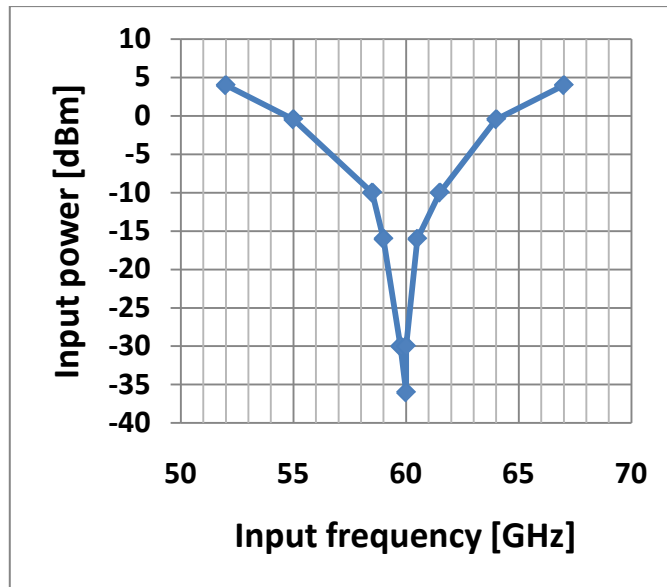


Figure 3.32: 60GHz divider input sensitivity curve.

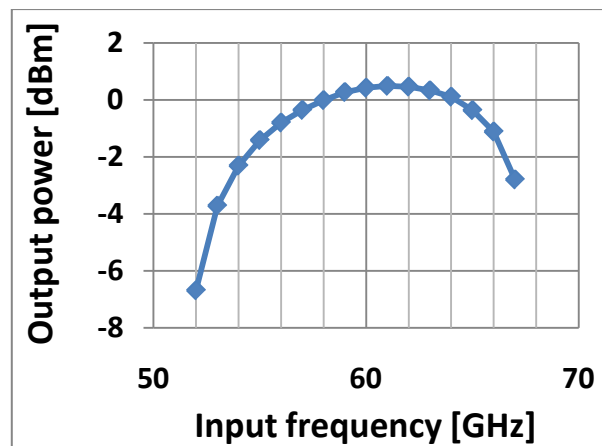


Figure 3.33: 60GHz divider output power at 4dBm input signal.

### 3.4.5.2 30GHz divider

The locking range of the second divider is shown in Figure 3.34. A 22GHz locking range can be achieved at rail-to-rail input (0.5V-peak). Only 4GHz input locking range is required at 30GHz to match the 8GHz locking range of the preceding 60GHz divider. This can be achieved with around -15dBm input signal. This gives a good margin for the 60GHz divider output signal that can be reduced due to lower input signals or process variations. Output power at rail-to-rail input signal is shown in Figure 3.35. This is slightly reduced at lower input levels.

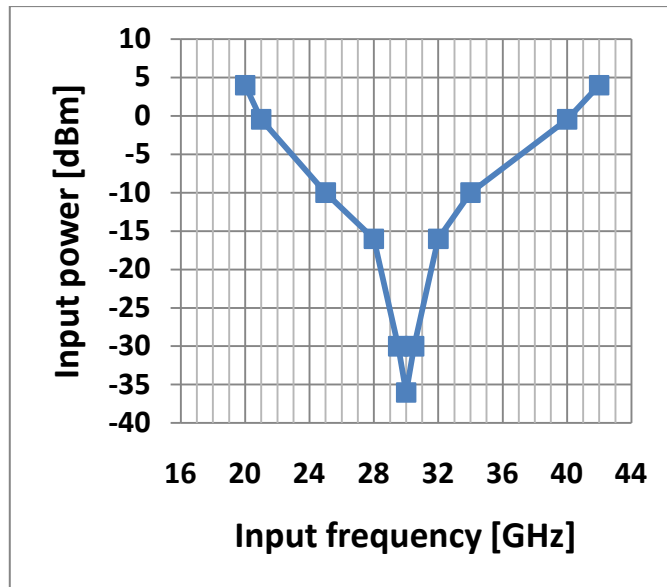


Figure 3.34: 30GHz divider input sensitivity curve.

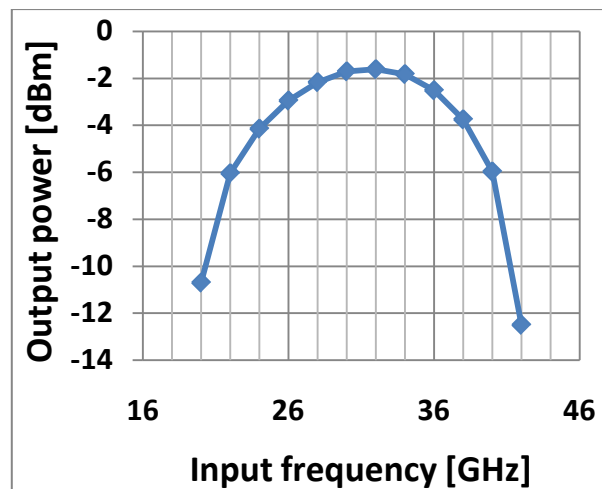


Figure 3.35: 30GHz divider output power at 4dBm input signal.

### 3.4.5.3 First CML divider

Input sensitivity curve and output power level of the first static divider are shown in Figure 3.36 and Figure 3.37, respectively. A maximum input frequency of 25GHz can be achieved by the SCL divider at rail-to-rail input signal. This divider operates at 15GHz, and only needs 2GHz input locking range. A minimum signal of -15dBm can be afforded because of the lower edge of the locking range.

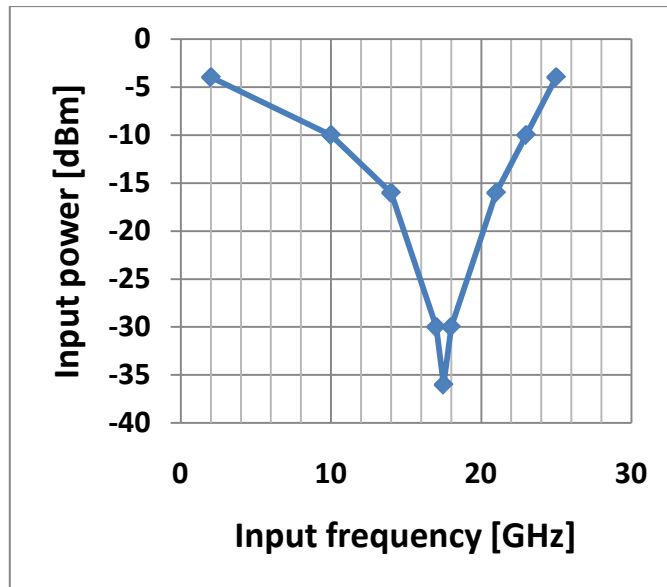


Figure 3.36: First static divider input sensitivity curve.

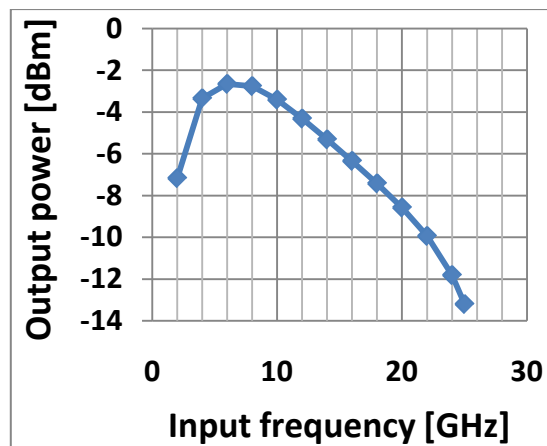


Figure 3.37: First static divider output power at 4dBm input signal.

#### 3.4.5.4 Second CML divider

As shown in Figure 3.38, maximum input frequency of the second static divider is slightly lower than that of the first one. The difference between both dividers is the lower power consumption in the second one (and the adjusted load resistance accordingly). The divider operates at 7.5GHz and only needs 1GHz input locking range. Minimum affordable input signal power is around -14dBm because of the lower edge of the locking range. Output power at rail-to-rail input signal is shown in Figure 3.39. This is going to feed the following differential to single-ended circuit that is loaded by the 50Ω off-chip resistance through the 2 inverting buffers.

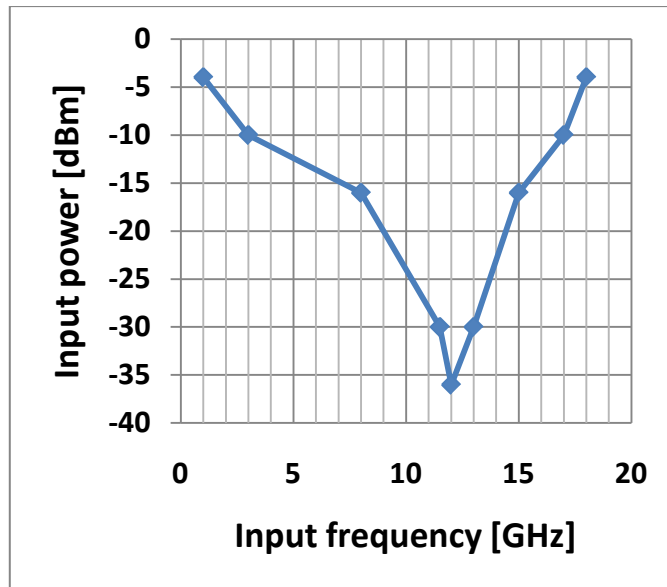


Figure 3.38: Second static divider input sensitivity curve.

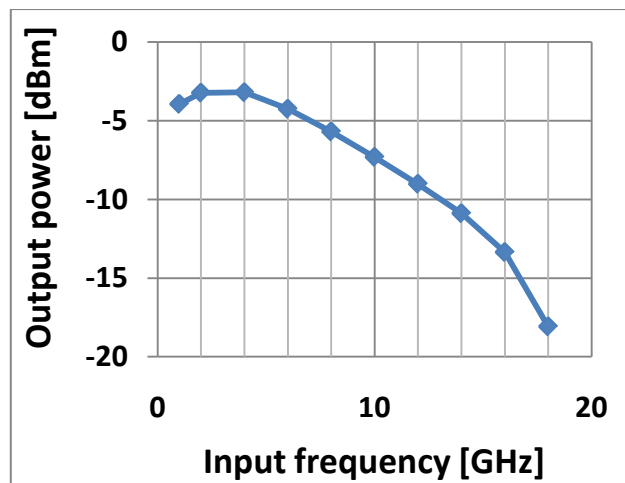


Figure 3.39: Second static divider output power at 4dBm input signal.

### 3.4.5.5 The complete divider chain

With a rail-to-rail input signal to the divider chain, Figure 3.40 shows signal power levels at different nodes. Circuit nodes at which signal levels are plotted are defined by numbers from 0 to 6. These are shown in Figure 3.28. Signal frequencies are indicated in the plot. Static dividers provide lower output amplitudes (nodes 3 and 4) as compared to the dynamic ones (nodes 1 and 2) at the required frequency range. This is compensated by the output buffers that provide higher output swing for measurements.

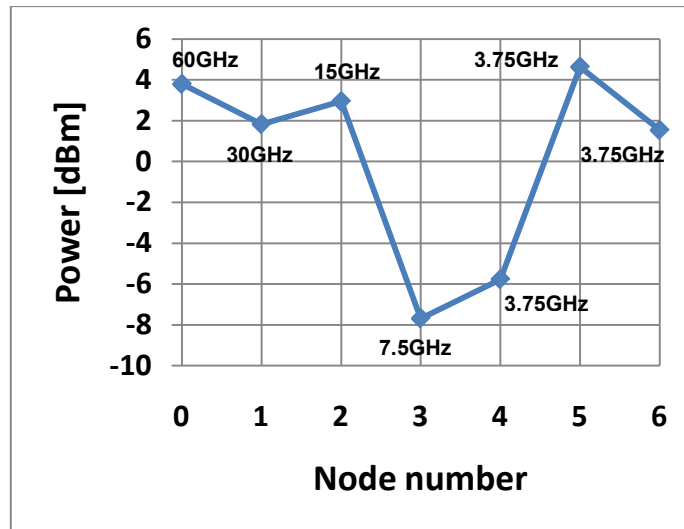


Figure 3.40: Divider chain signal levels at each block.

### 3.4.6 Performance summary

A summary of the performance of each divider block is shown in Table 3.5. The center frequency listed in the table is the frequency at which the divider locks with minimum input signal amplitude. The four divider blocks consume 9mW. The rest of the chain, including the differential to single-ended block, and the two inverters consume DC power consumption of 4.3mW.

In section 3.4.3.2, the locking range of the 30GHz divider was expected to be halved at one-half of the input signal (same locking range at the same input signal level). This is not the case because  $g_{q,max}$  was assumed to be the same. The 30GHz divider output has a lower bias voltage (due to the larger inductor value, and thus, higher DC resistance) and amplitude compared to the 60GHz divider. This increases  $g_{q,max}$ , which results in a higher value for the locking range.

Table 3.5: Performance summary of each divider block.

Divider block	Locking range at rail-to-rail input	Center frequency	Power consumption
60GHz divider	52GHz - 67GHz	60GHz	4mW
30GHz divider	20GHz - 42GHz	30GHz	2mW
First SCL divider	2GHz - 25GHz	17.5GHz	2mW
Second SCL divider	1GHz - 18GHz	12GHz	1mW

### 3.5 LNA and mixer

The aim of this section is to migrate an already-existing LNA and mixer combination [62] from a 45nm process to the 90nm one. No architectural changes were performed on the circuit. Circuit elements including actives and passives were redesigned in the 90nm technology. Target specifications are a maximum conversion gain of 26dB at 60GHz input, 6dB noise figure, +3.5dBm output -1dB compression point and -12dBm third-order intercept point (IIP3) in the high gain (HG) mode. These are the measured values for the 45nm design.

#### 3.5.1 Circuit schematic

The circuit schematic is shown, reprinted from [62], in Figure 3.41. The circuit includes a two-stage, single-ended, inductively-degenerated, common-source differential amplifier. The second stage is loaded by a transformer, which drives a double-balanced mixer for down-conversion. The actual circuit includes two similar double-balanced mixers for I and Q signals from the LO input. In our circuit, the mixer performance was checked using a resistive load instead of the diode-connected PMOS load in Figure 3.41. This is because no information was available about the mixer load.

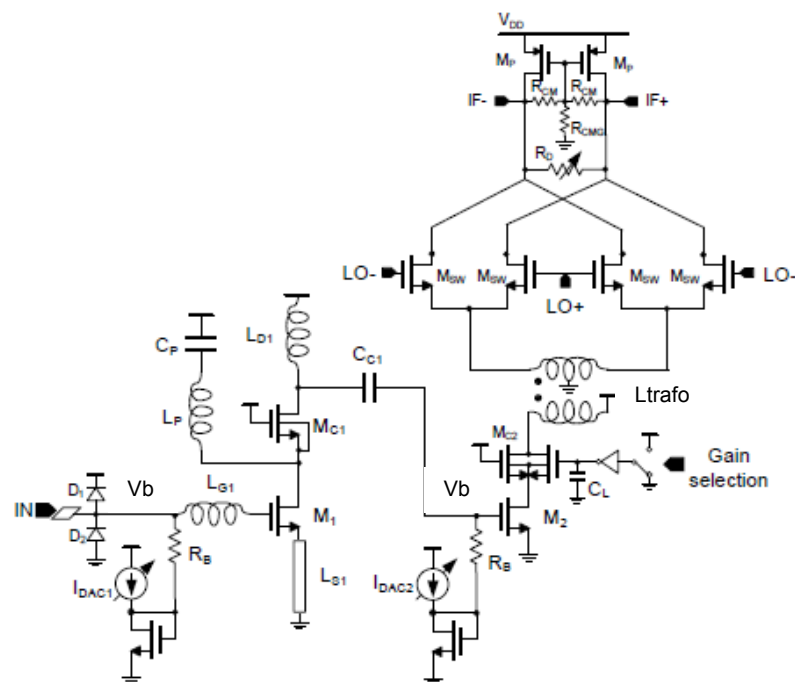


Figure 3.41: Circuit schematic of the LNA+mixer combination [62].

### 3.5.2 Design guidelines

As explained in section 2.4.2, gain, noise figure (NF), and input impedance matching for the LNA can be achieved through adjusting the size of transistor M1, together with inductor values  $L_{S1}$  and  $L_{G1}$ . Inductor  $L_P$  should be sized to absorb the parasitic capacitance at the cascode node. Capacitor  $C_P$  is just to prevent the cascode node from being biased, through inductor  $L_P$ , at the supply voltage. Inductor  $L_{D1}$  and the second stage transformer should provide maximum gain at the required 60GHz frequency. The transformer should also absorb the parasitic capacitance at the source node of the mixer switches  $M_{SW}$ . This, together with the LO buffer transformer, allow for larger switch transistors without losing the bandwidth.

### 3.5.3 Design values

Design values for the two-stage LNA and mixer, excluding the bandgap reference, current DAC and digital circuitry are listed in Table 3.6. Minimum length (80nm) is used in all circuit transistors. The supply voltage is 1V. M defines the number of fingers and W is the channel width.

**Table 3.6: Design values for the LNA and mixer.**

Transistor sizes		
Parameter		Value
Common-source transistor (M1, M2)	W	1.5um
	M	64
Cascode transistor (Mc1)	W	1.5um
	M	64
Cascode transistor (Mc2)	W	1.5um
	M	32
Switch transistor (Msw)	W	1.5um
	M	8
Passive elements' values		
Source inductor	$L_{S1}$	150pH
Gate inductor	$L_{G1}$	10pH
Drain inductor	$L_{D1}$	40pH
Cascode inductor	$L_P$	80pH

Cascode capacitor	$C_P$	370fF
Coupling capacitor	$C_{C1}$	370fF
Biasing resistor	$R_B$	6.5k $\Omega$
Coupling transformer (primary = sec.)	Ltrafo	90pH
<b>Controlling parameters</b>		
CS transistor bias voltage @ max. current	Vb	660mV
LO bias voltage	$V_{LO,DC}$	200mV

### 3.5.4 Simulation results

Schematic simulation results of the LNA and mixer combination are going to be plotted in the following sub-sections. The circuit is simulated with ideal inductors ( $L_{S1}$ ,  $L_{G1}$ ,  $L_{D1}$  and  $L_P$ ) with an estimated quality factor of 12. The transformer RLCG model is used, as shown in Figure 3.10. An intermediate frequency of 1GHz is used in the simulation. Estimates of the parasitic capacitances for the layout were kept from the original design.

#### 3.5.4.1 Conversion gain

Conversion gain as a function of LO input power is shown in Figure 3.42 for a load resistance ( $R_L$ ) of 1k $\Omega$ . Different LO bias voltages ( $P_{LO,DC}$ ) were used to choose the operating voltage. This can be controlled at the LO buffer transformer center tap (Figure 3.12). A mixer switch transistor should be biased close to its threshold voltage (around 0.25V) for symmetric switching (an ideally square wave output current). That's why the gain is decreased at LO bias voltages of 0.1V and 0.4V. The conversion gain is increased with the input LO amplitude until the mixer switch transistors go into the triode region. At a  $P_{LO,DC}$  of 0.2V, the mixer switch transistors go into the triode region at 7dBm (compared to 3dBm at  $P_{LO,DC}$  of 0.3V) LO input power ( $P_{LO,dBm}$ ), and the conversion gain is still large enough at smaller LO input signals. So, a LO bias voltage of 200mV was chosen for our operation.

Conversion gain vs. load resistance at different LO input power levels is shown in Figure 3.43. Conversion gain is proportional to the load resistance. However, higher resistance values causes larger voltage drops that reduce headroom as the drain voltage of the mixer transistor is biased at a lower voltage. With larger input swing at the LO input, the mixer transistor can easily go into the triode regime, causing the conversion gain to drop with LO input amplitude. That's why the gain is dropped at 3.5 k $\Omega$  for

$P_{LO,dBm}$  of 4dBm while it keeps increasing for lower LO input power values (expected to drop at higher load resistance values).

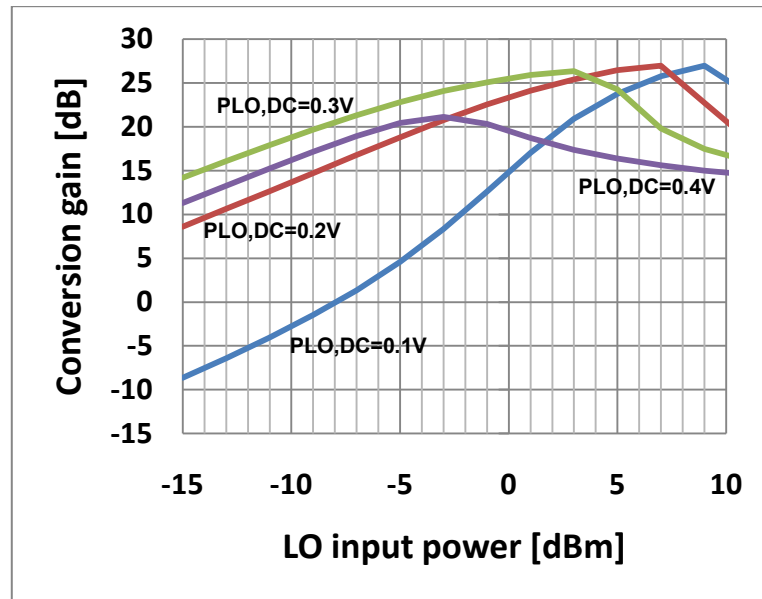


Figure 3.42: Conversion gain vs. LO input power for  $R_L=1k\Omega$ .

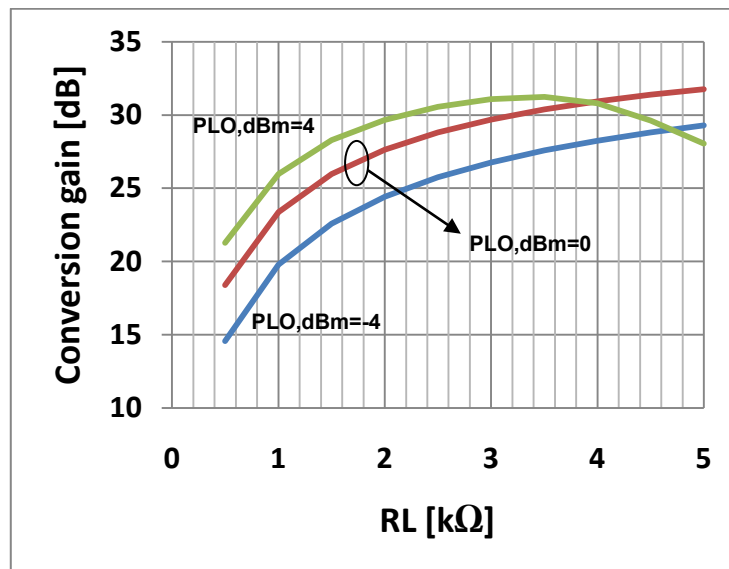


Figure 3.43: Conversion gain vs. mixer load resistance for different LO input power values.

Conversion gain at 5kΩ load resistance is shown in Figure 3.44. Gain starts decreasing at a lower value for LO input power compared to case with 1kΩ (Figure 3.42). Thus, operation with a 5kΩ resistive load is only advised at low input LO power values (below 3dBm).

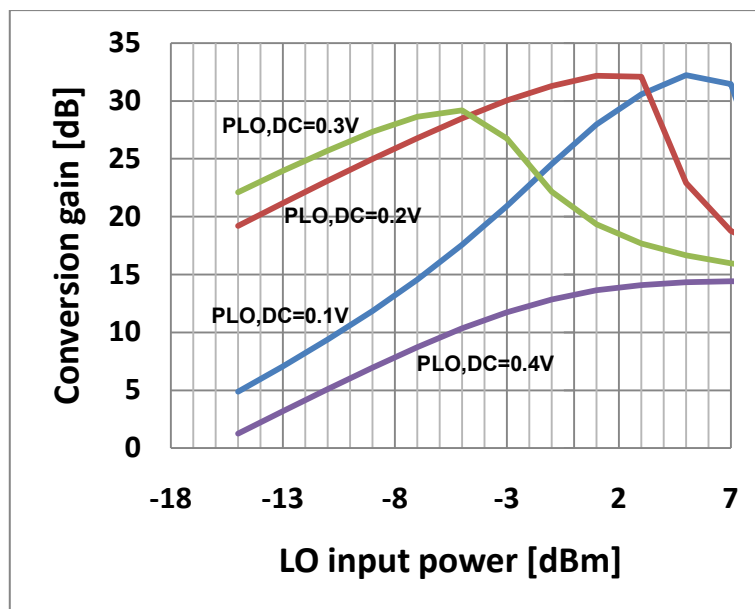


Figure 3.44: Conversion gain vs. LO input power for  $R_L=5k\Omega$ .

Conversion gain across the input frequency band is shown in Figure 3.45. Maximum conversion gain of 26.3dB at 60GHz is achieved at  $1k\Omega$  load resistance, 200mV LO bias voltage, and 4dBm LO input power. The circuit doesn't provide a constant gain over the 7GHz input bandwidth. This explains the need for wide-band LNA design if channel bonding is used in the system and the entire bandwidth is used.

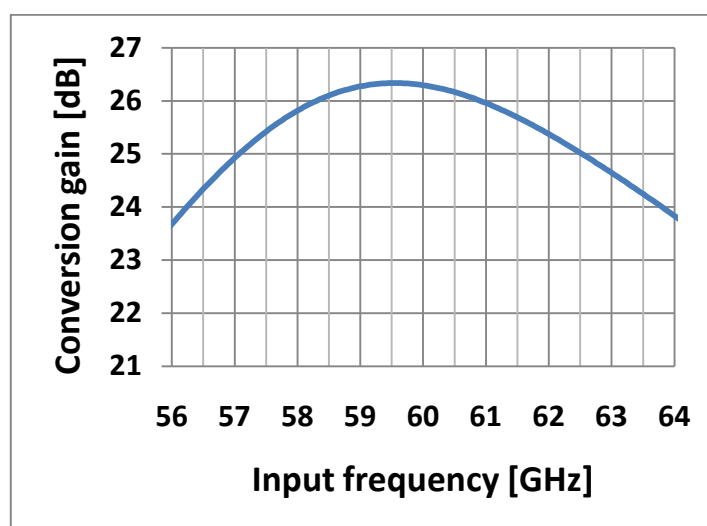


Figure 3.45: Conversion gain vs. RF input frequency for  $R_L=1k\Omega$  and  $P_{LO,dBm}=4dBm$ .

### 3.5.4.2 Noise figure and S11

Double-side band noise figure is going to be used for the following NF results. Noise figure and input return loss are shown in Figure 3.46a and Figure 3.46b, respectively. The noise figure is 5dB and S11 is lower than -10dB over the whole 7GHz input frequency band.

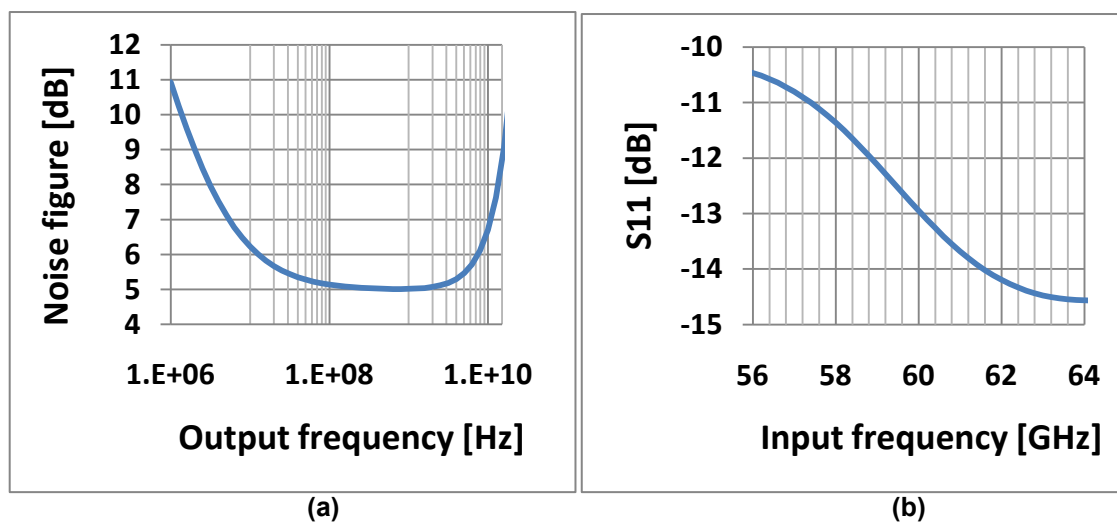


Figure 3.46: (a) Noise figure vs. IF output frequency, and (b) S11 vs. RF input frequency.

### 3.5.4.3 Linearity

Output -1dB compression point and third order intercept point are shown in Figure 3.47. The load resistance is set to 1k $\Omega$ , and the LO input power is 4dBm. Output P-1dB from simulation is +5.8dBm and IIP3 is -9.7dBm.

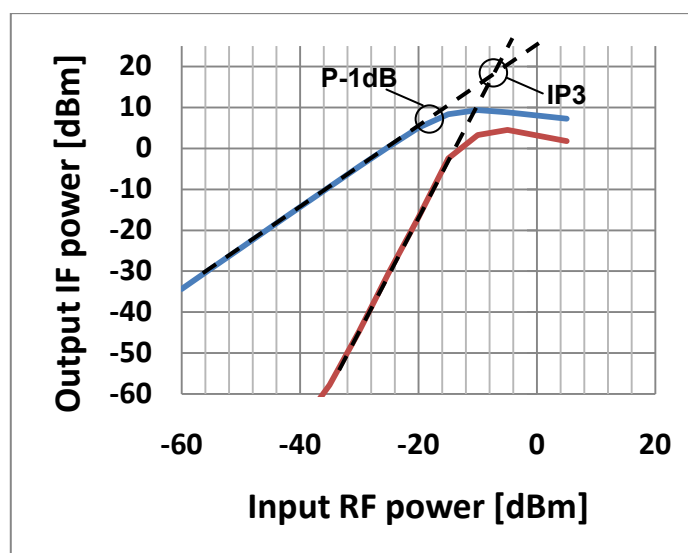


Figure 3.47: -1dB compression point and third order intercept point for RL=1k $\Omega$ .

The circuit consumes 41.6mW from 1V supply. This is because of the increased LNA transistor sizes during migration. The biasing circuit, on the other hand, is kept without changes.

#### 3.5.4.4 Results at reduced power consumption

If we switch off one bit of the current DAC, we can get a reduced bias voltage for the LNA CS transistors ( $V_{GS}=500\text{mV}$ ). This reduces the total power consumption to 21.8mW. The gain could, however, be increased by using a higher load resistance. At a load resistance of  $1.5\text{k}\Omega$ , conversion gain versus LO input power is shown in Figure 3.48. The conversion gain starts to drop at 6dBm input LO power ( $0.63\text{V-peak}$ ). A conversion gain of 26.77dB can be achieved at 4dBm input power ( $0.5\text{V-peak}$ ).  $S_{11}$  is below 12.5dB for the entire frequency range (57-64GHz). NF is 5.88dB at 1GHz IF frequency. Output -1dB compression point is 6.3dBm and IIP3 is -8.6dBm. These results are very close to the high power (HP) mode results with a 50% improvement in the power consumption.

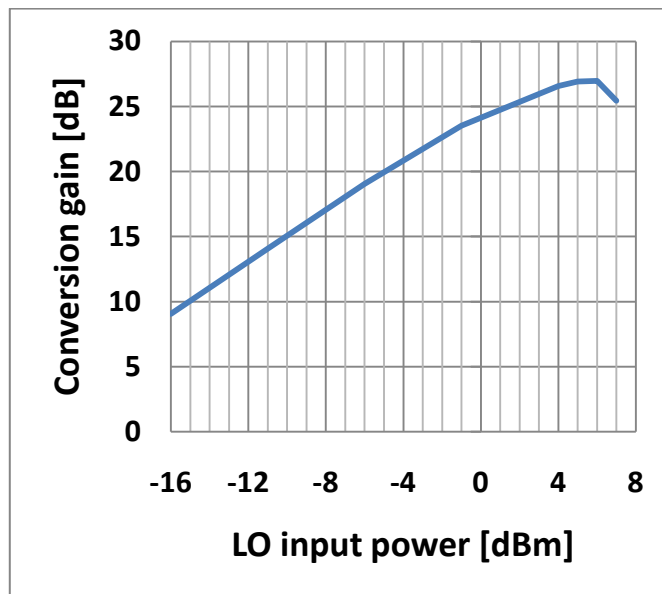


Figure 3.48: Conversion gain vs. LO input power at 21.8mW total power consumption.

At minimum power consumption (LP mode), the LNA CS transistors are biased at a gate-source voltage of 380mV. Total power consumption is then 10.55mW. Conversion gain for a mixer load resistance of  $1.5\text{k}\Omega$  is shown in Figure 3.49 versus LO input power. A conversion gain of 17.7dB can be achieved at 4dBm LO input power ( $0.5\text{V-}$

peak).  $S_{11}$  is below  $-15\text{dB}$  over the  $57\text{-}64\text{GHz}$  input frequency range, and NF is  $10.11\text{dB}$ . Output  $-1\text{dB}$  compression point is  $+5.8\text{dBm}$  and IIP3 is  $-2.4\text{dBm}$ .

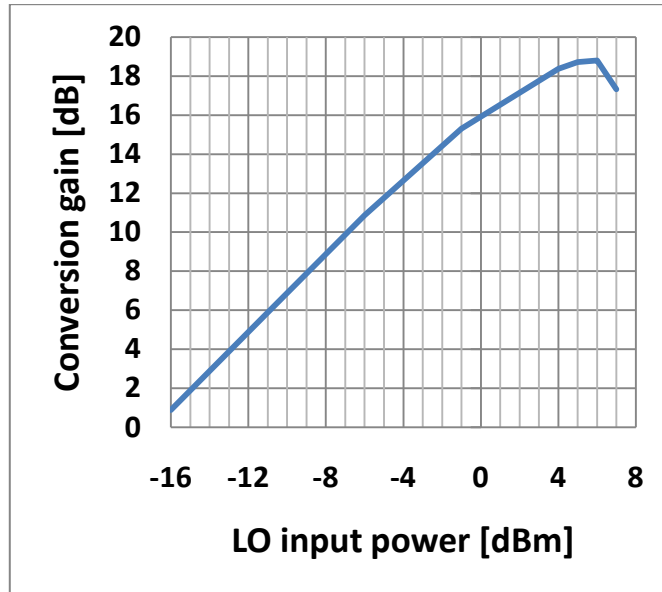


Figure 3.49: Conversion gain vs. LO input power at  $10.55\text{mW}$  total power consumption.

### 3.5.5 Performance summary

A comparison between the required specifications and the design simulations in the reduced power (RP) mode is shown in Table 3.7. The reduced power mode has very close results to the high power mode except for the improved power consumption. Thus, it should be used instead.

Table 3.7: Performance summary of the LNA and mixer combination.

Parameter	Required	Achieved (RP)
Conversion gain (CG)	26dB	26.77dB
Noise figure (NF)	6dB	5.88dB
Output $-1\text{dB}$ compression point	$+3.5\text{dBm}$	$+6.3\text{dBm}$
Input-referred 3 <sup>rd</sup> order intercept point (IIP3)	$-12\text{dBm}$	$-8.6\text{dBm}$
Max. input reflection coefficient ( $S_{11}$ )	$-10\text{dB}$	$-10\text{dB}$
Total power consumption	23mW	21.8mW

# Chapter 4

## Top-Level Design

---

After all the front-end circuit blocks are discussed, the top-level schematic design is going to be presented in this chapter. The circuit performance after putting blocks together is expected to differ from the performance of the blocks separately. This is due to the effect of actual loading of one block by another, as compared to the expected loading while dealing with each section alone.

### 4.1 Complete top-level circuit

In our top-level, we still have another challenge. This is to let the oscillator drive both the mixer and the divider. Two transformer-coupled CS amplifiers provide suitable voltage swings to both the mixer and divider inputs. The top-level circuit now includes the QVCO, LO buffers, divider chain, LNA and mixer. Top-level schematic and simulation results are shown in the following subsections.

#### 4.1.1 Circuit schematic

Figure 4.1 shows the top-level schematic of all of the blocks connected together. The P-QVCO, the divider chain, the LNA and mixer from sections 3.3, 3.4 and 3.5, respectively, are used. Ideal transformers with an estimated quality factor and coupling coefficient of 8 and 0.8, respectively, are used in the simulation.

#### 4.1.2 Design choices

The divider input transistor is 40 $\mu\text{m}$  wide and the mixer input transistor is 12 $\mu\text{m}$  wide. A single CS differential stage was not enough to buffer both loads. So, two buffer stages (Mbuf1 and Mbuf2 in Figure 4.1) are used instead. One choice was to load the first buffer with the second buffer and the second buffer with both the mixer and divider loads. The mixer circuit can operate (with enough gain) at lower input amplitude than the divider. As shown in Figure 3.32, the divider locking range is increased from around 6GHz to 15GHz if the input amplitude is increased from 0.2V to 0.5V-peak.

Meanwhile, Figure 3.48 shows a reduction of around 2dBm in mixer conversion gain for the same change in the input amplitude. Thus, instead of providing the mixer and divider circuit with the same input amplitude, one buffer stage is chosen to buffer the mixer circuit and two for the divider. The buffer configuration is shown in Figure 4.1. This allows more swing to be delivered to the divider input (without an effective degradation in the mixer performance) as compared to the first choice (two buffers loading both mixer and divider circuits). Downsides of the additional buffer are the added chip area and power consumption. However, an approximately  $2 \times 50 \mu\text{m} \times 50 \mu\text{m}$  additional chip area (dominated by the differential inductor size) and  $2 \times 10 \text{mA}$  additional power consumption are not so significant in a system with an estimated chip area of  $0.13 \text{mm}^2$  and power consumption of  $92 \text{mA}$ .

### 4.1.3 Design values

The P-QVCO values are listed in Table 3.2, where parameters related to the P-QVCO don't depend on the load. The divider chain values are listed in Table 3.4. The reduced power LNA is used in the top-level. The LNA and mixer design values are shown in Table 3.6. The bias voltage of the CS node in the LNA is  $500 \text{mV}$ . The load resistance is  $1.5 \text{k}\Omega$ , and the LO input bias voltage ( $V_b$ ) is  $200 \text{mV}$ . These are the same values used in the reduced power version of the LNA and mixer combination. The transformer values are chosen to tune out the parasitic capacitance and maximize the buffer gain at  $60 \text{GHz}$ . The gate width of the buffer transistor is a trade-off between buffer gain and input impedance. Higher buffer gate width causes a shift in the oscillator operating frequencies due to the higher load capacitance. Design values for the two LO buffers are shown in Table 4.1. The transistor finger width ( $W$ ) of all the buffer transistors is  $1 \mu\text{m}$ .  $M$  defines the number of fingers and  $L$  is the channel length.

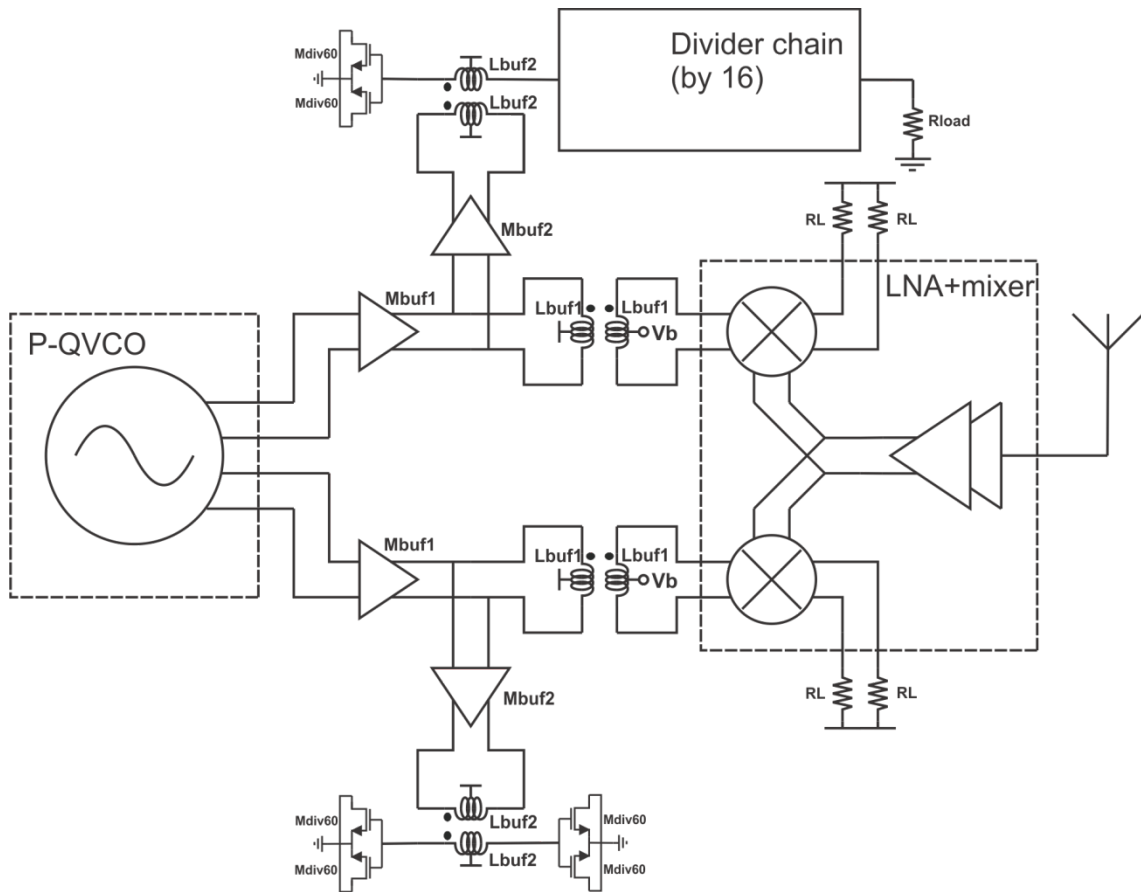


Figure 4.1: Front-end top-level circuit schematic.

Table 4.1: LO buffers design values for the complete top-level circuit.

Transistor sizes		
Parameter		Value
First buffer transistor (Mbuf1)	M	14
	L	80nm
Second buffer transistor (Mbuf2)	M	20
	L	80nm
Current mirror transistors (Mcm,buf)	M	208
	L	300nm
Passive elements' values		
First buffer transformer (primary = sec.)	Lbuf1	200pH
Second buffer transformer (primary = sec.)	Lbuf2	190pH
Controlling parameters		
First buffer bias current	Ibuf1	5mA
Second buffer bias current	Ibuf2	10mA

#### 4.1.4 Simulation results

Transient simulations of the circuit are used to estimate the QVCO output amplitude. As shown in Figure 4.2, an approximate value of 0.22V-peak is achieved at the QVCO output. This is 50mV-peak lower than the value achieved before (Figure 3.18), because different circuit loading the buffer was used. The buffer load affects the QVCO output through feedback via gate-drain parasitic capacitance of the buffer transistor ( $C_{gd,buf}$ ). The oscillation frequency is expected to change as well. As shown in Figure 4.3, output tuning range of 56-64GHz is achieved. This is 800MHz lower than the simulated 56.8-64.8GHz in Figure 3.18, but still within the required 8GHz range. Note that the spectral width of the QVCO output at higher frequency indicates phase noise degradation, which is expected from the previous QVCO simulations (see Figure 3.19). With a QVCO single-ended output of 200mV, voltages at the divider and mixer inputs are shown in Figure 4.4 with different  $L_{buf1}$  values. A 0.473V-peak (0.946V-pp) signal is achieved at the divider input. This is close to the rail-to-rail input swing required for the maximum locking range of the divider (Figure 3.32). At the mixer input, however, a value of 330mV-peak is achieved. With an increased load resistance ( $R_L=2k\Omega$  instead of  $1.5k\Omega$ ), a conversion gain of 26dB is still achievable. The whole front-end consumes 26.6mW from the QVCO, 13.3mW from the divider chain, 21.8mW from the LNA and mixer combination, 2x5mW from the first buffer and 2x10mW from the second buffer. This gives a total of 91.7mW for the front-end circuit.

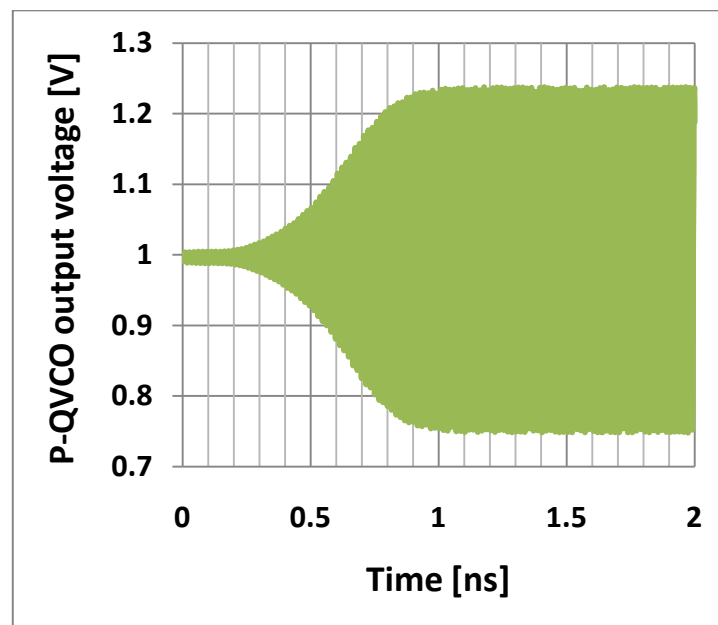


Figure 4.2: P-QVCO transient output voltage in the complete top-level system.

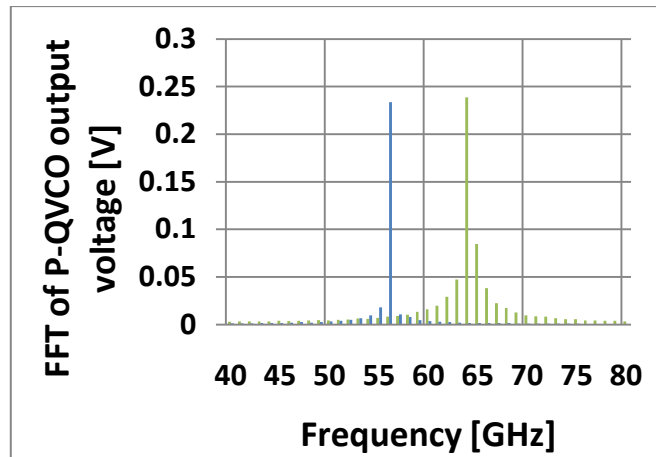


Figure 4.3: FFT of the P-QVCO output at max. and min. tuning ranges.

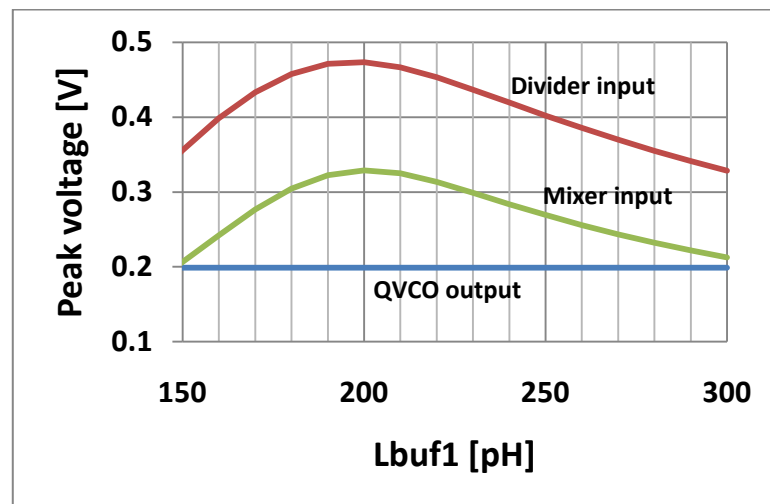


Figure 4.4: Voltage levels at the mixer and divider inputs vs. Lbuf1 value.

## 4.2 QVCO and divider sub-system

Due to time limitations, the whole front-end top-level is not laid-out. So, a QVCO, LO buffer, first stage divider and an output buffer are to be considered for layout. The top-level schematic of this sub-system and its simulation results are going to be presented in this section.

### 4.2.1 Circuit schematic

The top-level schematic of the sub-system is shown in Figure 4.5. Compared to Figure 3.12, one buffer output drives the 60GHz divide-by-2 stage.

## 4.2.2 Design choices

As shown previously in Figure 3.18, rail-to-rail output voltage swing was not achieved when the LO buffer is loaded with two divider injecting transistors, each with 20um gate width. As explained in section 2.3.1, using two injecting transistors can increase the injecting transistor output conductance with the drawback of larger input device. Thus, a single injecting transistor is implemented (with a width of 24um), which provides a smaller load for the LO buffer. As will be shown in the simulation results (Figure 4.8), this causes a reduced locking range compared to Figure 3.32, but can still be matched to the QVCO output tuning range (with a divider input voltage swing of 0.4V). Using two buffers to drive the divider is recommended for future work.

As explained in section 3.3.3.10, a choice can be made between the transformer-coupled and the inductively-tuned buffer configurations depending on the buffer load resistance. Both configurations were simulated with the single injecting transistor divider. The buffer output voltage swing was higher in the case of inductively-tuned buffer. This is because the resistive contribution of the 24um wide divider input to the buffer output resistance is higher than that of the transformer (see equations 2.11 and 2.142.16).

Neutralization capacitors ( $C_c$ ) are used in the LO buffer to provide more stability [61]. They cancel the effect of the feedback parasitic capacitance ( $C_{gd,buf}$ ) and help increase the oscillator output amplitude. The neutralization capacitors are implemented as MOS transistors with the gate and source connected together. This adds a gate-source and bulk capacitances to the gate-drain capacitance required for neutralization. Hence, the neutralization capacitors can be designed smaller than the buffer transistor to account for these additional parasitic capacitances. The phase noise improvement due to the neutralization capacitors will be shown in section 4.2.4.3.2.

The output buffer is a source follower with its source connected to the output pads through 50 $\Omega$  transmission lines. The source-follower is biased with an external current source ( $I_{sf}$ ).  $L_{tee}$  is an external inductor that is used to increase the current source output impedance and  $C_{tee}$  is an external decoupling capacitor. Together with the source follower size,  $I_{sf}$  adjusts the transistor output impedance to 50 $\Omega$ .

**Figure 4.5: QVCO and divider sub-system circuit schematic.**

### 4.2.3 Design values

Design values of the P-QVCO are the same as those listed in Table 3.2. Design values of the LO buffer, divider and output buffer are listed in Table 4.2. The transistor finger width of all the following transistors is 1 $\mu$ m. M defines the number of fingers and L is the channel length.

**Table 4.2: Design values of the sub-system blocks (without the QVCO).**

<b>Transistor sizes</b>		
<b>Parameter</b>		<b>Value</b>
LO buffer transistor (Mbuf)	M	14
	L	80nm
Neutralization transistor (Mn)	M	12
	L	80nm
LO buffer current mirror (Mcm,buf)	M	208
	L	300nm
Divider transistor (Mdiv60)	M	26
	L	80nm
Injecting transistor (Minj60)	M	24
	L	80nm
Divider current mirror (Mcm,div60)	M	96
	L	160nm
Output buffer transistor (Msf)	M	16
	L	80nm
<b>Passive elements' values</b>		
LO buffer inductor (without Cc)	Lbuf	300pH
LO buffer inductor (with Cc)	Lbuf	160pH
Divider inductor	Ldiv60	300pH
<b>Controlling parameters</b>		
LO buffer bias current	Ibuf	10mA
Divider bias current	Idiv60	1mA
Output buffer bias current	Isf	5mA

### 4.2.4 Simulation results

The simulation results of each circuit block will be presented. Each block is loaded by the following stage during simulation.

#### 4.2.4.1 Source follower

The real part of the source follower output impedance ( $Z_{sf,out}$ ) is shown in Figure 4.6. Figure 4.6a shows the variation of  $\text{Re}(Z_{sf,out})$  with different values of the source-follower width ( $M_{sf}$ ) if  $L_{tee}$  is connected to ground. At  $M_{sf}=16$  and  $I_{sf}$  connected, output impedance of  $50\Omega$  can be achieved at  $4.5\text{mA}$  as shown in Figure 4.6b. Lower current can be achieved at larger  $M_{sf}$  (e.g.,  $1.3\text{mA}$  at  $M_{sf}$  of  $30\mu\text{m}$ ), but this will load the divider and degrade the locking range. The small-signal gain of the source-follower at a bias current of  $4.5\text{mA}$  is shown versus frequency in Figure 4.7a. A value of  $0.41x$  is achieved for the buffer gain at  $30\text{GHz}$ . The large-signal gain versus the input amplitude is shown in Figure 4.7b. A value of around  $0\text{dBm}$  ( $\sim 0.32\text{V}$ ) is expected from the divider output. The large signal gain at this value is still above  $0.4x$ .

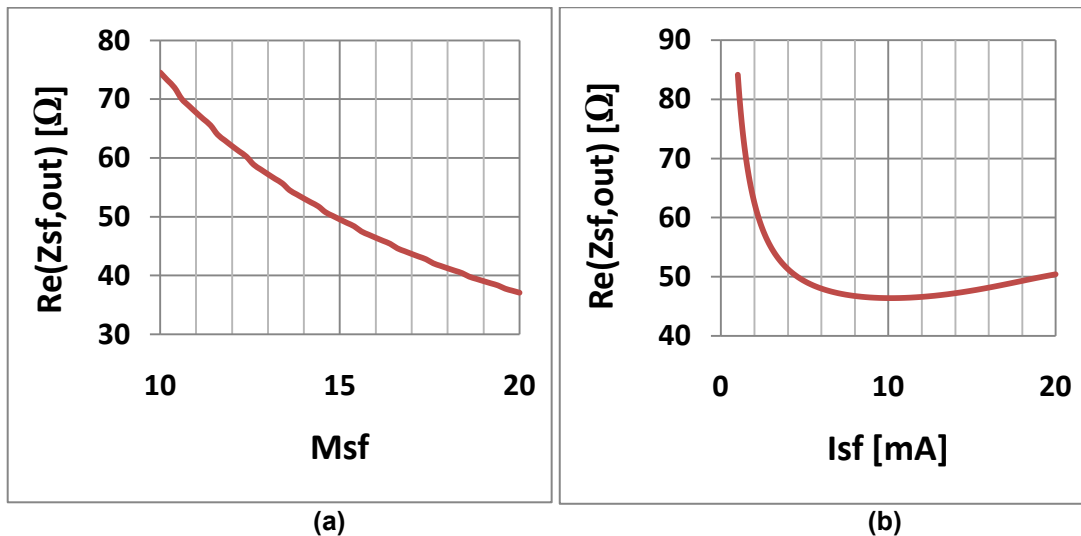


Figure 4.6: Real part of the source follower output impedance (a) without current source, and (b) with current source at  $M_{sf}=16$ .

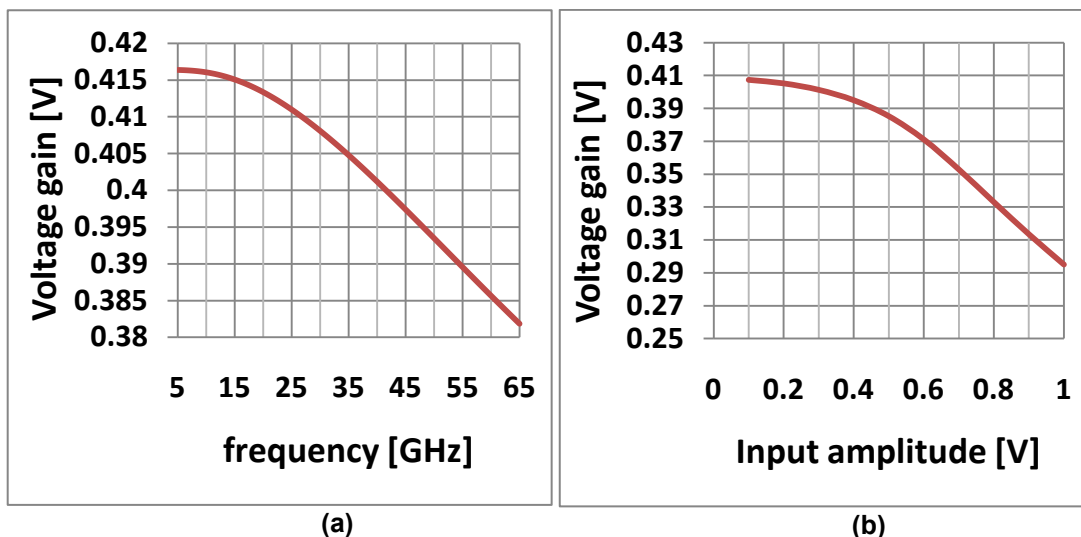


Figure 4.7: (a) Small- and (b) large-signal voltage gain of the source follower.

#### 4.2.4.2 Divider

The input sensitivity curve of the 60GHz divider and the divider output power versus input frequency is shown in Figure 4.8 and Figure 4.9, respectively. At 2dBm ( $\sim 0.4V$ -peak) input, 10GHz locking range is predicted from simulations at the schematic level. The inductor used is an ideal one with estimated quality factor of 15. The inductor is implemented with the following parameter values:  $N=2$ ,  $W=3\mu m$ ,  $S=2\mu m$  and  $OD=55\mu m$ .

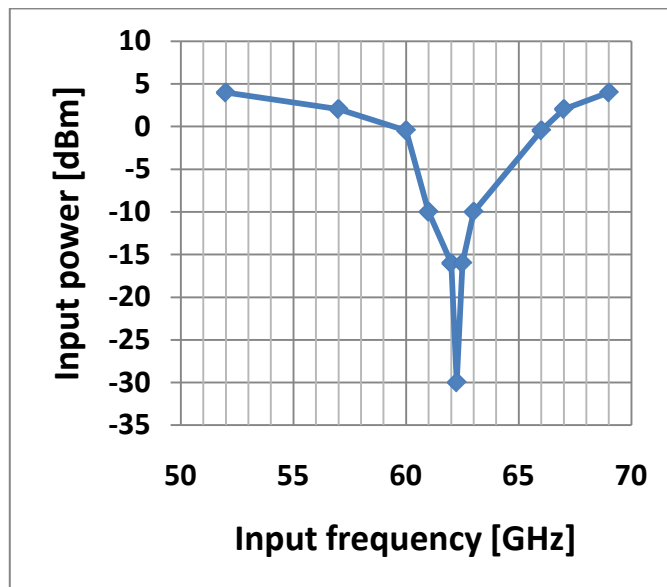


Figure 4.8: Input sensitivity curve of the sub-system divider.

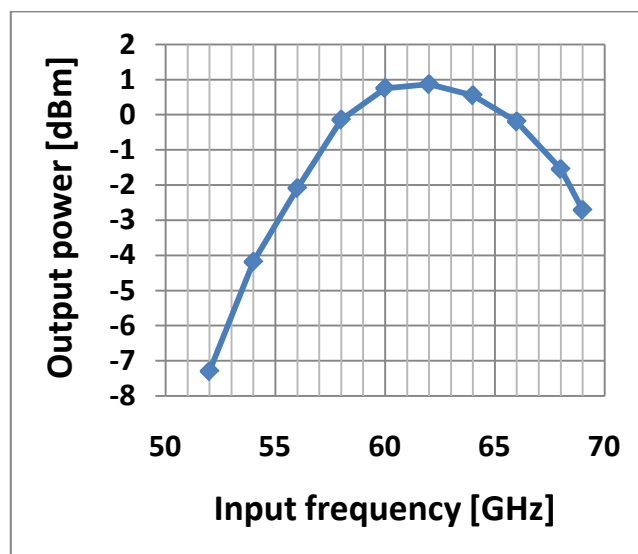


Figure 4.9: Output power of the sub-system divider.

### 4.2.4.3 QVCO and LO buffer

The output voltage levels and phase noise results are going to be shown across the tuning range in the following sub-sections. The results of the circuit with and without the neutralization capacitors are presented.

#### 4.2.4.3.1 Without neutralization capacitors

The performance of the sub-system without adding neutralization capacitors is shown in Figure 4.10. The divider input (Bbuf as indicated in Figure 4.5) can reach about 0.4V-peak, and the tuning range is 8.4GHz. The phase noise is increased at higher frequencies of the tuning range. This is noticed before in section 3.3.5.2. Neutralization capacitors are going to be used in the following sub-section to cancel the effect of  $C_{gd,buf}$ . This improves the oscillator output, and phase noise accordingly (Equation 2.9).

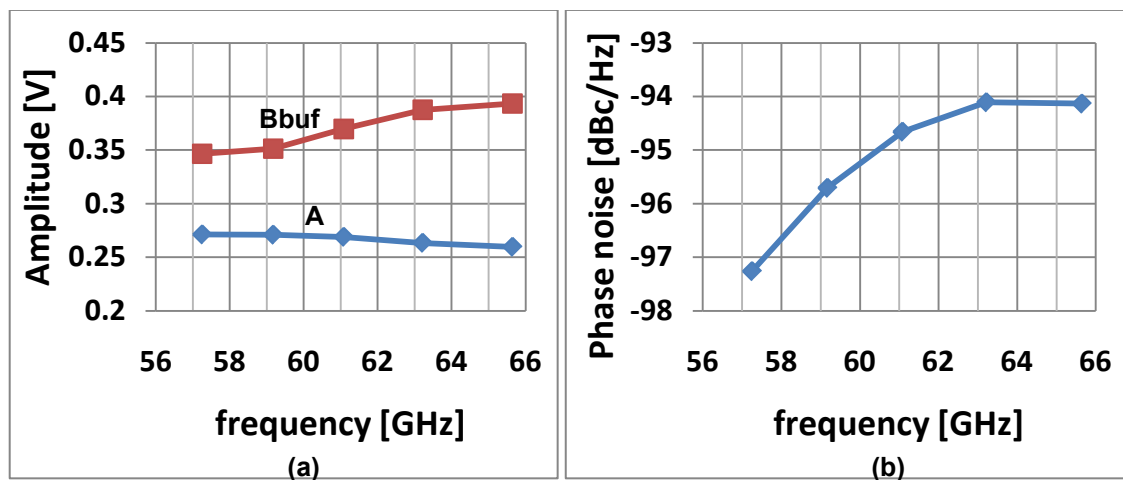


Figure 4.10: (a) Amplitudes and (b) phase noise of the sub-system QVCO and LO buffer vs. tuning range without neutralization capacitors.

#### 4.2.4.3.2 With neutralization capacitors

Figure 4.11 shows the performance of the QVCO and LO buffer after using the neutralization capacitors. The phase noise shows a noticeable improvement due to the increased oscillator amplitude (A). A maximum of -97.4dBc/Hz is predicted from simulation at maximum operating frequency. All parameters are the same as the case without  $C_c$  except for the buffer inductor, which is 160pH instead of the 300pH. This is due to the additional capacitance seen at the buffer output node. The gain is also reduced, and a maximum of 0.25V-peak is simulated at the divider input (Bbuf). The

circuit consumes a total of 55mW. The output voltage can be increased by increasing the bias current. This causes more power to be consumed in the QVCO.

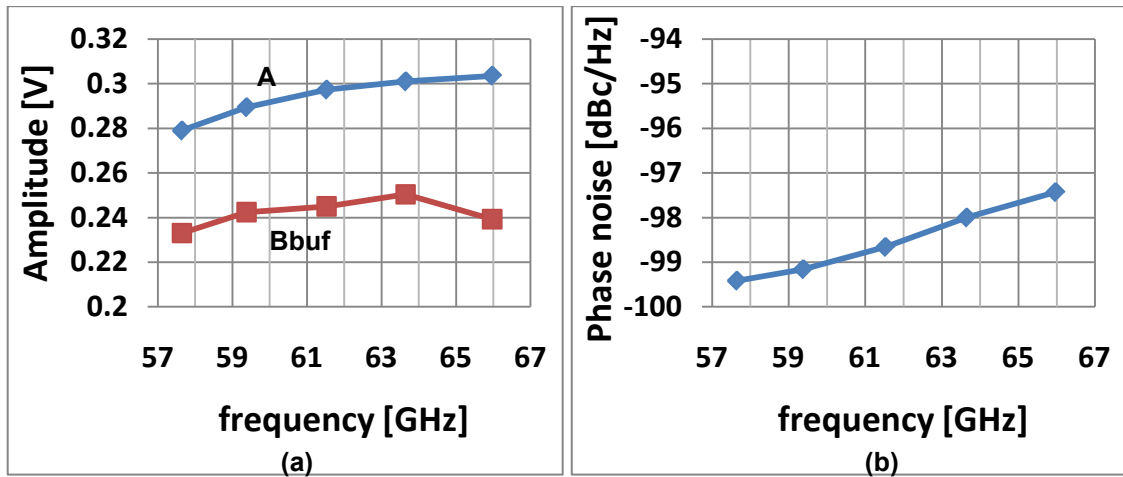


Figure 4.11: (a) Amplitudes and (b) phase noise of the sub-system QVCO and LO buffer vs. tuning range with neutralization capacitors.

The previous discussion shows a trade-off between output amplitude (or power consumption) and phase noise. The neutralization capacitors reduce total phase noise, but also the LO buffer gain. As the main target of the QVCO design is to achieve low phase noise, the circuit using neutralization capacitors is chosen to be laid-out and tested. This will be shown in the next chapter.

# Chapter 5

# Layout and Post-Layout Simulations

---

The sub-system in section 4.2 is laid-out and taped-out for testing. Due to time limitations, measurement results are not going to be part of this work. The post-layout simulation results are going to be provided.

## 5.1 Physical layout

The schematic used is shown in Figure 4.5. The circuit consists of a P-QVCO, LO buffer, a divide-by-two stage and output buffers. Current sources are provided externally. The top-level circuit layout with the pads connecting input-output signals (IO ring) is shown in Figure 5.1. The IO ring doesn't enclose the circuit core symmetrically due to the available chip area. The circuit core is only 0.33mmx0.2mm, and the chip with IO ring is 1.1mmx0.63mm. Unit elements (5umx5um) of technology metal stack are used to form a low-resistance ground plane. Ground cells are used in the chip to connect the external supply and ground pads to the internal nodes.

Figure 5.2 is a zoom-in to the circuit core. The QVCO inductor ( $L_{vco}$ ) parameters are mentioned in section 3.3.3.3. An inductance value of 39.6pH and a quality factor of 14.2 are predicted using this inductor. The LO buffer and divider inductors ( $L_{buf}$  and  $L_{div60}$ ) parameters are listed in Table 5.1. The interconnect lines to the active elements are taken into account.

Figure 5.3 shows the QVCO layout without the ground cells. The buffer transistor ( $M_{buf}$ ) is placed close to the QVCO output. The QVCO layout, without the current mirror transistors and biasing resistors ( $R_d$ ), is symmetrical around its center.

Table 5.1: Inductor parameters for the LO buffer and divider in the test chip.

Parameter	N	W	S	OD	L	Q	fo
Lbuf	2	2um	2um	35um	240pH	10	60GHz
Ldiv60	2	3um	2um	48um	247pH	14.9	30GHz

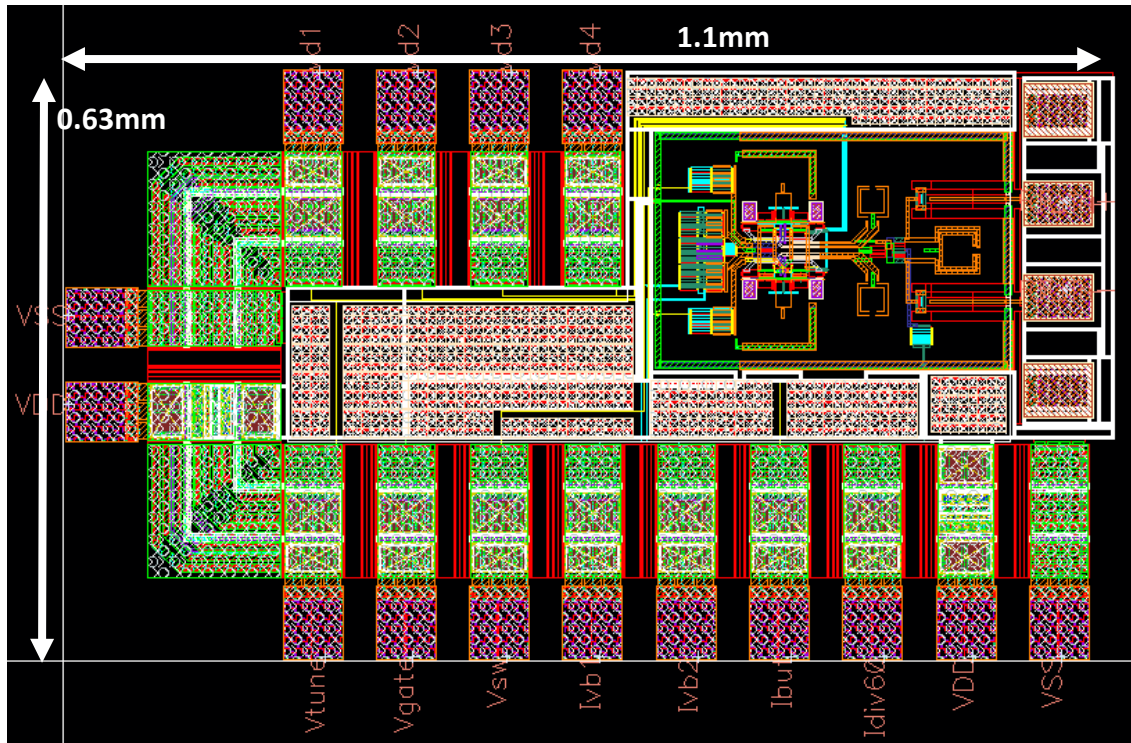


Figure 5.1: Top-level circuit layout with IO rings.

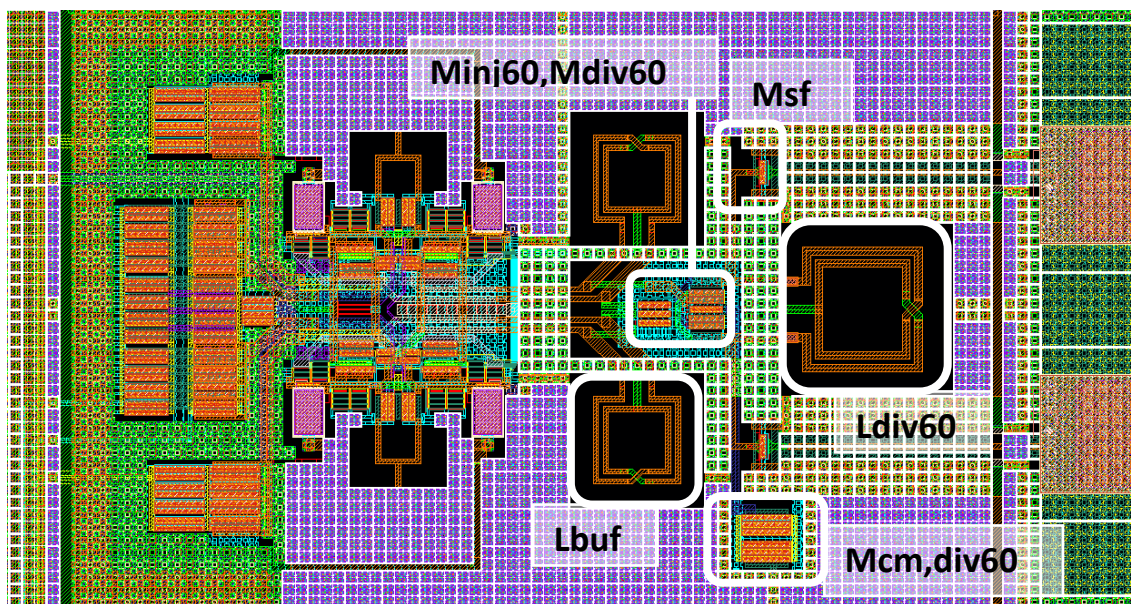


Figure 5.2: The circuit core including the QVCO, LO buffer, divider and output buffer.

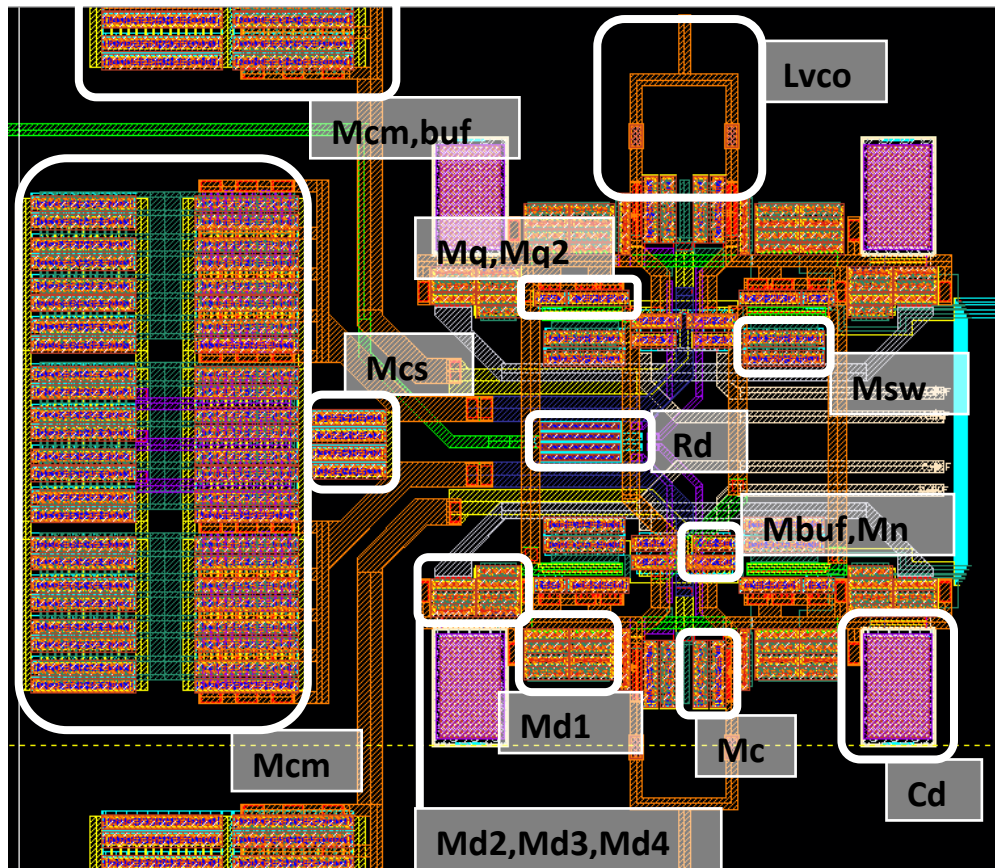


Figure 5.3: The P-QVCO, and LO buffer active elements with the ground cells omitted.

## 5.2 Nominal simulation results

The following simulations are performed with typical process parameters, a supply voltage of 1V and at a temperature of 27°C.

### 5.2.1 Divider

The aim of the divider stage is to translate the output signal from 60GHz to 30GHz. Thus, the free-running frequency should be around 30GHz. As shown in Table 4.2, a value of 300pH was selected for the divider inductor ( $L_{div60}$ ). This can be implemented with an inductor of OD of 55 $\mu$ m. An inductor with OD of 48 $\mu$ m is, mistakenly, chosen instead. This inductor has 300pH at 60GHz, but it only has 247pH at 30GHz. As shown in Figure 5.4 and Figure 5.5, a shift of 8GHz is caused in the input locking range (at minimum input amplitude) when the OD=48 $\mu$ m inductor is used. This can cause a mismatch between the QVCO output frequency range and the divider input locking range, and the divider output will not track the input frequency anymore.

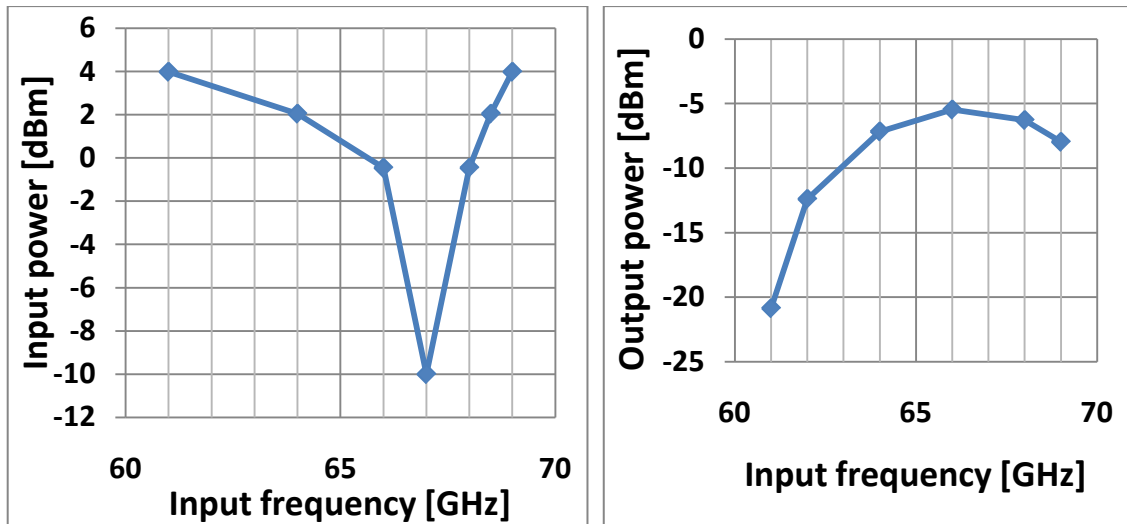


Figure 5.4: Divider input sensitivity curve and output power for a 48um OD inductor.

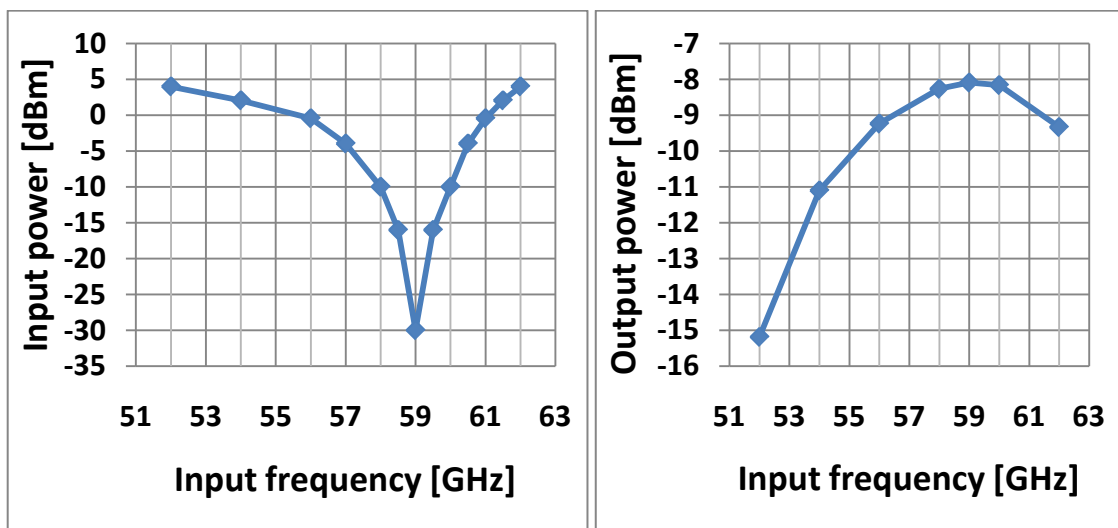


Figure 5.5: Divider input sensitivity curve and output power for a 55um OD inductor.

### 5.2.2 QVCO and LO buffer

The post-layout simulation results after the P-QVCO and LO buffer are shown in this section. The divider inductor used in these simulations is the one with OD of 55um. Figure 5.6 shows the output amplitudes and phase noise versus the QVCO bias current source ( $I_{vco}$ ) at the middle of the tuning range and a gate voltage of 1V. More current is required to start the oscillation as compared to the schematic because of the parasitic resistance. Also the inductor value is around 40pH, which is lower than the one used in the schematic. This is to overcome the additional layout parasitic capacitance. The reduced QVCO inductor leads to lower amplitude, and thus more current is required for

the start-up. With a QVCO bias current of 30mA, the gate voltage ( $V_{gate}$ ) is varied in Figure 5.7, and phase noise reaches a minimum value at  $V_{gate}$  of 1V. Figure 5.8 shows the QVCO and LO buffer amplitudes and phase noise at 30mA bias current and 1V gate voltage. The simulated LO buffer output is around 0.25V and the tuning range is 6.3GHz centered at 58.5GHz. A maximum phase noise value of -97.4dBc/Hz is predicted from simulation, which is the main target specification. The LO buffer output amplitude can be increased either by removing the neutralization capacitors and increasing the buffer transistor ( $M_{buf}$ ) gate-width or using a two-stage buffer to boost the voltage swing. The first solution increases the phase noise and the second solution costs more supply current and chip area.

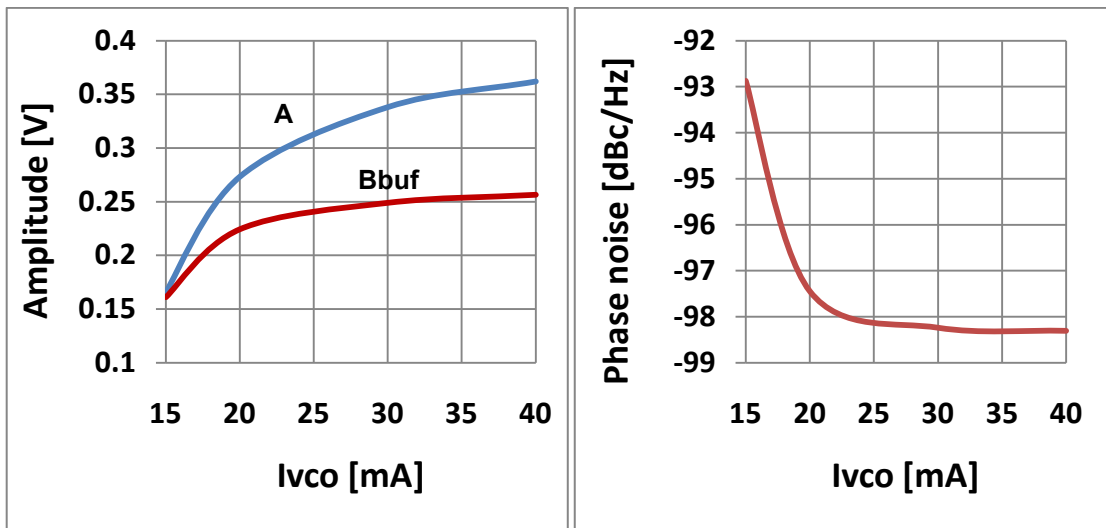


Figure 5.6: Variation with QVCO bias current at  $V_{gate}$  of 1V.

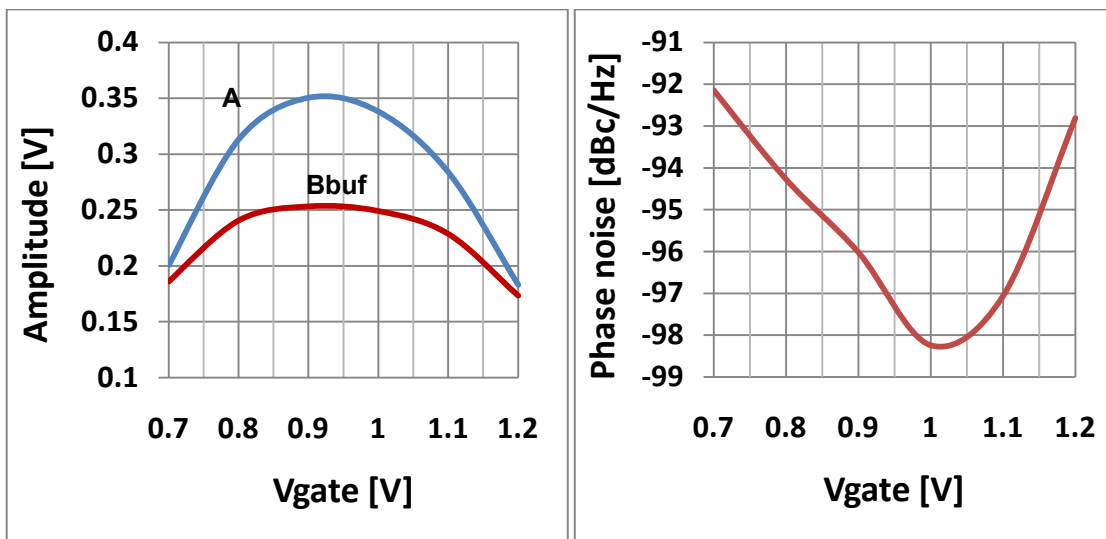


Figure 5.7: Variations with gate voltage at  $I_{vco}$  of 30mA.

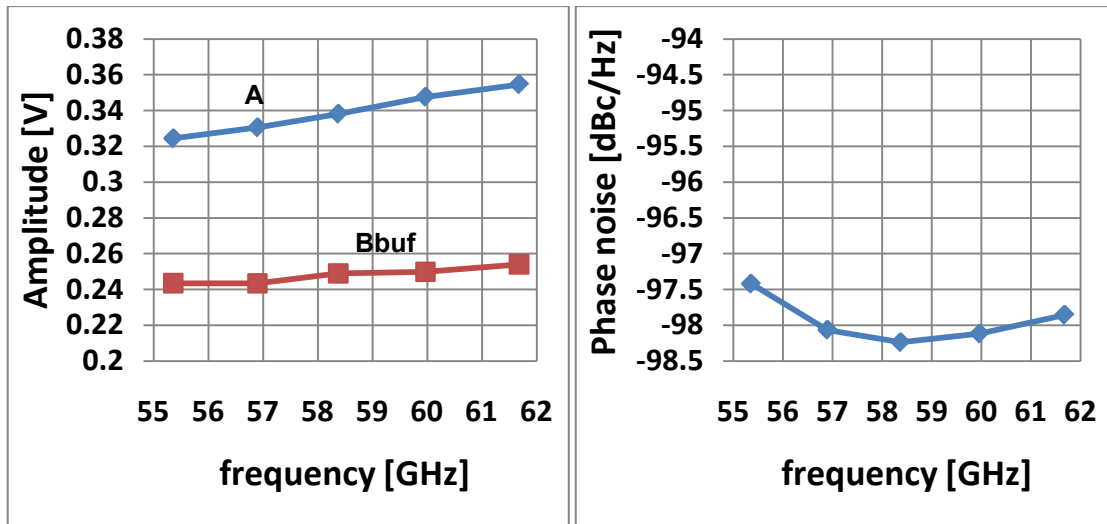


Figure 5.8: Performance at Vgate of 1V and Ivco of 30mA over the tuning range.

### 5.3 PVT simulations

The aim of this section is to provide simulation results at different process corners, supply voltages and operating temperatures (PV and T). As shown in Figure 5.9, the power supply is swept from 0.9V to 1.1V ( $\pm 10\%$  with a nominal value of 1V) using a typical process with a temperature of 27°C (room temperature). Simulations with different process corners are performed first on the schematic level. MOS process corners are: typical (TT), slow-NMOS-slow-PMOS (SS), slow-NMOS-fast-PMOS (SF), fast-NMOS-slow-PMOS (FS) and fast-NMOS-fast-PMOS (FF). Figure 5.10 shows the output amplitudes, phase noise and oscillation frequency versus process corners at nominal supply voltage (1V) and room temperature (27°C). The QVCO output amplitude at the slow process (SS) is the smallest. Higher temperature leads to lower carrier mobility and slower operation. Thus, the worst case is to simulate a slow process with high temperature (e.g., 100°C) and low supply voltage (0.9V), and a fast process with low temperature (e.g., 0°C) and high supply voltage (1.1V). Worst case results are summarized in Table 5.2 for pre- and post-layout simulations. The slow combination needs more current for start-up. The listed schematic simulation results for PVT of SS, 0.9V and 100°C use a gate voltage of 0.7V and a QVCO bias current of 25mA (the default values are a gate voltage of 0.6V and bias current of 10mA). The post-layout worst case slow simulation did not start up.

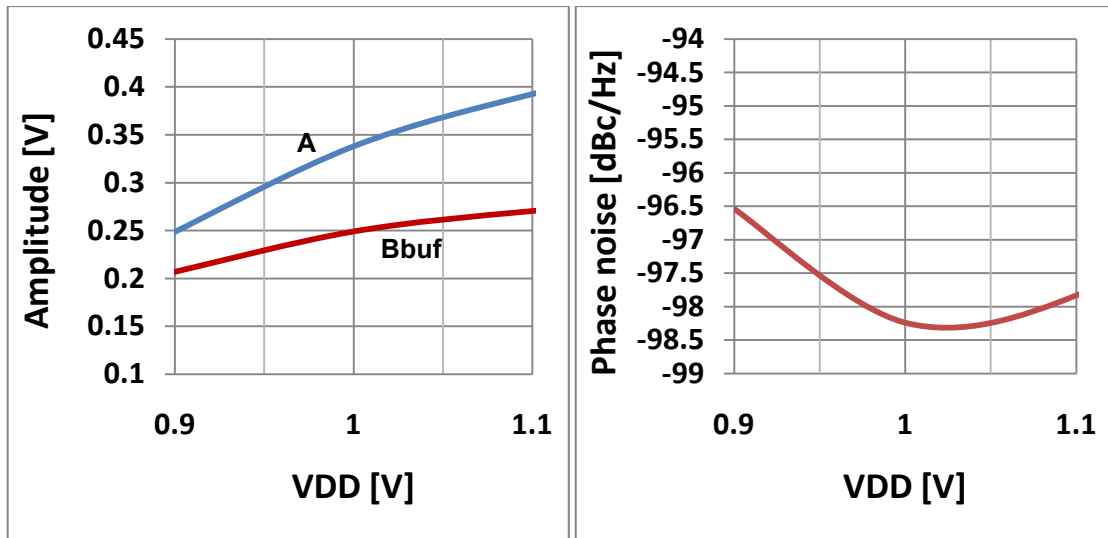


Figure 5.9: Amplitude and phase noise variations of the QVCO and LO buffer with supply voltage at  $V_{gate}$  of 1V and  $I_{vco}$  of 30mA.

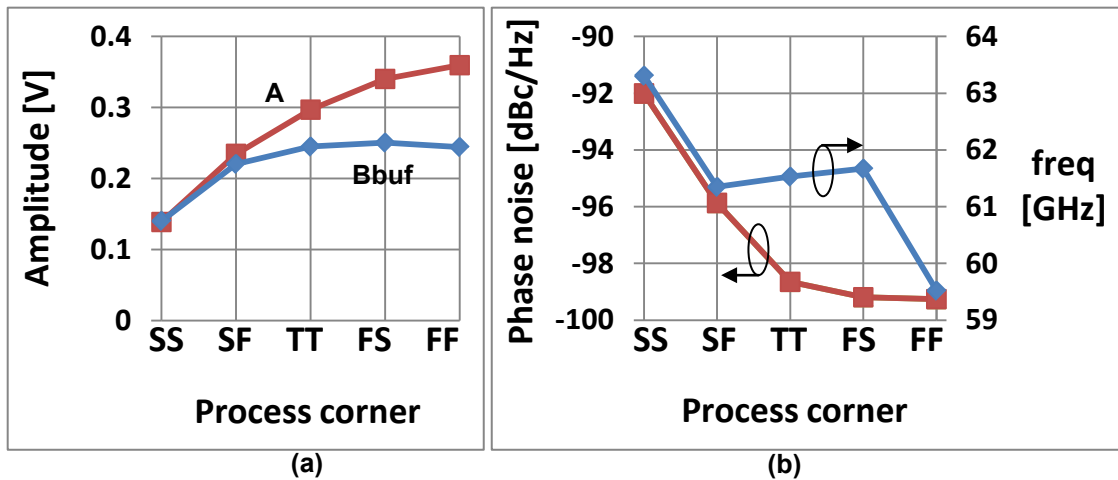


Figure 5.10: (a) Amplitudes, (b) phase noise and oscillation frequency schematic simulations vs. process corners at 27°C.

Table 5.2: Worst case PVT simulation results.

	Process corner	$V_{DD}$ [V]	Temp. [°C]	Phase noise	QVCO output (A)	Divider input (Bbuf)	Oscillation frequency
Schematic	FF	1.1	0	-99.93dBc/Hz	382.4mV	257.1mV	59.46GHz
	SS	0.9	100	-87.67dBc/Hz	212.3mV	186.9mV	62.7GHz
Layout	FF	1.1	0	-98.13dBc/Hz	460mV	261.2mV	56.32GHz
	SS	0.9	100	×	×	×	×

# Chapter 6

## Conclusions

---

In this work, a receiver front-end at 60GHz is explored. The circuit includes a QVCO, divider chain, LNA, mixer and LO buffers. A test-chip including the QVCO, LO buffer and the first stage divider is designed to verify the key components of the receiver design. The thesis summary and recommendations for future work are discussed in this chapter.

### 6.1 Summary

Chapter 1 is an introduction, including the 60GHz band standards and system architecture. The unlicensed frequency band between 57GHz and 66GHz is assigned for 60GHz operation in different countries. This can be used in applications that need data rates up to tens of gigabits per second according to the IEEE 802.15.3c and ECMA-387 standards, such as short range cable replacement with very high speed wireless links.

In chapter 2, a theoretical background on the blocks used in the circuit is provided. The cross-coupled LC VCO theory is elaborated with more details on phase noise. The parallel, series and gate-modulated QVCO topologies are presented. For the LO buffer, the inductively-tuned and transformer-coupled common-source configurations were analyzed. The ILFD theory for use in the first and second divider blocks is presented. The other two divider blocks use static high frequency CML divide-by-two circuits. The chapter ends with noise figure and linearity background with the used inductively-degenerated cascode LNA and active mixer.

The schematics, design steps and simulation results of the circuit blocks are included in chapter 3. The parallel QVCO is gate-decoupled and biased externally to achieve a better phase noise performance. Variable coupling was also implemented to ensure oscillator start-up. The P-QVCO achieved phase noise values of -98.9dBc/Hz to -94.8dBc/Hz over the 8GHz tuning range. Voltage levels of up to 0.52V-peak were achieved at the LO buffer output. The bottom-series QVCO achieved approximately the

same performance, but with 10mW power consumption compared to the 26.6mW consumed by the P-QVCO. Two ILFD circuits were designed at 60GHz and 30GHz. More insight into the effect of the inductor quality factor of the locking range was introduced. Two regions of operation were defined according to the value of the quality factor: the Q-limited and  $g_{q,max}$ -limited regimes. In the  $g_{q,max}$ -limited region, the locking range doesn't depend on the inductor quality factor as long as the injecting transistor output conductance and total capacitance are fixed. Locking ranges up to 15GHz are achieved at 60GHz using the dual-mixing ILFD. A maximum operating frequency of 25GHz is achieved using the static CML divider. The whole divider chain consumes 9mW without the output buffers. The LNA and mixer combination achieves a maximum conversion gain of 26.77dB and a noise figure of 5.88dB. The output -1dB compression point is +6.3dBm, IIP3 is -8.6dBm and it consumes 21.8mW including all biasing circuitry.

In chapter 4, the top-level design of the receiver front-end is presented. Two LO buffers were used to drive the mixer and divider chain. The P-QVCO, LO buffer and the first stage of the divider chain are connected in a separate sub-system to be simulated for tape-out. With the use of neutralization capacitors in the LO buffer, maximum phase noise of -97.4dBc/Hz is predicted from simulations.

The layout of the test-chip is shown in chapter 5. The post layout simulations show a maximum of -97.4dBc/Hz of phase noise and a 55.4–61.7GHz tuning range. The LO buffer output voltage is around 0.25V-peak. This can be improved by post-layout optimization of circuit parameters or different circuit topologies as will be discussed in the future work.

## 6.2 Future work

The gate-decoupled P-QVCO is used in the test circuit. However, as shown in section 3.3.6, the BS-QVCO consumes less power and gives approximately the same phase noise performance. Thus, a layout for the BS-QVCO should be made for lower power consumption in the QVCO. Due to time limitations, no extensive trials were performed on the GM-QVCO. The GM-QVCO is expected to provide better phase noise [37]. The QVCO inductor can, thus, be increased allowing for better modeling and lower power consumption.

The main problem in the test circuit is the low voltage levels at the divider input. The divider locking range depends on the input amplitude. Two buffer stages can be used to provide amplitudes high enough for large divider locking range. This is used in the front-end top level but not implemented in the test chip due to time limitations.

Traditional inductively-degenerated cascode LNA and active mixer are used in the design. Passive mixers could be investigated for better linearity, with the challenge of switching speed and Op-Amp bandwidth. Innovative topologies for wideband LNA should also be investigated in the future. The current LNA can handle an input bandwidth of around 2GHz that accounts for a single channel. If channel bonding is used, more bandwidth (up to 9GHz for 4 channels) will be required. Thus, more effort should be spent on designing a wideband LNA at 60GHz.

# Appendix A

## Transformer-Coupled Buffer

---

The current-output transformer-coupled common-source differential amplifier (Figure 2.20b) will be analyzed in this appendix. The buffer output impedance due to the transformer load (Equation 2.15) is derived. For simplicity, the load is assumed to be only capacitive ( $C_{load}=C$ ). We'll assume that the buffer side of the transformer is the primary side (with "p" subscript) and the load represents the secondary side (with "s" subscript). The transformer primary and secondary voltages can be written as following:

$$v_p = j\omega L i_p + j\omega M i_s \quad \text{A.1}$$

$$v_s = j\omega L i_s + j\omega M i_p \quad \text{A.2}$$

The load is only capacitive. So,

$$Z_s = \frac{v_s}{i_s} = -\frac{1}{j\omega C}$$

By substituting into A.2:

$$-\frac{i_s}{j\omega C} = j\omega L i_s + j\omega M i_p$$

$$-i_s \left( j\omega L + \frac{1}{j\omega C} \right) = j\omega M i_p$$

$$\frac{i_s}{i_p} = \frac{-j\omega M}{j\omega L + \frac{1}{j\omega C}} = \frac{-j\omega kL \times j\omega C}{-\omega^2 LC + 1} = \frac{\omega^2 LCk}{1 - \omega^2 LC} \quad \text{A.3}$$

The primary impedance from A.1 is:

$$Z_p = \frac{v_p}{i_p} = j\omega L + j\omega M \frac{i_s}{i_p}$$

Using A.3, the buffer output impedance can be derived.

$$Z_{\text{out}} = Z_p = j\omega L + j\omega k L \frac{\omega^2 L C k}{1 - \omega^2 L C}$$

$$Z_{\text{out}} = j\omega \left( L + \frac{\omega^2 L^2 C_{\text{load}} k^2}{1 - \omega^2 L C} \right)$$

# Bibliography

---

- [1] International Telecommunication Union. [Online]. <http://www.itu.int/>
- [2] IEEE Std 521-2002, IEEE Standard Letter Designations for Radar-Frequency Bands, 2003.
- [3] FCC, Operation within the band 57-64 GHz, Code of Federal Regulations, title 47, vol. 1, part 15.255c, Oct 1, 2001. [Online].  
<http://frwebgate.access.gpo.gov/cgi-bin/get-cfr.cgi?TITLE=47&PART=15&SECTION=255&YEAR=2001&TYPE=TEXT>
- [4] Nan Guo, Robert C. Qiu, Shaomin S. Mo and Kazuaki Takahashi, "60-GHz Millimeter-Wave Radio: Principle, Technology, and New Results," EURASIP Journal on Wireless Communications and Networking, ID 68253, 2007.
- [5] Eino Kivisaari, 60 GHz MMW Applications, Helsinki University of Technology, Telecommunications and Multimedia Laboratory, Apr. 9, 2003. [Online].  
<http://www.tml.tkk.fi/Opinnot/T-109.551/2003/kalvot/60GHz.ppt>
- [6] IEEE Std 802.15.3c-2009, Wireless MAC and PHY Specifications for High Rate WPANs, Oct. 2009.
- [7] "Standard ECMA-387 – High Rate 60GHz PHY, MAC and HDMI PAL," ECMA International, Dec. 2008.
- [8] Ali M. Niknejad and Hossein Hashemi, mm-Wave Silicon Technology: 60 GHz and Beyond, Springer, 2008.
- [9] Wikipedia, Beamforming. [Online]. <http://en.wikipedia.org/wiki/Beamforming>
- [10] B.D. Van Veen and K.M. Buckley, "Beamforming: A Versatile Approach to Spatial Filtering," IEEE ASSP Magazine, vol.5, no.2, pp.4-24, Apr. 1988.

- [11] Dixian Zhao, 60 GHz Beamforming Transmitter Design for Pulse Doppler Radar, M.Sc. thesis, Delft University of Technology, Feb. 2009.
- [12] J. Bass, E. Rodriguez, J. Finnigan, C. McPheeters, Beamforming Basics, Connexions Web site, Jul. 27, 2005. [Online].  
<http://cnx.org/content/m12563/latest/>
- [13] Karen Scheir, CMOS Building Blocks for 60 GHz Phased-Array Receivers, Ph.D. thesis, Vrije Universiteit Brussel, Dec. 2009.
- [14] A. Natarajan, B. Floyd, and A. Hajimiri, "A Bidirectional RF-Combining 60 GHz Phased-Array Front-End," IEEE ISSCC Dig. Tech. Papers, pp.202–597, Feb. 2007.
- [15] J. Roderick, H. Krishnaswamy, K. Newton and H. Hashemi, "Silicon-Based Ultra-Wideband Beam-Forming," IEEE J. Solid-State Circuits, vol.41, no.8, pp.1726-1739, Aug. 2006.
- [16] John R. Long, RF Integrated Circuit Design, TU-Delft MSc. course lecture notes, 2009.
- [17] M.J.M. Pelgrom, A.C.J. Duinmaijer and A.P.G. Welbers, "Matching Properties of MOS Transistors," IEEE J. Solid-State Circuits, vol.24, no.5, pp.1433-1440, Oct. 1989.
- [18] Advanced Design System (ADS), Agilent Technologies. [Online].  
<http://www.agilent.com/find/eesof-ads>
- [19] HFSS, Ansoft. [Online]. <http://www.ansoft.com/products/hf/hfss/>
- [20] Software for IC Design and Circuit Design Verification, Mentor Graphics. [Online]. [http://www.mentor.com/products/ic\\_nanometer\\_design/](http://www.mentor.com/products/ic_nanometer_design/)
- [21] Assura Physical Verification. [Online].  
<http://www.cadence.com/products/mfg/apv/>
- [22] 60-GHz Applications, IBM Research. [Online].

[http://domino.watson.ibm.com/comm/research\\_projects.nsf/pages/mmwave.apps.html](http://domino.watson.ibm.com/comm/research_projects.nsf/pages/mmwave.apps.html)

- [23] A. Hajimiri and T.H. Lee, "Design issues in CMOS differential LC oscillators," IEEE J. Solid-State Circuits, vol.34, pp.717-724, May 1999.
- [24] Emad Hegazi, Jacob Rael and Asad Abidi, The Designer's Guide to High-Purity Oscillators, Springer, 2005.
- [25] D.B. Leeson, "A simple model of feedback oscillator noise spectrum," Proceedings of the IEEE, vol.54, pp.329-330, Feb. 1966.
- [26] J. Craninckx and M. Steyaert, "Low-noise voltage-controlled oscillators using enhanced LC-tanks," IEEE Trans. on Circuits and Systems II: Analog and Digital Signal Processing, vol.42, pp.794-804, Dec. 1995.
- [27] A. Hajimiri and T.H. Lee, "A general theory of phase noise in electrical oscillators," IEEE J. Solid-State Circuits, vol.33, pp.179-94, Feb. 1998.
- [28] Q. Huang, "On the exact design of RF oscillators," Proceedings of the IEEE. 1998 Custom Integrated Circuits Conference, May. 1998.
- [29] A. Demir, A. Mehrorta, and J. Roychowdhury, "Phase noise in oscillators: a unifying theory and numerical methods for characterization," IEEE Trans. on Circuits and Systems-I: Fundamental Theory and Applications, vol.47, no.5, pp.655-674, May 2000.
- [30] J.J. Rael and A.A. Abidi, "Physical processes of phase noise in differential LC oscillators," Proc. of IEEE Custom Integrated Circuits Conference (CICC), pp.569-572, 2000.
- [31] D. Ham and A. Hajimiri, "Concepts and methods in optimization of integrated LC VCOs," IEEE J. Solid-State Circuits, vol.36, pp.896-909, Jun. 2001.
- [32] P. Andreani and A. Fard, "More on the  $1/f^2$  phase noise performance of CMOS differential-pair LC-tank oscillators," IEEE J. Solid-State Circuits, vol.41, no.12,

pp.2703-2712, Dec. 2006.

- [33] H. Darabi, A.A. Abidi, "Noise in RF CMOS Mixers: A Simple Physical Model," IEEE J. Solid–States Circuits, vol.35, no.1, pp.15-25, Jan. 2000.
- [34] E. Hegazi, and A.A. Abidi, "Varactor Characteristics, Oscillator Tuning Curves, and AM–FM Conversion," IEEE J. Solid-State Circuits, vol.38, no.6, Jun. 2003.
- [35] S. Levantino, C. Samori, A. Zanchi and A.L. Lacaita, "AM-to-PM conversion in varactor-tuned oscillator" IEEE Trans. on Circuits and Systems-II, Analog and Digital Signal Processing, vol.49, no.7, pp.509-513, Jul. 2002.
- [36] B. Razavi, RF Microelectronics, Prentice Hall, 1998.
- [37] K.-W. Cheng, et al., "A gate-modulated CMOS LC quadrature VCO," IEEE Radio Frequency IC Symp., pp. 267-270, Jun. 2009.
- [38] A. Mazzanti and P. Andreani, "Class-C Harmonic CMOS VCOs, With a General Result on Phase Noise," IEEE J. Solid-State Circuits, vol.43, no.12, pp.2716-2729, Dec. 2008.
- [39] Vojkan Vidojkovic and Giovanni Mangraviti, Design of 60GHz CMOS receiver and power amplifier in 40 nm LP CMOS: LO buffer, Deliverable 60GHz-B2.2, IMEC SSET-WL, May. 2010.
- [40] M. Alioto and G. Palumbo, Model and Design of Bipolar and MOS Current-Mode Logic: CML, ECL and SCL Digital Circuit, Springer, 2005.
- [41] Almudena Suárez, Analysis and Design of Autonomous Microwave Circuits, Wiley-IEEE Press, 2009.
- [42] H.R. Rateg and T.H. Lee, "Superharmonic Injection-Locked Frequency Dividers," IEEE J. Solid-State Circuits, vol.34, no.6, pp.813-821, Jun. 1999.
- [43] H. Wu and A. Hajimiri, "A 19GHz, 0.5mW, 0.35um CMOS Frequency Divider with Shunt-Peaking Locking-Range Enhancement," IEEE ISSCC Dig. Tech. Papers, pp.412-413, Feb. 2001.

- [44] M. Tiebout, "A CMOS direct injection-locked oscillator topology as high-frequency low-power frequency divider," *IEEE J. Solid-State Circuits*, vol.39, no.7, pp.1170-1174, Jul. 2004.
- [45] K. Yamamoto and M. Fujishima, "55 GHz CMOS frequency divider with 3.2 GHz locking range," *Proc. ESSCIRC*, pp.135-138, Sep. 2004.
- [46] K. Yamamoto and M. Fujishima, "70GHz CMOS Harmonic Injection-Locked Divider," *IEEE ISSCC Dig. Tech. Papers*, pp.600–601, Jun. 2006.
- [47] C.-C. Chen, H.-W. Tsao and H. Wang, "Design and Analysis of CMOS Frequency Dividers With Wide Input Locking Ranges," *IEEE Trans. Microw. Theory Techn.*, vol.57, no.12, pp.3060-3069, Dec. 2009.
- [48] F. Ellinger et al., "30–40-GHz Drain-Pumped Passive-Mixer MMIC Fabricated on VLSI SOI CMOS Technology," *IEEE Trans. Microw. Theory Techn.*, vol.52, no.5, pp.1382–1391, May. 2004.
- [49] C.-Y. Wu and C.-Y. Yu, "Design and Analysis of a Millimeter-Wave Direct Injection-Locked Frequency Divider With Large Frequency Locking Range," *IEEE Trans. Microw. Theory Techn.*, vol.55, no.8, pp.1649-1658, Aug. 2007.
- [50] J.-C. Chien and L.-H. Lu, "40 GHz wide-locking-rangeregenerative frequency divider and low-phase-noise balancedVCO in 0.18  $\mu\text{m}$  CMOS," *IEEE ISSCC Dig. Tech. papers*, pp. 544–545, Feb. 2007.
- [51] M. Mizuno, et al., "A GHz MOS Adaptive Pipeline Technique Using MOS Current-Mode Logic," *IEEE J. Solid-State Circuits*, vol.31, no.6, pp.784-791, Jun.1996.
- [52] M. Usama and T.A. Kwasniewski, "New CML latch structure for high frequency Prescaler design," *Canadian Conference on Electrical and Computer Engineering 2004*, vol.4, pp.1915-1918, May 2004.
- [53] M. Usama and T.A. Kwasniewski, "A 40 GHz Frequency Divider in 90-nm CMOS Technology," *Proc. of International North East Workshop on Circuits and*

Systems (NEWCAS 2006), Jun. 2006.

- [54] Thomas H. Lee, *The Design of CMOS Radio-Frequency Integrated Circuits*, Cambridge University Press, Second Edition, 2004.
- [55] Leo de Vreede, *Microwave Circuit Design*, TU-Delft MSc. course lecture notes, 2009.
- [56] A. Rofougaran, et al., "A Single-Chip 900MHz Spread-Spectrum Wireless Transceiver in 1-mm CMOS - Part I: Architecture and Transmitter Design," *IEEE J. Solid-State Circuits*, vol.33, no.4, pp.515-534, Apr. 1998.
- [57] Pierre Wahl, *Exploring the Pathways of Faster Optical Telecommunication in 90nm CMOS: Design, analysis and Layout of a Quadrature Voltage-Controlled Oscillator*, M.Sc. thesis, Vrije Universiteit Brussel, Jun. 2009.
- [58] A. Kral, F. Behbahani, and A.A. Abidi, "RF-CMOS oscillators with switched tuning," in *Proc. IEEE Custom Integrated Circuits Conf.*, Santa Clara, CA, pp.555–558, May 1998.
- [59] A. D. Berny, A. M. Niknejad, and R. G. Meyer, "A 1.8-GHz LC VCO with 1.3-GHz tuning range and digital amplitude calibration," *IEEE J. Solid-State Circuits*, vol.40, no.4, pp.909-917, Apr. 2005.
- [60] S. Levantino, et al., "Frequency Dependence on Bias Current in 5-GHz CMOS VCOs: Impact on Tuning Range and Flicker Noise Upconversion," *IEEE J. Solid-State Circuits*, vol.37, no.8, pp.1003-1011, Aug. 2002.
- [61] W.L. Chan, J.R. Long, M. Spirito and J.J. Pekarik, "A 60GHz Band 1V 11.5dBm Power Amplifier with 11% PAE in 65nm CMOS," *IEEE ISSCC Dig. Tech. Papers*, pp.380-381a, Feb. 2009.
- [62] J. Borremans, K. Raczkowski and P. Wambacq, "A Digitally Controlled Compact 57-to-66GHz Front-End in 45nm Digital CMOS," *IEEE ISSCC Dig. Tech. papers*, pp.492-493a, Feb. 2009.

